

# Geologic Storage of CO<sub>2</sub>

## Investigators

Jerry Harris, Professor, Geophysics; Anthony Kovscek, Associate Professor, Franklin Orr, Jr., Professor, Energy Resources Engineering; Mark Zoback, Professor, Geophysics; Paul Hagin, Youli Quan, Research Associates, Geophysics; Tom Tang, Senior Research Associate, Energy Resources Engineering; Eduardo Santos, Postdoc, Geophysics; Adeyemi Arogunmati, Laura Chiaramonte, Jolene Robin-McCaskill, Hannah Ross, Chun-tang Xu, Graduate Research Assistants, Geophysics; Taku Ide, Wenjuan Lin, Carolyn Seto, Graduate Research Assistants, Energy Resources Engineering; Kristian Jessen, Acting Assistant Professor, Energy Resources Engineering; Reginald Mitchell, Associate Professor, Mechanical Engineering.

## Abstract

In this report we summarize progress related to integrated and complementary fundamental studies of CO<sub>2</sub> transport and sequestration in deep, unmineable coal seams. Three parallel suites of laboratory experiments are discussed which aim to measure a number of physical and chemical properties affecting flow, sequestration and monitoring in coal beds. In some cases, the same properties (for example, permeability and compressibility) are being measured on different scales of observation and under different boundary conditions, to provide a more complete understanding of coal properties. Findings to date from four modeling studies are presented. These include a theoretical analytical study of multi-phase flow and sequestration and numerical studies of one-dimensional flow that attempt to replicate simulation of flow-through coal pack experiments for calibration. Another modeling study addresses field-scale reservoir simulation studies of coupled ECBM and CO<sub>2</sub> sequestration in the Powder River Basin of Wyoming. Three additional studies are also summarized in this report. The first is a theoretical study with numerical simulations for quasi-continuous monitoring strategies for sequestration in coal. The second one reports field observations of a coal bed fire, which may lead to the potential to utilize CO<sub>2</sub> injection as a technique for extinguishing the fires. The final study is a geomechanical screening study of a potential storage and leakage experiments at the U.S. Department of Energy's National Sequestration Test Facility at Teapot Dome, Wyoming. The analysis of stress, faults, and their responses to CO<sub>2</sub> injection provide guidance for similar situations in coals.

# Table of Contents

<b>Investigators .....</b>	<b>1</b>
<b>Abstract.....</b>	<b>1</b>
<b>1. Introduction.....</b>	<b>3</b>
<b>2. Laboratory Experiments on Coal Properties .....</b>	<b>5</b>
2.1 DARS Measurements of Attenuation and Compressibility .....	5
2.2 Sorption-Induced Permeability Change of Coal during Gas-Injection Processes .	11
2.3 Coalbed Wettability and Relative Permeability.....	15
2.4 Measurements of Static Physical Properties, Ultrasonic Velocity, and Permeability .....	18
<b>3. Modeling Studies of Coal Properties.....</b>	<b>23</b>
3.1 Analytical Modeling of CO <sub>2</sub> Storage and ECBM.....	23
3.2 Numerical Modeling of Gas Flow .....	35
3.3 CO <sub>2</sub> Sequestration and ECBM in Coalbeds of the Powder River Basin .....	41
<b>4. Dynamic Imaging for Seismic Monitoring of CO<sub>2</sub> Storage in Coal .....</b>	<b>53</b>
<b>5. Observations of a Coalbed Fire .....</b>	<b>70</b>
<b>6. Seal Integrity and Feasibility of CO<sub>2</sub> Sequestration in the Teapot Dome EOR Pilot: Geomechanical Site Characterization .....</b>	<b>75</b>
<b>7. Progress.....</b>	<b>84</b>
<b>8. Future Plans .....</b>	<b>86</b>
8.1 Integrated Laboratory Measurements of the Physical and Transport Properties of Coal.....	86
8.2 Analytical and Numerical Modeling of the Flow and Transport Properties of Coal .....	89
8.3 Modeling and Field Studies of Coalbed Fires .....	90
8.4 Simulation Studies of Quasi-continuous Seismic Monitoring.....	90
<b>Publications .....</b>	<b>91</b>
<b>References.....</b>	<b>92</b>
<b>Contacts .....</b>	<b>98</b>

## 1. Introduction

A number of fundamental scientific questions must be addressed before the potential for utilizing deep, unmineable coalbeds for CO<sub>2</sub> sequestration (and enhanced coal bed methane recovery) can be quantitatively assessed. In this report we summarize progress of laboratory, theoretical and field studies investigating the feasibility of CO<sub>2</sub> sequestration in coal and the ability to monitor effectively the distribution of CO<sub>2</sub> in a repository after injection.

In section 2 we review progress related to a suite of integrated laboratory studies that address a variety of phenomena related to the adsorption and transport properties of coal and the effects of pressure, stress, temperature and the presence of CO<sub>2</sub> and other gases on the physical properties of coal. These studies are instrumental to improved simulation of CO<sub>2</sub> sequestration and storage as well as the utilization of geophysical monitoring to verify the integrity of the repository.

Section 3 describes three related modeling studies of CO<sub>2</sub> sequestration. In one study, analytical modeling techniques have been used to study two phase multi-component flow and ECBM. A numerical modeling study of CO<sub>2</sub> adsorption and desorption considers fundamental multi-porosity nature of coal, shrinkage and swelling of the coal and preferential selectivity of gas species and sorption hysteresis. Finally, a field-scale modeling study of CO<sub>2</sub> sequestration and ECBM is presented in the context of parameters obtained by history-matching water and gas production in the Powder River Basin of Wyoming. All studies incorporate adsorption isotherms obtained in the laboratory studies carried out in this project. Realistic estimates of coal shrinkage and swelling are used in the last modeling effort.

Efficient monitoring is an essential component of all CO<sub>2</sub> storage projects. New techniques to accomplish this are summarized in Section 4. These techniques are designed to construct time-lapse subsurface images using relatively low-resolution active seismic imaging in order to reduce the cost of quasi-continuous long-term monitoring.

Sections 5 and 6 outline progress on topics of coal bed fires and CO<sub>2</sub> sequestration in the Teapot Dome EOR pilot project. In the coal bed fire work, we summarize preliminary observations related to a scoping study of fissures developing over the fires and their importance of providing oxygen to assist combustion. The Teapot Dome study addresses two sites in the study area – one where the seal integrity of the fault-bounded target reservoir appears to be ideal for sequestration and the other where leakage along pre-existing faults is expected to occur.

Three principal settings are being considered for geologic sequestration of carbon dioxide – deep saline aquifers, depleted oil and gas reservoirs, and deep unmineable coal seams. Of these, coal bed storage of CO<sub>2</sub> remains the least well understood. While the potential volumes of storage in coal beds are more variable in comparison to the other geological settings, the appreciable coal deposits in the U.S., China, Russia and India, provide important opportunities to sequester CO<sub>2</sub> if coalbeds are indeed a viable storage

setting for greenhouse gases. The work summarized here represents concrete steps related to improved quantitative evaluation of this storage mechanism as well as the potential for cost recovery associated with ECBM.

## **2. Laboratory Experiments on Coal Properties**

There are three laboratory groups currently conducting experiments on coal samples. Jerry Harris is directing an effort to measure the dynamic elastic properties and attenuation of coal. Tony Kavscek is directing an effort to measure adsorption isotherms and study the flow and transport properties of coal. Mark Zoback is directing an effort to measure the static elastic properties and strength of coal, including shrinkage and swelling as a function of gas adsorption. In this section of the annual report, we present our experimental results to date, and discuss our plans for tightly integrating and coordinating our laboratory research efforts.

We plan to take full advantage of the combined capabilities of our laboratory equipment, and tightly integrate our research efforts over the coming year. Both the unique and shared capabilities of each laboratory are shown schematically in Figure 1. The center of the diagram represents our focus on studying the physical properties of coal as a function of gas adsorption and fluid saturation. Overlapping areas of the diagram represent shared research interests, similar laboratory capabilities, and opportunities for independent verification of experimental results.

For example, compressibility is measured at frequencies in the kilohertz range in the Harris laboratory using the DARS system. In the Zoback laboratory, compressibility is measured at the megahertz and sub-hertz frequency ranges, using ultrasonic velocity transducers and strain gauges. Combining the two data sets provides an opportunity to fully describe coal compressibility over the range of frequencies of interest in the field. A second example concerns separating the effects of deformation and adsorption on permeability. The Kavscek laboratory is better equipped to measure the effects of adsorption on permeability, while the Zoback laboratory can simultaneously measure changes in permeability and deformation due to changing effective stress and coal shrinkage/swelling. Combining these results will improve our understanding of how to predict permeability when effective stress and adsorption are changing simultaneously, for example, during injection of CO<sub>2</sub> into a coal bed.

Our experimental activities to date have been divided among several complementary areas of research – low-frequency measurements of compressibility and attenuation, measurements of permeability and wettability as a function of adsorption, and measurements of elastic properties, permeability, and strength as a function of effective stress. The laboratory systems, theoretical developments, and significant results associated with each of these activities are described below.

### **2.1 DARS Measurements of Attenuation and Compressibility**

The speed of sound provides important diagnostic information for a variety of important physical properties of fluids, rocks, and fluid-saturated rocks. One problem that has frustrated the earth science community for years is the large discrepancy in frequency used in traditional pulse transmission measurements (~1 MHz) and field measurements (i.e., 10 Hz - 10 KHz). Issues of frequency dispersion are often raised but most often go unresolved. Traditional laboratory methods of measuring the acoustic properties of say a 1-inch plug fall into three categories: (1) pulsed traveling-waves, where a high frequency

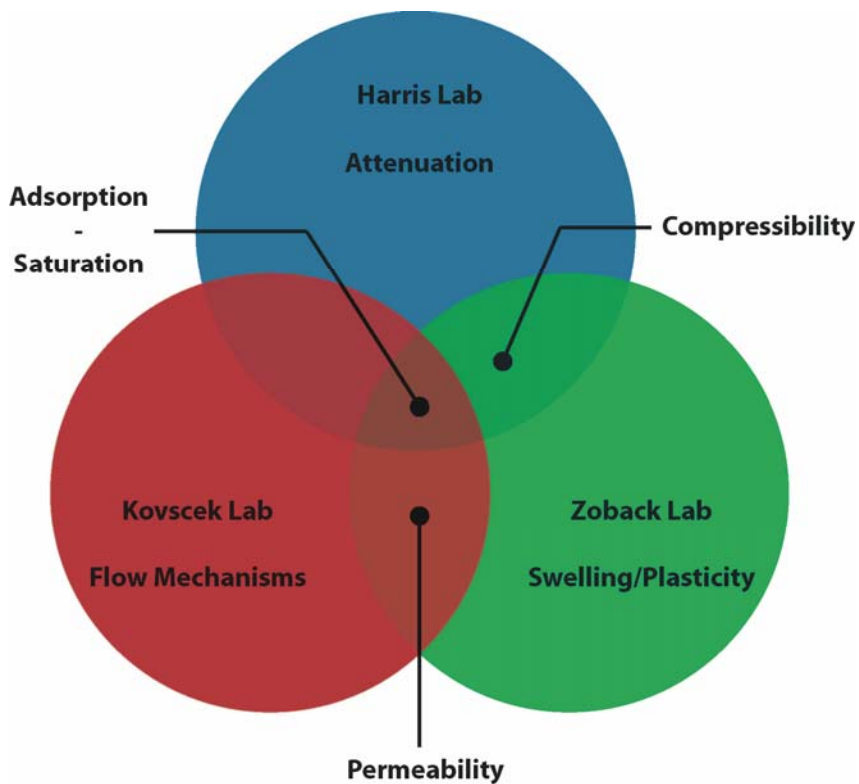


**Figure 1:** Schematic representation of integrated laboratory effort.

pulse (500 kHz - 5 MHz) is transmitted through the sample; (2) vibrating systems, where the natural resonance ( $\sim 50$  kHz) of the sample is excited; and (3) quasi-static stress/strain response. Attenuation is usually a secondary measurement and none of these traditional methods can easily measure small samples at the frequencies used in field experiments. The most popular of these is time-of-flight using pulse transmission in a precision cut sample. Low frequency measurements can be made using resonant bar techniques but these require large samples and are more difficult and expensive than pulse transmission. Moreover, attenuation estimates are very difficult to make from pulse transmission measurements. Our DARS (Differential Acoustic Resonance Spectroscopy) method is a low frequency ( $\sim 1000$  Hz) measurement that can be applied to acoustically small samples, even unconsolidated samples or samples with irregular shape. The primary target of our DARS measurement is attenuation.

Acoustic Resonance Spectroscopy is a well-established methodology used by NIST (National Institute of Standards and Technology) to measure the velocity and  $Q$  of gases. Cavity resonators have been shown to provide a remarkably accurate means of measuring the velocity of sound in gases [93]. The resonant frequency of a cavity is dependent on the size and shape of the cavity and the velocity of sound in the contained fluid. The frequency at resonance can be measured with an accuracy of one part in a million and the velocity of sound easily determined to accuracy better than 0.05% when the cavity dimensions are well characterized. Measurements with precision of 0.003% have been

reported. Moreover, the velocity is easily measured as a function temperature and pressure. The measurement is routinely made at a few kilohertz, e.g., 4 KHz, in the laboratory. This technique is called Acoustic Resonance Spectroscopy or ARS.

We are implementing a variation on ARS, that we call Differential Acoustic Resonance Spectroscopy or DARS. DARS is being developed specifically for acoustically small samples of porous material, namely rocks, and appears to be especially well suited for coal samples, e.g., poorly consolidated and possibly irregular. The DARS principle of operation is quite simple. First we measure the complex resonant spectrum of the simple cavity filled with a fluid. Next, we introduce into the cavity a small sample and measure the change in the complex resonance frequencies, i.e., frequency and Q. A combination of calibration and numerical modeling is then used to extract an estimate of the modulus and Q of the sample. Accurate measurements can be made with DARS for acoustically small samples because the resonances in laboratory-size cavities occur in the hundreds to thousands of Hertz. An example of the resonance data from DARS I is shown in Figure 2. The data measured using DARS is the resonant frequency ( $f$ ), the half-power linewidth ( $W$ ) of the resonance curve, and the amplitude of the resonant curve ( $A$ ).

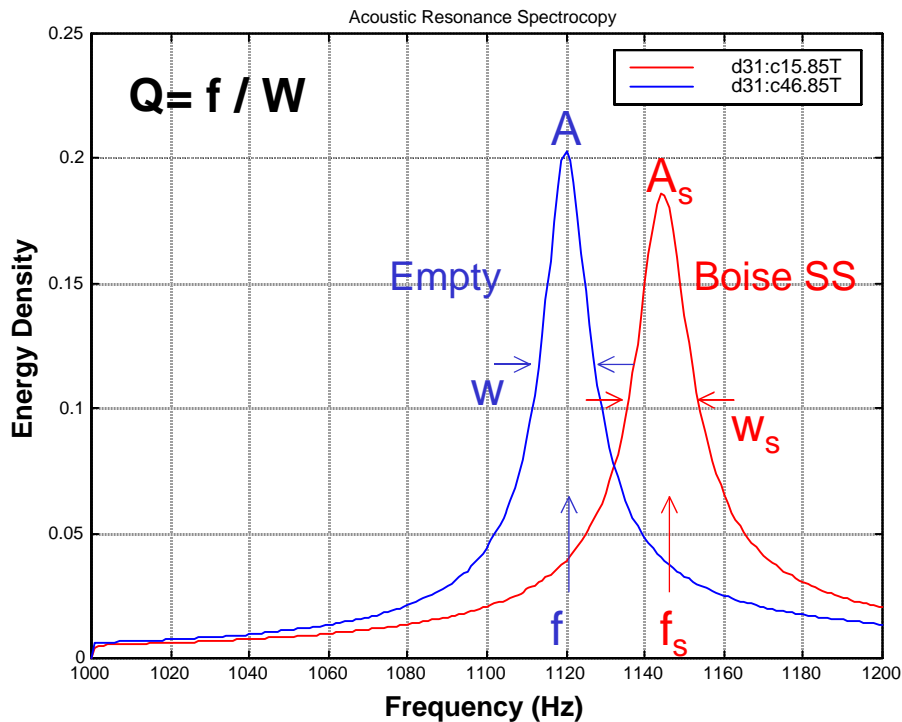


**Figure 2:** DARS I resonance curves for the empty cavity (blue) and the cavity with a small sample of sandstone (red).

DARS II can be used to determine the sound properties at different temperatures and pressures. In summary, DARS is capable of measuring the compressive modulus and loss factor of acoustically small samples under the following conditions:

- (1) Low frequencies on small samples- 100's to 1000's of Hertz;
- (2) Narrow band at a specified center frequency, e.g., 1000 Hz;
- (3) Unconsolidated samples and samples with somewhat irregular shapes;
- (4) Under varying conditions of differential pressure and temperature.

The DARS profile involves moving the sample (relative to the cavity) in manner illustrated in Figure 3. In this way, different combinations of acoustic pressure and velocity can be used to extract different acoustic properties of the sample, namely modulus, density, compressive losses and flow losses.

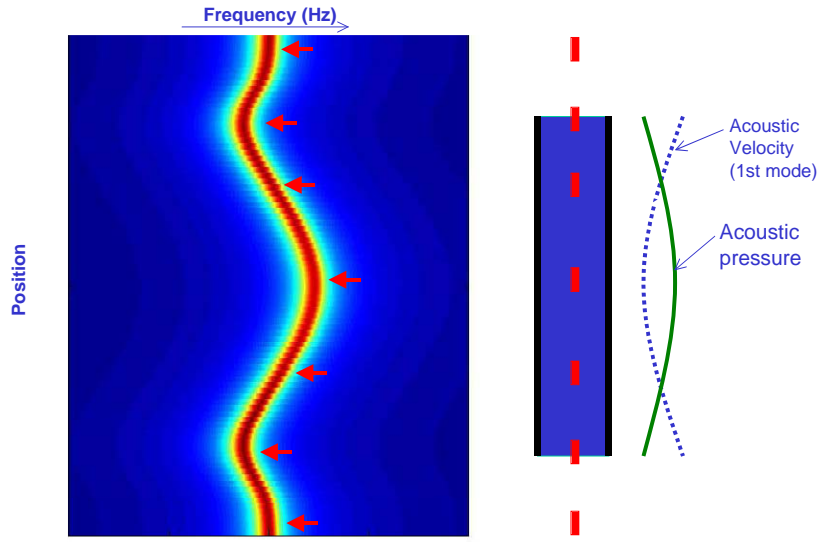


**Figure 3.** DARS I resonance profile, recorded as the sample (red rectangle in the cavity to the right) moves along the axis of the cavity in the varying pressure and velocity fields, allows for the estimation of several acoustic properties of the sample.

#### *The DARS Model*

The resonant frequency of a cavity can be found using the perturbation formula originally developed by Morse and Ingard [95]:

$$\omega_s^2 - \omega_o^2 = -\omega_o^2 \alpha A \langle p^2 \rangle \delta\kappa - \omega_o^2 \alpha B \langle \rho^2 c^2 U^2 \rangle \delta\rho \quad (1)$$

where  $\omega_s$  is the sample-loaded cavity resonant frequency,  $\omega_o$  is the empty cavity resonant frequency,  $\alpha = V_s/V_c$  is the ratio of the sample volume to the cavity volume,  $\langle p^2 \rangle$  and  $\langle \rho^2 c^2 U^2 \rangle$  are the average acoustic pressure and velocity distributions,

$\delta\kappa = (\kappa_2 - \kappa_o)/\kappa_o$  is the contrast in sample compressibility to the fluid,  $\delta\rho = (\rho_2 - \rho_o)/\rho_s$  is the contrast in sample density to the fluid, and  $A$  and  $B$  are system constants (e.g., cavity geometry) determined through calibration with known samples.

We expanded upon the Morse and Ingard derivation to add two important features to the model: (1) sample attenuation, and (2) a double difference formulation for use with a reference sample. For attenuation, we assume that the compressibility and density parameters are complex quantities. Complex compressibility captures compressive losses whereas complex density models losses to fluid flow, e.g., acoustic flow or micro-tortuosity in porous samples:

$$\kappa_r = \kappa_n^r (1 + i/Q_n) \quad (2a)$$

$$\rho_r = \rho_n^r (1 + i/q_n) \quad (2b)$$

where  $Q_n$  is the “quality factor” related to compressive losses and  $q_n$  is the quality factor related to flow losses. The double difference model has the advantage of producing smaller frequency shifts, thus maintaining validity of the perturbation approach for the unknown sample in comparison to the reference sample. (We do not show the double-difference formula here.) The procedure is to first use the frequency shift to estimate the compressibility, and then the linewidth is added to estimate the loss factors  $Q$  and  $q$ .

#### *Dynamic Diffusive Micro-flow*

Xu [94] developed a model for dynamic diffusion or micro-flow of the DARS acoustic fields into porous samples. This result enables estimation of a micro permeability and its connection to the traditional acoustic properties. The result also shows how the DARS fields penetrate and sample the porous sample. This depth of penetration depends on the frequency of the DARS signal and the permeability of the sample and therefore has implications for inhomogeneous samples and the design of DARS II. An example of the pressure distribution (at 1000 Hz) for a permeable sample is shown in Figure 4. This result was computed using a finite element model for dynamic diffusion.

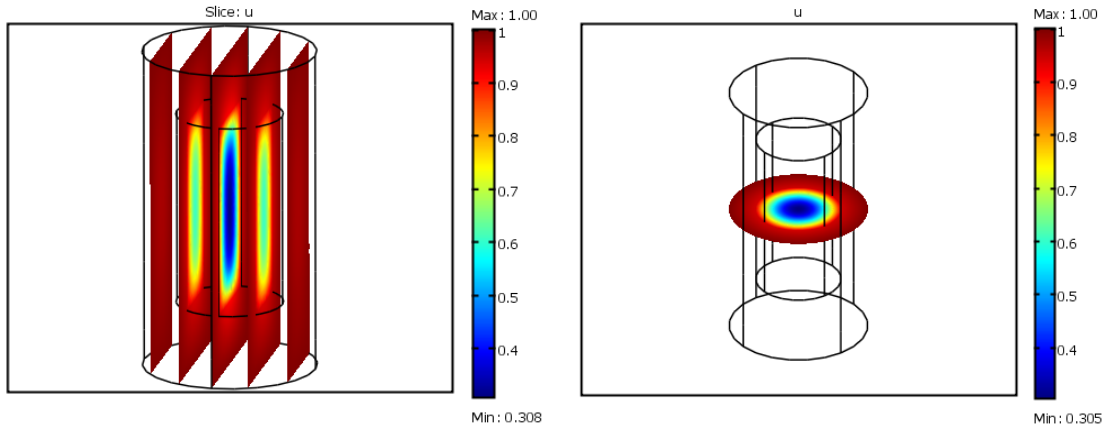


**Figure 4:** DARS diffusion pressure distribution in a cylindrical sample of porous sample estimated using a finite element model Xu [94].

### DARS $Q$ Estimates for Coal Samples

Three samples (Figure 5) were measured with DARS I at room temperature and pressure. The largest sample (#1) is a hard hard semi Anthracite. Samples #2 and #3 are soft sub-bituminous. The smallest sample (#3) is slightly irregular in shape. The DARS responses are shown in Figure 6. The difference curves (5c and 5d) clearly show the smooth changes in frequency and linewidth as the samples are moved through the cavity. These responses were simulated with the perturbation model to yield estimates for compressibility and  $Q$ . The permeability was estimated from the dynamic diffusion model developed by Xu [94]. These estimates are given in Table I. The anthracite sample #1 has the highest value of  $Q$  and lowest value of permeability. The perturbation model does not capture the complicated behavior observed in the linewidth near the ends of the cavity. This behavior is likely due to fluctuations in the acoustic velocity fields that are not well modeled near the ends of the cavity.

The DARS I results shown in Figure 6 and Table I demonstrate the robust and well-behaved nature of the DARS measurements. These are believed to be the first low frequency measurements of  $Q$  on coal samples. Nevertheless, these measurements were made at zero differential pressure and must be updated for in situ conditions using the new DARS II system being built. The DARS II system is discussed in Section 8 Future Plans.



**Figure 5:** Coal samples measured by DARS. See their DARS responses in Fig. 6.

**Table I:** Summary of coal samples measured using DARS I. Permeability was measured for sample #1 but estimated for samples #2 and #3 using the DARS dynamic diffusion theory [94].

Sample #	Comments	Boundary Conditions - Sealed	Measured Volume (in <sup>3</sup> )	Measured Porosity (%)	DARS Estimates		
					Permeability (mD)	Bulk Modulus (Gpa)	$Q$
#1	Hard, semi-anthracite	Yes	1.21	1.9	0.05-0.1	2.84	38
#2	Weak sub-bituminous	No	1.15	7.14	218	3.33	30
#3	Weak, sub-bituminous	NO	0.95	13.9	325	3.06	21

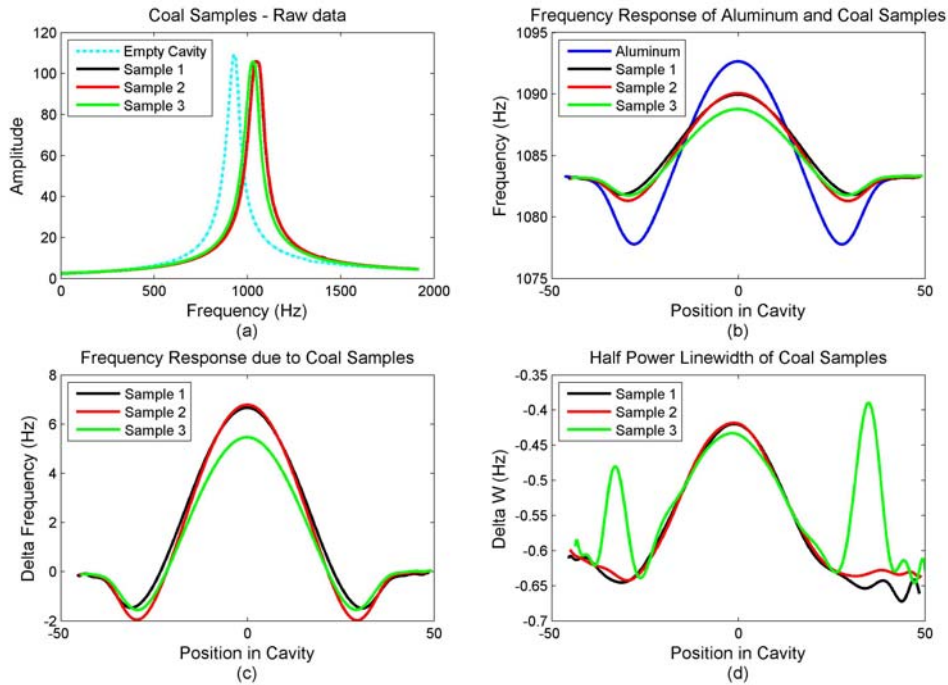


**Figure 6:** DARS I profile responses for three coal samples. (a) Resonance curves; (b) Resonance frequencies; (c) Difference frequencies (cavity perturbations  $\Delta f$ ); (d) Difference linewidths (cavity perturbations  $\Delta W$ ).

## 2.2 Sorption-Induced Permeability Change of Coal during Gas-Injection Processes

The permeability of coal beds changes during gas production and injection. It is believed that two factors induce changes in coal bed permeability [96]. One factor is the effective pressure and the other factor is the adsorption/desorption of gases. For example, the change of permeability in a coal bed during reservoir depletion is the result of two competitive effects [97]. As pore pressure decreases under a constant overburden pressure, the effective pressure increases and permeability decreases due to cleat compression, i.e. closure of the fractures. On the other hand, as the pore pressure decreases, the adsorbed gas desorbs from the matrix of the coal bed. Gas desorption causes shrinkage of the matrix, opening of cleats, and an increase in permeability. The role of effective stress and/or matrix shrinkage/swelling on coal bed permeability has been investigated by many researchers [97, 96, 99, 100]. The goal of our research is to investigate the coal permeability reduction phenomena in the process of gas injection, study gas adsorption on coal, relate permeability reduction with gas adsorption, and build a permeability evolution model useful for simulation of gas injection into coal beds.

### Permeability Reduction

The experimental apparatus is illustrated schematically in Figure 7. The apparatus includes two high pressure gas containers for injected gas and overburden pressure supply, a coal holder system, a pressure regulator, pressure measuring devices, and a flow meter for measuring the gas flow rate. The heart of the setup is the coal holder system. Coal from Powder River Basin (WY) was dried and ground to a particle size of 60 meshes. The ground coal was packed tightly into a rubber sleeve fixed in an aluminum sleeve. The sleeve was then put into a larger stainless steel sleeve to form an annulus for inserting overburden pressure.

Experiments were conducted at a series of increasing pore pressures and a constant net effective stress of 400 *psi* for different gas compositions. The compositions of the injected gases are as follows: pure CH<sub>4</sub>, pure N<sub>2</sub>, pure CO<sub>2</sub>, and 25% CO<sub>2</sub> + 75% N<sub>2</sub>, 50% CO<sub>2</sub> + 50% N<sub>2</sub>, 75% CO<sub>2</sub> + 25% N<sub>2</sub>, and 85% CO<sub>2</sub> + 15% N<sub>2</sub> binary mixtures. The coal pack was first saturated with a test gas at constant pore pressure overnight. Then the test gas was injected into the coal pack at different pressure gradients. The flow rates were recorded when steady flow rate was reached. The permeability of the coal pack was calculated using Darcy's Law (Equation 3) for compressible fluids. The procedure was repeated for all the gas compositions and increasing pore pressures.

$$k_g = \frac{2000\mu_g q_a p_g L}{A[(p_1 + p_2)(p_1 - p_2)]} \quad (3)$$

$k_g$  : Absolute permeability of the coal pack, mD;

$\mu_g$  : Gas viscosity, cp;

$q_a$  : Gas flow at atmosphere pressure, cc/s;

$p_a$  : Standard atmosphere pressure, atm;

$L$  : Length of the coal pack, cm;

$A$  : Cross sectional area of the coal pack, cm<sup>2</sup>;

$p_1, p_2$  : Inlet and outlet pressures of the coal holder, atm.

The results of the experiments are shown in Figure 8. The permeability of the coal pack decreased with the increase of the pore pressure for all gas compositions. That is, permeability decreased as the amount of gas adsorbed increased at constant net effective stress. The amount of permeability reduction varied with gas composition. The permeability reduction was negligible for pure N<sub>2</sub>, greater for pure CH<sub>4</sub> and the greatest for pure CO<sub>2</sub>. When injecting CO<sub>2</sub> and N<sub>2</sub> mixtures, with an increase of CO<sub>2</sub> in the mixture, the permeability decreased markedly, some fraction of N<sub>2</sub> (around 25%) helps to preserve permeability. With the increase of pore pressure, the amount of adsorption increases; and CO<sub>2</sub> has the largest amount of adsorption in comparison to CH<sub>4</sub> and N<sub>2</sub> at

the same pressure [101]. Therefore, we conclude that as the amount of gas adsorbed increases, the permeability decreases.

### Adsorption Isotherms

The extended Langmuir model [102] and the ideal adsorbed solution model [103] were used to calculate the moles and composition of the adsorbed solutions. Both techniques rely on measurement of pure gas adsorption isotherms. The volume of the adsorbed solution was then calculated by multiplying the moles of adsorption with the molar volume of the adsorbed gases. After the volume of the adsorbed solution was calculated, the porosity reduction defined as  $\phi/\phi_0$  was calculated. Porosity reduction assumes uniform coverage of all core pore space. The permeability reduction ( $k/k_0$ ) and the porosity reduction are plotted in Figure 9. Not all the data points fall onto a unique trend. The Reiss cubic relationship between porosity and permeability [104] was not obeyed, however, some exponential relationship seems to exist that depends on gas composition.

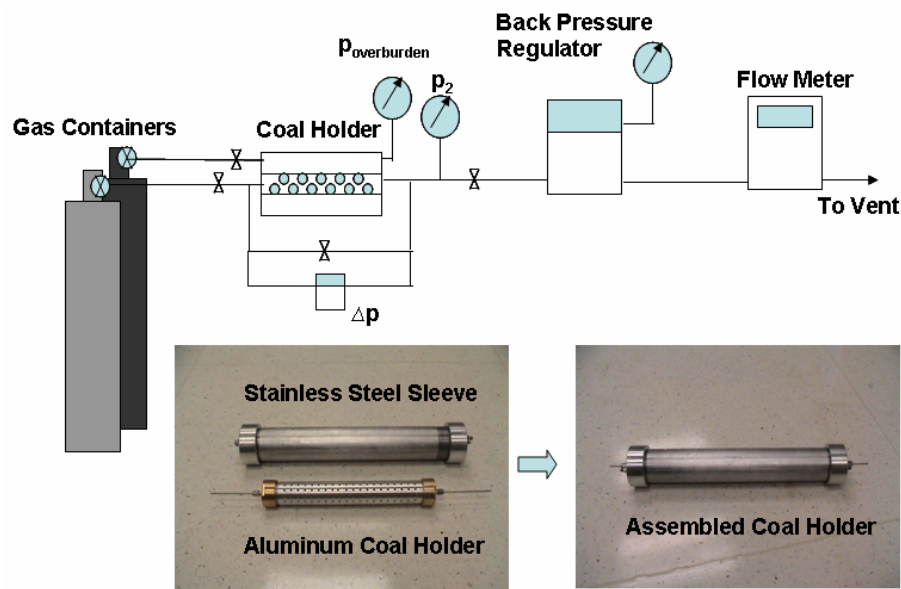


**Figure 7:** Schematic experimental setup for measuring permeability reduction during gas injection.

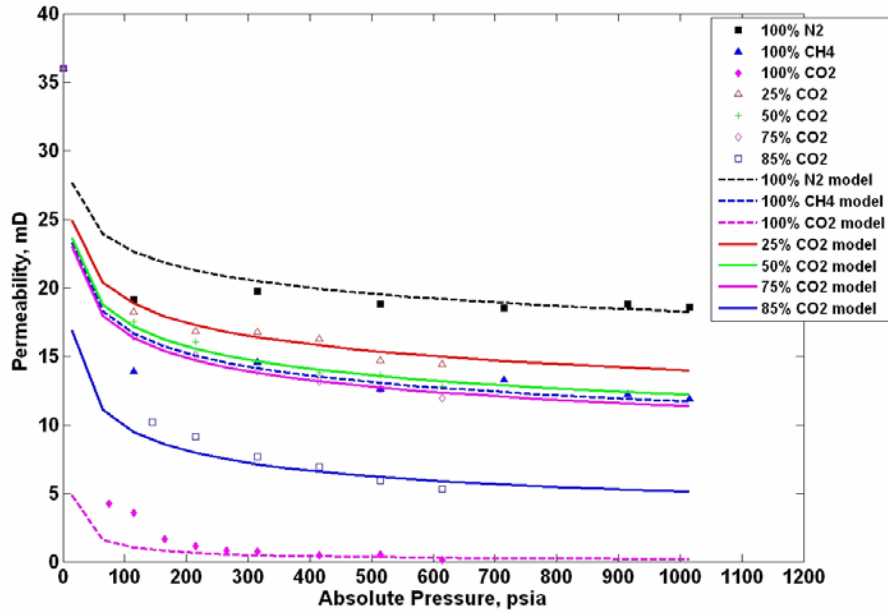


**Figure 8:** Absolute permeability of the coal pack versus pore pressure during injection of pure CH<sub>4</sub>, N<sub>2</sub>, CO<sub>2</sub>, and N<sub>2</sub> and CO<sub>2</sub> binary mixtures. Symbols are experimental data and lines are drawn to indicate trends. The net effective stress was maintained at 400 psi.

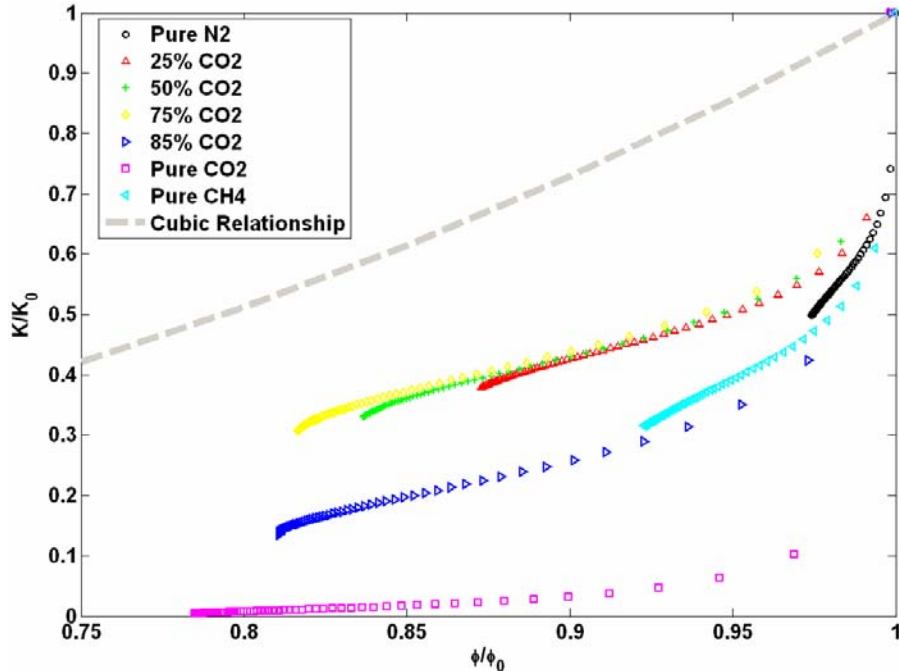


**Figure 9:** Calculated porosity change and experimental permeability change of the coal pack during gas injection.

### 2.3 Coalbed Wettability and Relative Permeability

Study of coalbed wettability is motivated by analytical modeling results, to follow, that show the first order effect of relative permeability on gas-saturation profiles and gas production in one dimension. Secondly, following placement of CO<sub>2</sub> on coal surfaces, water is acidic and the surface properties of coal partially modified by the presence of CO<sub>2</sub>. It is evident that coalbed wettability, as evidenced by the contact angle and gas-water relative permeability, varies with the chemistry of the wetting solution and the coal surface. Therefore spontaneous imbibition of water into coal should be a function of solution pH. As the contact angle decreases, the rate of imbibition increases and *vice versa*. Because wettability determines the relative permeability of a given fluid at the reservoir scale, it is expected that relative permeability curves will also vary with solution pH. Our experimental effort is aimed at verifying the above statements and extracting the multiphase (gas/water) flow properties of coal.

#### *Experimental Setup and Procedure*

Powder River Basin coal samples are first ground to a size-60 mesh (mean size 0.25 mm) and then pressed to develop porous media suitable for imbibition studies. To ensure homogeneity of the sample, low porosity, and low permeability, a custom made press has been designed. Coal cores are then potted with epoxy into acrylic tubes. Cores are placed in a vacuum oven and dried at 25 °C until the weight of the core no longer changes. The dry potted cores are placed in an imbibition cell as illustrated in Figure 10. The imbibition cell is placed within the gantry of an X-ray computed tomography (CT) scanner and CT is used to monitor the progress of water imbibition into dry coal. Experiments are conducted in a counter current mode by circulating water across the face of the coal. Water imbibes spontaneously. The CT Scanner is a Fourth Generation Picker 1200SX. The tube current is 125 mA whereas the energy level is 130 kV. The scan time is 4 seconds.

To date, we have used solutions with pH's of 2.5, 7, and 10. The weight of water imbibed by the core is measured by placing the solutions in a sealed, air-tight beaker on top of an electronic balance. Water that is not imbibed by the core is returned to the beaker. The weight of the beaker is recorded every 30 s and stored on a computer. The core is scanned with the CT every minute initially to capture end effects, and then every few minutes varying from 5 to 30 minutes depending on the solution. At the end of spontaneous imbibition (when the mass of water imbibed becomes constant), a forced imbibition is conducted to completely saturate the core with water. The last procedure is required for processing of the saturation profiles measured by CT as well as computation of the Amott wettability index.

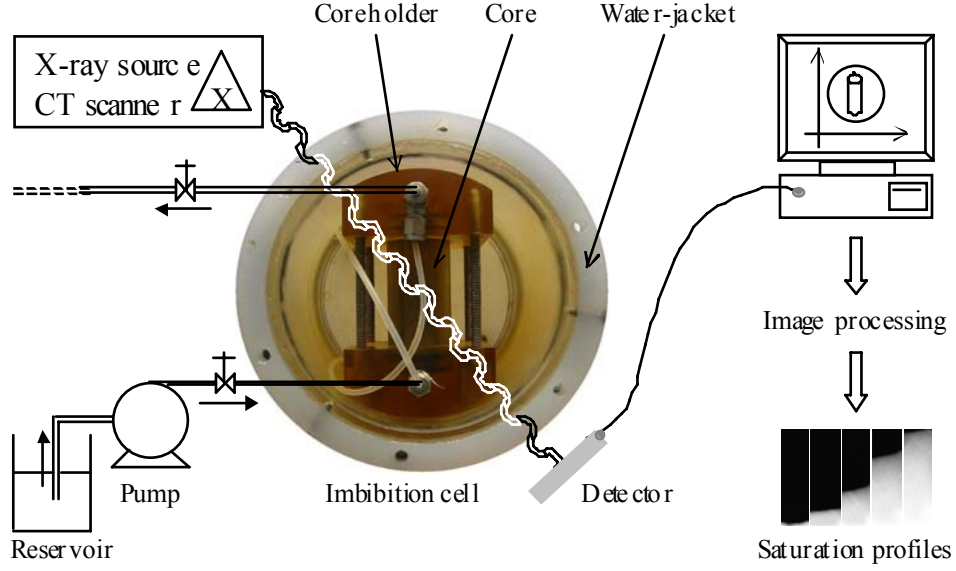


**Figure 10:** Imbibition cell.

The data obtained from CT scanning is processed to obtain one-dimensional saturation profiles as a function of time [107]. Classical water imbibition theory is used to interpret the weight-gain versus time data collected. Handy[108] derived an approximate equation relating the mass of water imbibed,  $m$ , with capillarity and wettability that reads

$$m = \rho_w A \sqrt{\frac{2P_c k \phi S_w t}{\mu}} \quad (4)$$

where  $\rho_w$  is the density of water,  $A$  is the cross sectional area,  $P_c$  is the capillary pressure,  $k$  is the permeability,  $\phi$  is the porosity,  $S_w$  is the saturation,  $\mu_w$  is the viscosity of water and  $t$  is the time. The slope of the lines, with respect to  $t^{1/2}$ , is then equal to  $\rho_w A \sqrt{2P_c k \phi S_w t / \mu}$ . Next, the capillary pressure, Equation (5) is substituted into Equation (4).

$$P_c = \sigma \cos \theta \sqrt{\frac{\phi}{k}} J(S_w) \quad (5)$$

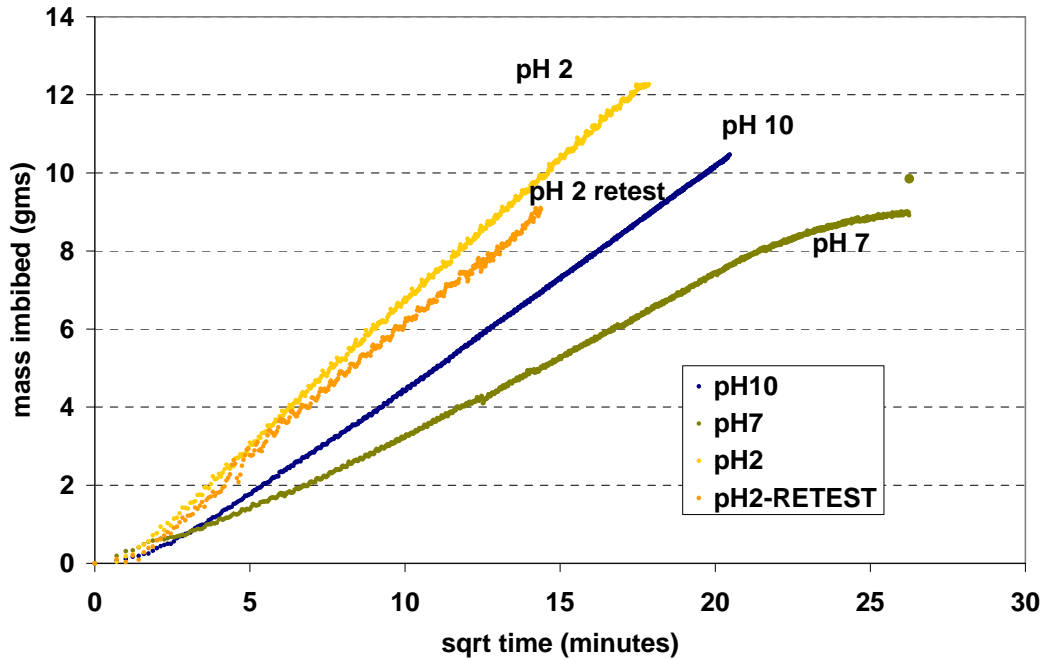
Among different pH solutions,  $P_c$  differs by a factor of  $\cos \theta$  because  $J(S_w)$  is unique for similar coalpacks and the interfacial tension,  $\sigma$ , is sensibly independent of pH. So from imbibition data collected at two different pH's, we obtain the following ratio of mass imbibed

$$\frac{m_1}{m_2} = \left( \sqrt{\frac{\cos\theta_1 S_{w1}}{\cos\theta_2 S_{w2}}} \right) \quad (6)$$

All quantities, except the ratio  $\cos\theta_1/\cos\theta_2$  are measured. These measurements indicate the relative change of contact angle with pH.

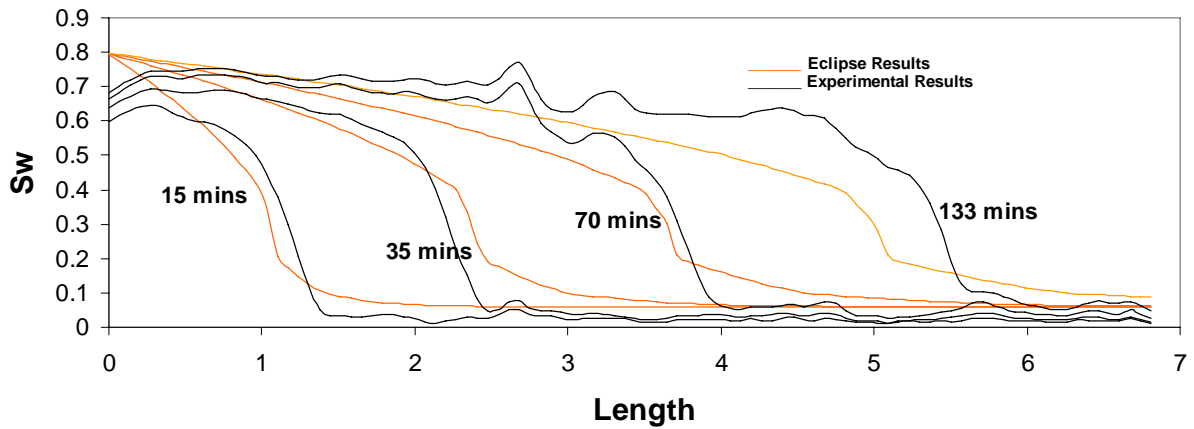
### Results and Discussion

Figure 11 illustrates weight gain profiles for imbibition of pH = 2, 7, and 10 solution. Experiments at pH=2 were repeated with good agreement between individual tests. From the slope of the line at pH=2, the coal is seen to be more water wet under these conditions. We estimate the contact angles as 32°, 75°, and 60° for the pH = 2, 7, and 10 solutions respectively.



**Figure 11:** Mass of water imbibed (g) versus  $t^{1/2}$  at pH 2, 7, 10.

Relative permeability curves also help us to gauge wettability. As a portion of this study we are estimating relative permeability for water-air coal systems as a function of pH using the method of [109]. Figures 12 and 13 summarize experimental results and relative permeabilities for the pH=2 system. Figure 12 presents aqueous phase saturation profiles as measured by the CT scanner superimposed with profiles computed with the relative permeability curves shown in Figure 13.



**Figure 12:** Simulation and experimental aqueous-phase saturation profiles with time for pH-2 (air-water-coal system).

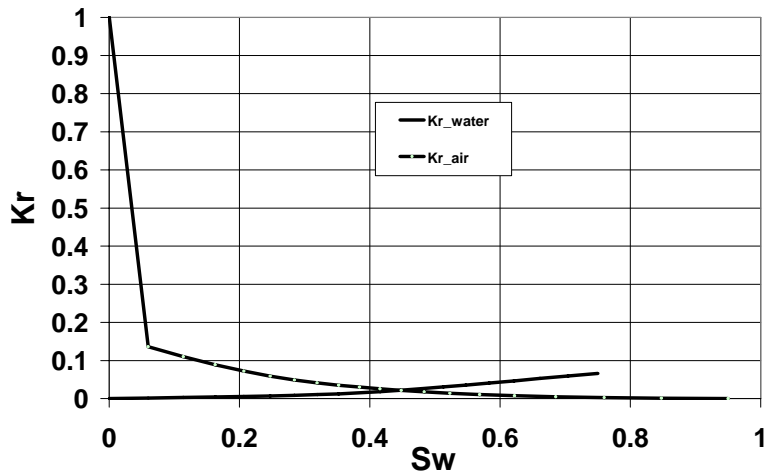


**Figure 13:** Relative permeability curves, pH equals 2, air/water/coal system.

## 2.4 Measurements of Static Physical Properties, Ultrasonic Velocity, and Permeability

Recent coal-bed methane pilot field studies [110, 111] suggest that carbon dioxide injectivity in coal beds may be increased by hydraulically fracturing the coal. Predicting the effect of a hydraulic fracture in a particular coal bed requires knowledge of the fluid flow properties, elastic properties, and strength of both the coal matrix and the cleats. Similarly, numerical simulations [113] of ECBM in the Powder River Basin suggest that injectivity of CO<sub>2</sub> depends on both coal swelling parameters (e.g. [112]) and the elastic properties of the cleats. All of these properties can be measured under a variety of boundary and temperature conditions in our triaxial press. Our experimental work is

focused on measuring the elastic and flow properties of coal and studying the relationship between coal chemistry (i.e. adsorption) and physical properties.

### Equipment Modifications

The laboratory apparatus was modified to optimize its measurement capabilities for experiments on intact coal samples. The most significant modification was the addition of a separate pore fluid sub-system, designed for gas permeability measurements. The sub-system includes two flow controllers that allow either flow or pressure feedback control, a gas analyzer, and a continuous-flow pore pressure intensifier. The new equipment is shown schematically in Figure 14. The other major upgrade to the system was the construction of new coreholders, which give us the ability to measure permeability and ultrasonic velocities simultaneously (Figure 15). In addition, all of the internal seals in the triaxial press were replaced with high-temperature, CO<sub>2</sub> compatible seals, and a new temperature controller was added, for more accurate control at temperatures below 100° F.

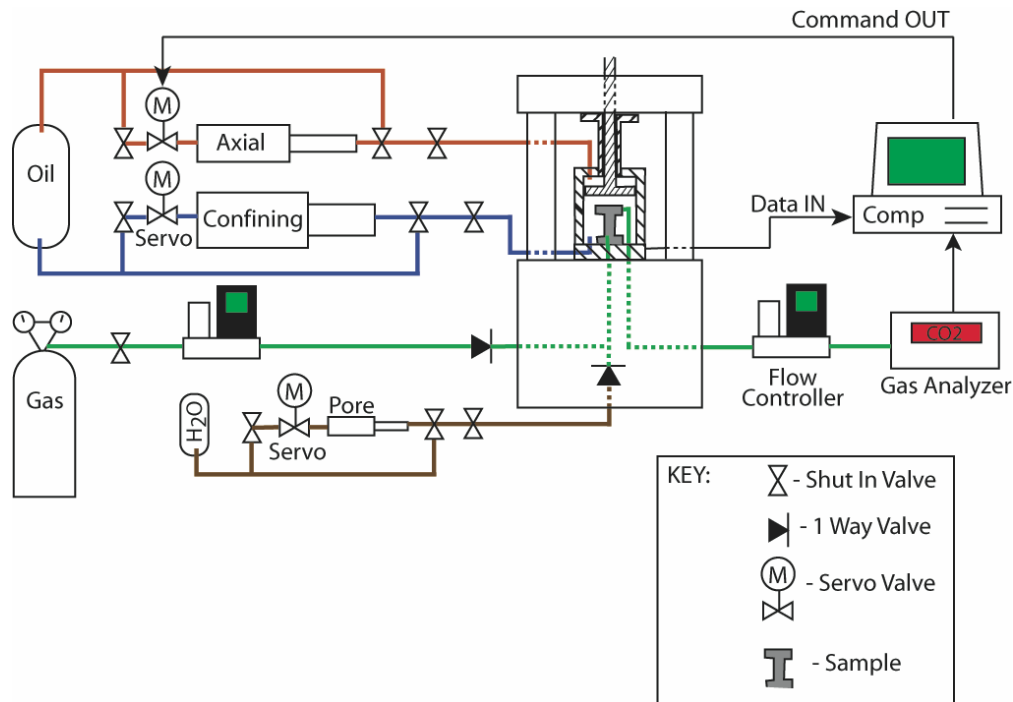


**Figure 14:** Schematic of triaxial press showing modifications to pore fluid line system in order to permit gas permeability measurements.

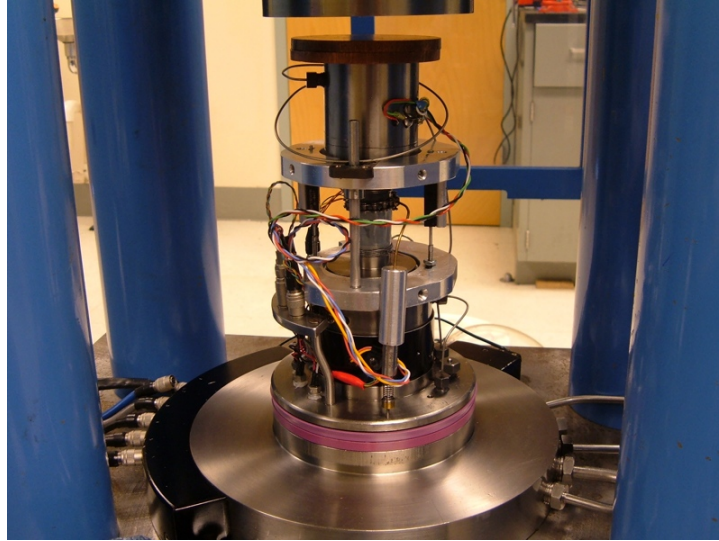


**Figure 15:** Photograph showing modified coreholder assembly, with mounted coal sample. Brightly colored, twisted cables coming from top and bottom coreholders are connected to ultrasonic velocity transducers. Thin steel tubing spiraling around the top coreholder connects the sample to the gas pore line, so that permeability can be measured.

### *Results*

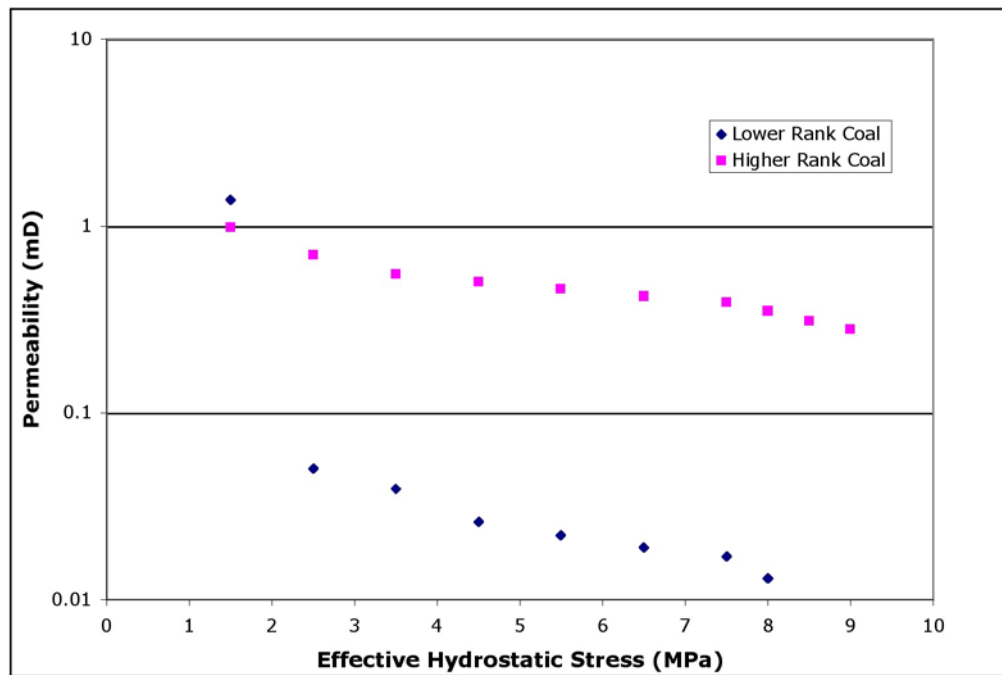
Modifications to the equipment were complete in December, 2006, and since then we have completed several experiments on intact coal samples from the Powder River Basin, Wyoming. Cylindrical coal samples were obtained from 4-inch diameter core either by drilling using a traditional diamond-grit core barrel or by plunge cutting using a tapered-edge core barrel. Due to the numerous cleats and fractures in the core, it was difficult to continuously core long samples, and sample dimensions of 1-inch diameter by 1.75 inches in length were typical. To date, we have concentrated our efforts on establishing baseline elastic and flow properties using helium as the saturating gas. We measured compressibility, ultrasonic P-wave velocity, and permeability as a function of effective stress under both hydrostatic and triaxial boundary conditions, at constant pore pressure. The elastic properties at several values of stress are listed in Table II.

Figure 16 shows Klinkenberg-corrected helium permeability data for two intact PRB coal samples as a function of hydrostatic effective stress during initial loading of the samples to 9 MPa. The pore pressure was taken to be the mean gas pressure across the sample (average of tank pressure and back pressure), and was held constant and equal to 1 MPa by varying the back pressure as needed. Note that the boundary conditions for these measurements differ from those used in the Kovscek laboratory. While their setup is designed to study the effects of adsorption on permeability by measuring permeability at constant effective stress, our system is designed to measure permeability at constant pore pressure. Hence, we are studying the mechanical effects of decreasing matrix porosity on matrix permeability.

Figure 17 shows ultrasonic *P*-wave velocity as a function of hydrostatic effective stress for an intact coal sample for both non-reactive (helium) and reactive (CO<sub>2</sub>) gasses. The sample was first saturated with helium and velocity data were collected as a function of effective hydrostatic stress. After completing this first phase of the experiment, the effective stress was lowered to 1.5 MPa, and the sample was flooded with CO<sub>2</sub>. The sample was allowed to equilibrate for 24 hours before collecting the second set of velocity data as a function of effective hydrostatic stress. Velocity can be seen to increase slightly (a few percent) following CO<sub>2</sub> saturation. Velocity also increases with effective stress, as expected. Pore pressure was held constant at 1 MPa for both both gasses.

**Table II:** Summary of static elastic properties for intact subbituminous Powder River Basin coal samples

Coal Type (Saturating Gas)	K (GPa) @ 5 MPa	K (GPa) @ 8 MPa	E (GPa) @ 4 MPa	$\nu$ (GPa) @ 4 MPa
Higher Rank (Helium)	8.1	11.0	3.6	0.34
Lower Rank (Helium)	1.1	1.2	0.8	0.38
Lower Rank (Carbon Dioxide)	1.6	1.9	1.0	0.4



**Figure 16:** Helium permeability as a function of effective hydrostatic stress for two intact coal samples from the Powder River Basin, WY. While the initial permeability of both

samples is similar (~1 mD), permeability decreases more rapidly with increasing stress in the more compliant, lower rank sample. Noticeable small axial cracks in the higher rank sample were absent in the lower rank sample.

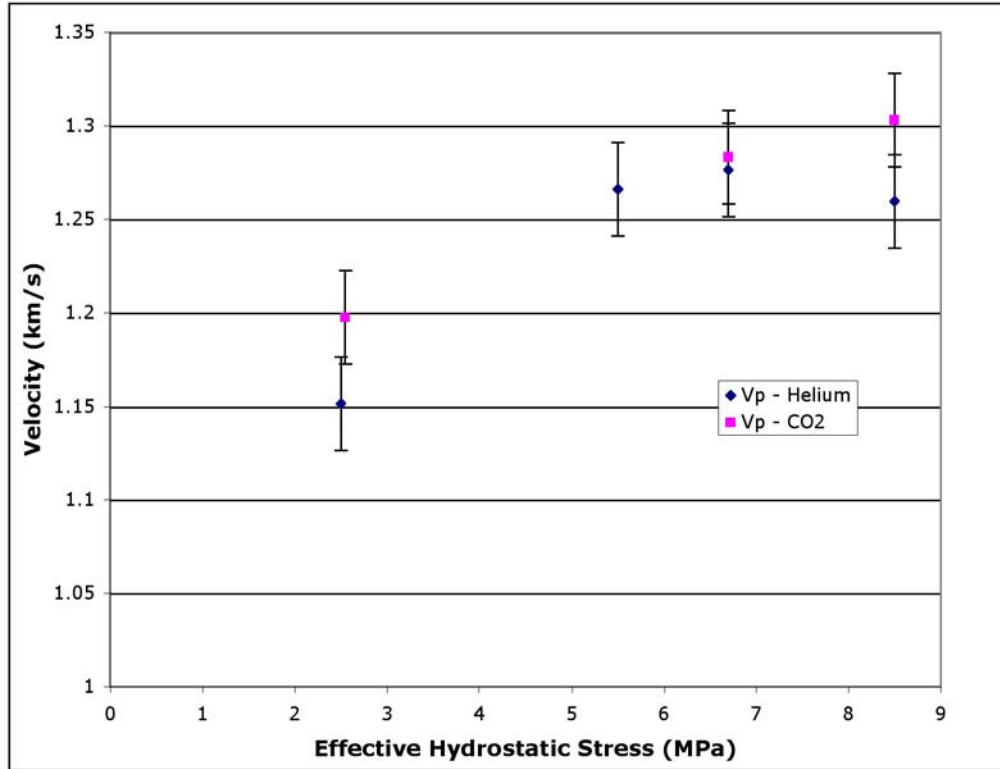


**Figure 17:** Ultrasonic compressional (P) wave velocity data from an intact subbituminous coal sample, as a function of effective hydrostatic stress and gas composition.

### 3. Modeling Studies of Coal Properties

#### 3.1 Analytical Modeling of CO<sub>2</sub> Storage and ECBM

Analytical models are powerful tools for understanding physical mechanisms involved in transport in CO<sub>2</sub> storage in coals and enhanced coalbed methane recovery. In this section, analytical theory developed for two-phase, multicomponent flow in systems with adsorption is applied to understand the effects of undersaturation, sorption hysteresis and relative permeability model parameters on solution structure. For more detailed information on the details of the analytical theory and many results reported previously, please refer to [8].

##### *Undersaturated Reservoirs*

Undersaturated coal reservoirs occur in a number of basins (Powder River, WY, Bowen Basin, Australia, Qin Shui Basin, China). Figure 18 shows the relation between reservoir pressure and gas content for saturated and undersaturated coals on the adsorption isotherm. For a given pressure, undersaturated reservoirs have a lower gas content than the corresponding saturated reservoir. Prior to desorption, the coal must be brought to saturated conditions. In an ECBM scheme, this is achieved by reducing the partial pressure of CH<sub>4</sub> in the coal.

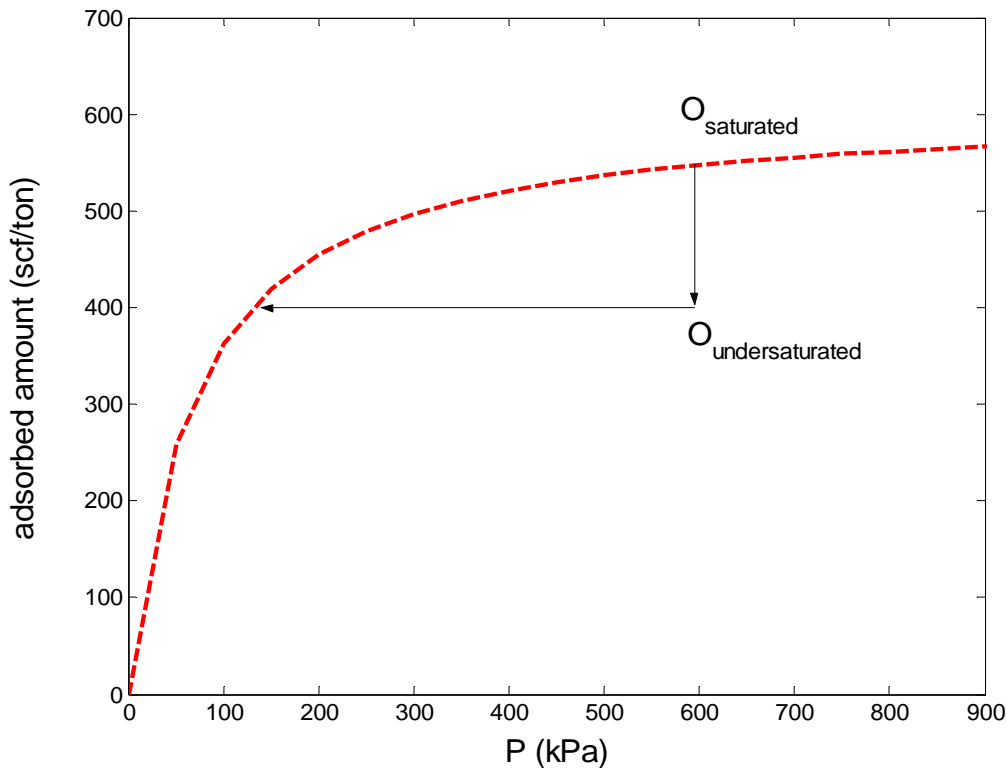


**Figure 18:** Relation between reservoir pressure and gas content for saturated and undersaturated coals.

When conditions are undersaturated, entry from the single phase region into the two-phase region no longer occurs along an extension of a tie line, as it does in systems without adsorption [5]. Solutions are constructed by solving the tie-line composition and gas saturation that satisfy the Rankine-Hugoniot condition. The shock balance from the single phase region to the two-phase region is written as

$$\Lambda = \frac{H_i^I - H_i^{II}}{G_i^I - G_i^{II}}, \quad i = 1 \dots N_c, \quad (7)$$

where

$$G_i = \sum_{j=1}^{N_c} x_{ij} \rho_j S_j + \frac{1-\phi}{\phi} a_i, \quad (8)$$

and

$$H_i = u \sum_{j=1}^{N_p} x_{ij} \rho_j f_j. \quad (9)$$

Substitution of the definitions for  $G_i^p$  and  $H_i^p$  into Equation 7 gives

$$\Lambda = \frac{u_D^I x_i^I \rho_D^I - u_D^{II} [f^{II} (y_i^{II} \rho_{GD}^{II} - x_i^{II} \rho_{LD}^{II}) + x_i^{II} \rho_{LD}^{II}]}{x_i^I \rho_D^I + \frac{1-\phi}{\phi} a_i^I - \left[ S^{II} (y_i^{II} \rho_{GD}^{II} - x_i^{II} \rho_{LD}^{II}) + x_i^{II} \rho_{LD}^{II} + \frac{1-\phi}{\phi} a_i^{II} \right]}. \quad (10)$$

Rearranging Equation 7 to solve for  $x_i^I$  gives a relationship between the equilibrium phase compositions and the initial composition,

$$x_i^I = \frac{1-\phi}{\phi} \Lambda \frac{a_i^{II} - a_i^I}{\rho_D^I (\Lambda - u_D^I)} + x_i^{II} \rho_{LD}^{II} \frac{\Lambda (1 - S^{II}) + (u_D^{II} f^{II} - 1)}{\rho_D^I (\Lambda - u_D^I)} + y_i^{II} \rho_{LD}^{II} \frac{\Lambda S^{II} + u_D^{II} f^{II}}{\rho_D^I (\Lambda - u_D^I)}. \quad (11)$$

Entry from the single phase region into the two phase region occurs along a tie line extension for two cases:

- The adsorption function is linear, or
- $a_i^{II} = a_i^I$ , thereby cancelling the adsorption contribution. If the isotherm is a function of equilibrium phase composition, along a tie line, the adsorbed concentration is constant, and the adsorption cancels.

The solutions presented in this report use the extended Langmuir isotherm to describe multicomponent adsorption. Nonlinearities in the accumulation term of the governing equation, prevent cancellation of the adsorption terms in the shock balance, and the initial composition is no longer a linear combination of the two-phase equilibrium composition. Figure 19 shows the corresponding initial tie lines for a variety of undersaturated initial conditions.

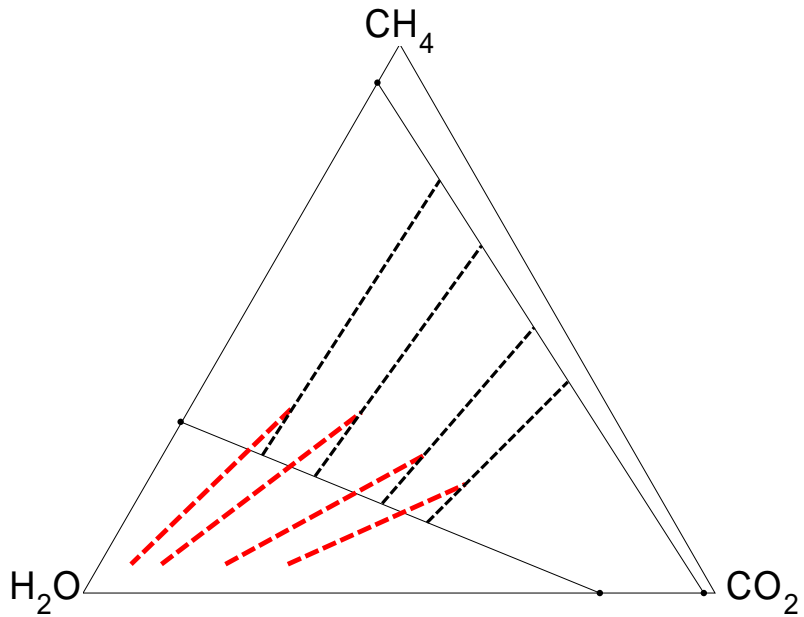


**Figure 19:** Location of the phase change shock from undersaturated initial compositions into the two-phase region relative to the initial tie line. Nonlinearities in the accumulation term prevent the phase change shock from occurring along an extension of a tie line.

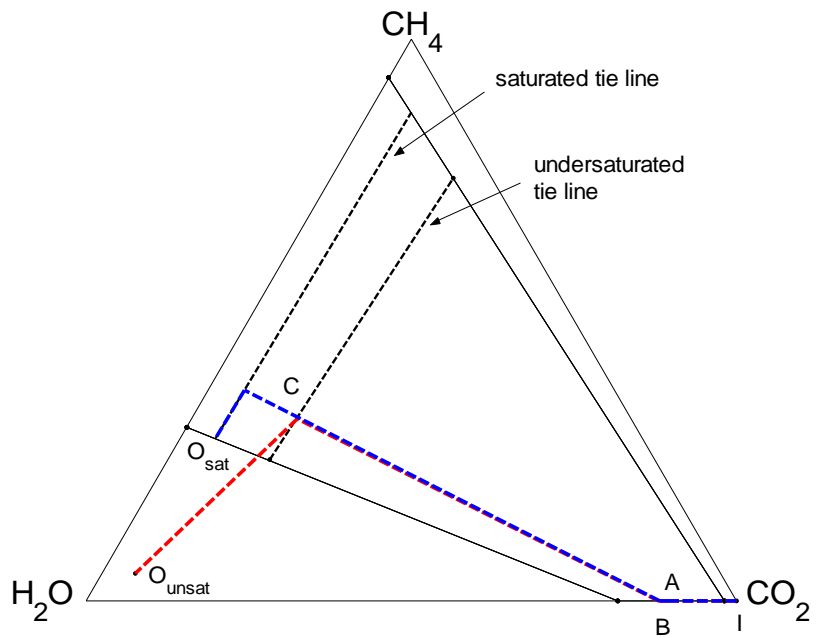


**Figure 20:** Comparison of composition path for saturated (blue) and undersaturated (red) initial conditions.

To illustrate the effect of undersaturated initial conditions on solution structure, injection of 100% CO<sub>2</sub> is injected into a coal with an initial composition of 5% CH<sub>4</sub>, 5% CO<sub>2</sub> and 90% H<sub>2</sub>O (undersaturated initial conditions) and compared against injection into a coal with an initial composition of CH<sub>4</sub>, CO<sub>2</sub> and H<sub>2</sub>O (saturated initial conditions). Composition paths and solution profiles are shown in Figures 20 and 21. In both solutions, the injection tie line remains the same. Upstream of the shock connecting injection and initial tie lines (B-C), the solution is unchanged. In the undersaturated system, less CH<sub>4</sub> is available to be recovered than in the saturated case. The tie line that satisfies the shock balance has a lower equilibrium concentration than that of the tie-line extension. The tie line controlling the initial equilibrium concentrations is lower in CH<sub>4</sub> compared to the saturated system.

In this example, the injection tie line is the shortest tie line, and solution construction starts with a shock from the injection conditions along the injection tie line (I to A). A rarefaction occurs along the injection tie line, from A to B. The new tie line to which a tangent shock connecting injection and initial tie lines is closer to the injection tie line, reflecting the lower CH<sub>4</sub> content of the coal, relative to the saturated case. The undersaturated displacement is slower than the saturated displacement because more gas must be injected to saturate the system before desorption can occur. Gas breakthrough occurs at greater than one pore volume injected. This results in a slower initial recovery in undersaturated coals (Figure 21).

Figure 22 shows the effect of undersaturated conditions on CH<sub>4</sub> recovery. Complete recovery from the saturated coal is slightly slower than the undersaturated coal. The undersaturated coal has less CH<sub>4</sub> available for recovery. The rate of recovery in the undersaturated coal increases rapidly once the bank of CH<sub>4</sub> reaches the outlet. Although the total amount of CO<sub>2</sub> that can be sequestered in undersaturated coals is the same as that in the corresponding saturated coal, if CO<sub>2</sub> sequestration is the goal of the project, injection into an undersaturated coalbed is preferable to injection in a saturated coal. Due to the delay of gas breakthrough associated with the initial injection period to reduce the partial pressure to bring the coal to saturated conditions, more CO<sub>2</sub> can be injected into the reservoir prior to gas breakthrough in undersaturated coals. Moreover, the replacement ratio of CO<sub>2</sub>:CH<sub>4</sub> is greater in undersaturated coals because there is less CH<sub>4</sub> initially associated with the coal for the same amount of CO<sub>2</sub> required to saturate the system. If accelerating CH<sub>4</sub> recovery is the objective, then injection into undersaturated coals is not attractive because of the delayed production response associated with bringing the coal to saturated conditions before CH<sub>4</sub> desorption occurs.

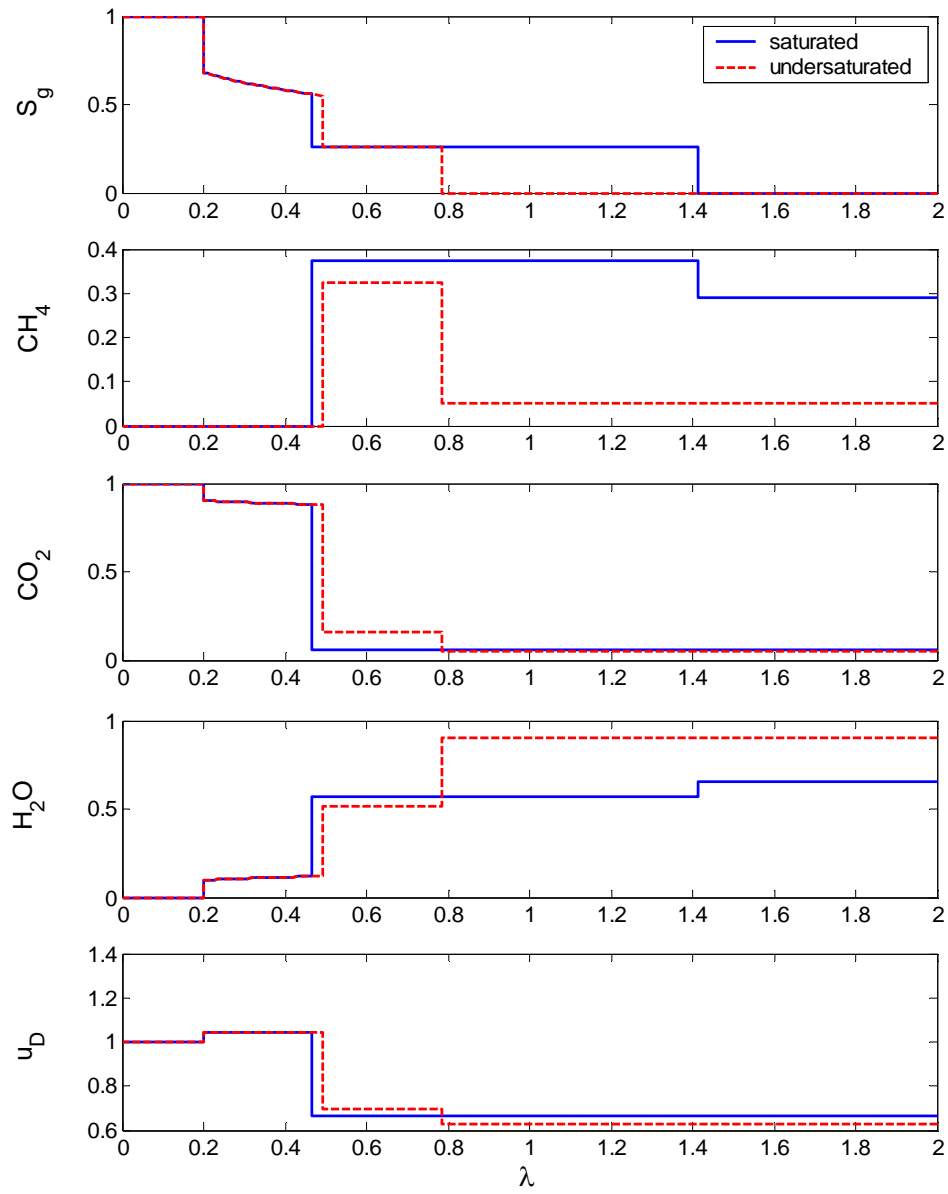


**Figure 21:** Comparison of solution profiles for saturated (blue) and undersaturated (red) initial conditions.

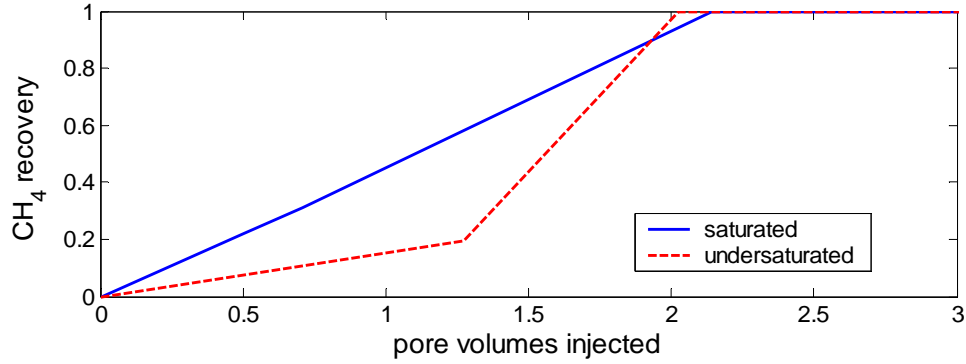


**Figure 22:** Comparison of CH<sub>4</sub> recovery for saturated (blue) and undersaturated (red) initial conditions.

### Sorption Hysteresis

Sorption hysteresis has been observed in pure gas adsorption in some coals [4][1]. This phenomenon is attributed to surface heterogeneities [7]. As gas is adsorbed onto the coal surface, matrix swelling occurs, reducing pore size. On desorption, matrix shrinkage results in increasing the openings of the pore throats. These changes in the matrix as components adsorb and desorb from the surface can create surface heterogeneities that affect the amount of gas adsorbed. This effect is manifest as desorption curves where the loading of gas on coal surfaces is greater than adsorption at the same pressure. Currently no commercial simulators have the capability to model sorption hysteresis. Such phenomena are easily implemented in the analytical model. To incorporate sorption hysteresis in the analytical model, additional conditions on the sorption constants are required:

$$a_{iD} = a_{iD}^{desorb}, \quad \frac{dy_i}{d\eta} < 0 \quad (12)$$

$$a_{iD} = a_{iD}^{adsorb}, \quad \frac{dy_i}{d\eta} > 0 \quad (13)$$

$$a_{iD}^{desorb}(y_i^{max}) = a_{iD}^{adsorb}(y_i^{max}). \quad (19)$$

Adsorption and desorption constants are summarised in Table III. Corresponding isotherms are shown in Figure 23. The adsorption path is shown with the solid line and the desorption path is shown with the dashed line. To illustrate the effect of sorption hysteresis on displacement behaviour, a mixture of 90% N<sub>2</sub> and 10% CO<sub>2</sub> was injected into a coalbed with initial conditions of 31% CH<sub>4</sub> and 69% H<sub>2</sub>O. Figure 24 compares solution profiles for displacements with and without sorption hysteresis.

**Table III:** Adsorption and desorption constants used to model adsorption hysteresis effects.

component	adsorption		desorption	
	$V_{mi}$ (scf/ton)	$B_i$ (psi <sup>-1</sup> )	$V_{mi}$ (scf/ton)	$B_i$ (psi <sup>-1</sup> )
N <sub>2</sub>	272	0.0024	226	0.0053
CH <sub>4</sub>	811	0.0024	609	0.0148
CO <sub>2</sub>	1760	0.0052	1510	0.0292

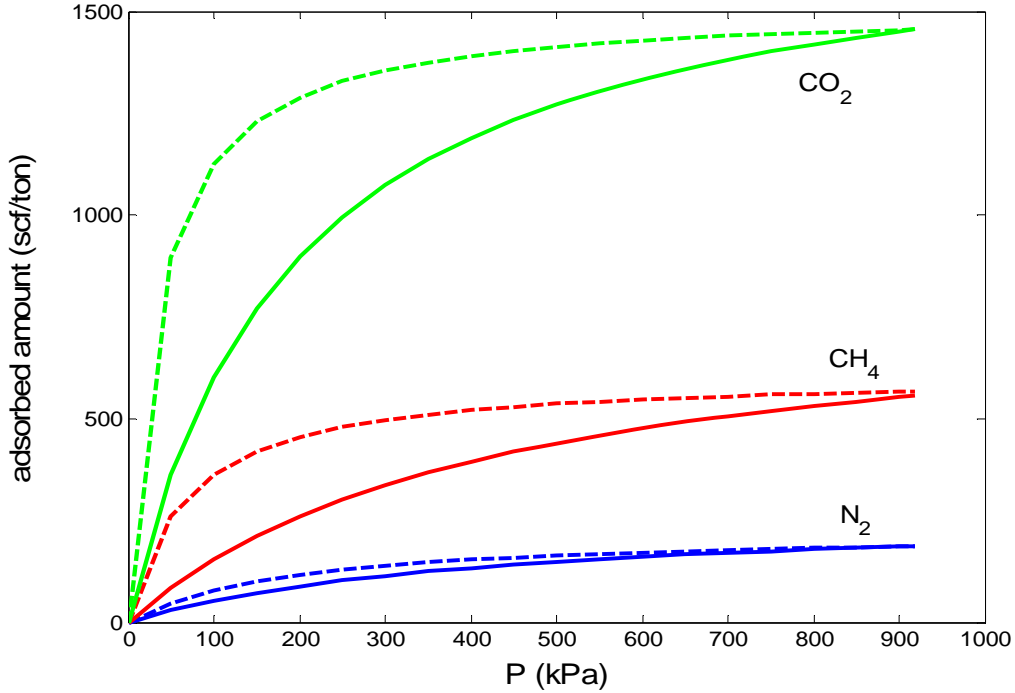


**Figure 23:** Adsorption and desorption isotherms used to model sorption hysteresis.

Sorption hysteresis changes the relative adsorption strength of the gas components, affecting breakthrough and bank arrival times and shifting overall component concentrations. Because initial and injection compositions are fixed, key tie lines of the displacement remain the same and the solution profiles are merely stretched or compressed relative to the case where hysteresis is not considered. When sorption hysteresis is considered, N<sub>2</sub> adsorption strength increases, and the propagation speed on N<sub>2</sub> through the coalbed is decreased. This effect is shown in the broader bank where N<sub>2</sub> desorbs CH<sub>4</sub>, compared to the system without hysteresis. More CH<sub>4</sub> is bound on the coal on the desorption path than on the adsorption path, and therefore, more CH<sub>4</sub> molecules are added to the flowing phase as CH<sub>4</sub> is desorbed than when the adsorption path is used in the displacement. This results in a greater increase in local flow velocity and a faster leading segment.

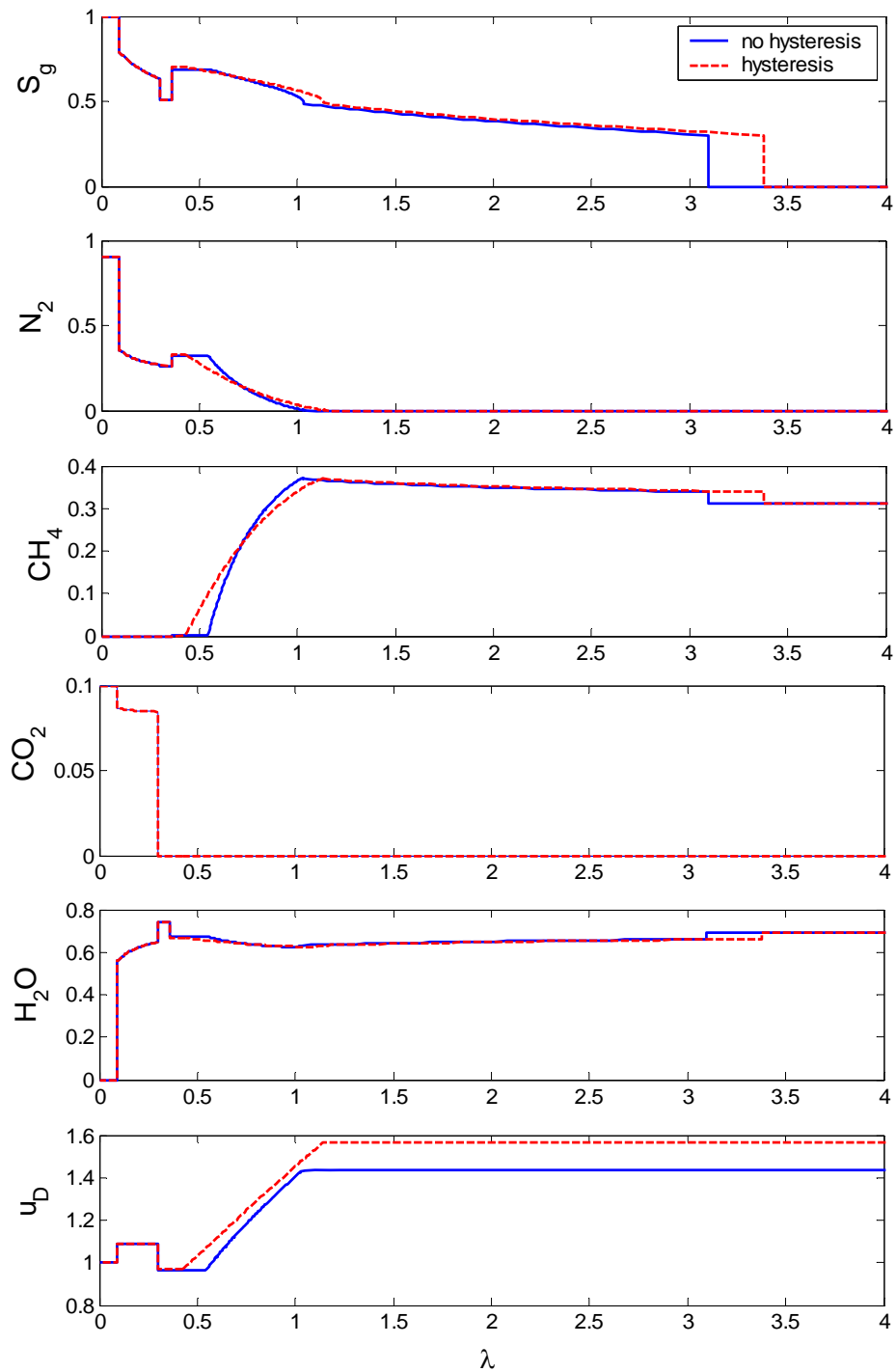


**Figure 24:** Solution profiles comparing the effect of sorption hysteresis.

## Relative Permeability

Many coalbeds are water-saturated. Multiphase flow effects are important in modelling transport in these systems. In this section, the effect of variations in relative permeability on displacement is investigated. Experimental evidence suggests that the coal surface changes from gas wet to water wet during CO<sub>2</sub> injection and high pressure injection (Mazumder *et al.*, 2003, Chaturvedi, 2006). Changes in wettability can be modelled through the relative permeability function, which in turn affects the fractional flow function that models multiphase flow. To examine this effect, two examples are presented: the first examines the influence of the location of the crossover point, and the second shows the effect of curvature of the relative permeability curves. To demonstrate the effect of multiphase flow parameters on recovery, a gas mixture of 50% N<sub>2</sub> and 50% CO<sub>2</sub> injected into a coal saturated with 31% CH<sub>4</sub> and 69% H<sub>2</sub>O is considered.

Quadratic relative permeabilities were used to model multiphase flow.

$$k_{rg} = k_{rgo} \left( \frac{S_g - S_{gc}}{1 - S_{gc} - S_{wr}} \right)^n, \quad S_{gc} < S_g < 1 - S_{wr}, \quad (20)$$

$$k_{rg} = 0, \quad S_g < S_{gc}, \quad (21)$$

$$k_{rg} = 1, \quad S_g > 1 - S_{wr}, \quad (22)$$

$$k_{rw} = k_{rwo} \left( \frac{1 - S_g - S_{wr}}{1 - S_{gc} - S_{wr}} \right)^n, \quad S_{gc} < S_g < 1 - S_{wr}, \quad (23)$$

$$k_{rw} = 1, \quad 1 - S_g > 1 - S_{gc}, \quad (24)$$

and

$$k_{rw} = 0, \quad 1 - S_g < S_{wr}. \quad (25)$$

Parameters are summarized in Table IV, and the corresponding relative permeability curves are shown in Figure 25. RP-1 and RP-2 represent a changing crossover point by changing  $S_{gc}$  and  $S_{wr}$ . RP-1 represents a gas wet system. RP-2 represents a water wet system. For the relative permeability models considered, the structure of the fractional flow curve remains the same: single inflection point, convex to concave for increasing gas saturation. The mobility ratio is fixed at 10. Fractional flow models are shown in Figure 26.

**Table IV:** Relative permeability cases considered.

case	$S_{gc}$	$S_{wr}$	exponent	$k_{rgo}$	$k_{rwo}$
RP-1	0.25	0.025	2	1	1
RP-2	0.05	0.35	2	1	1

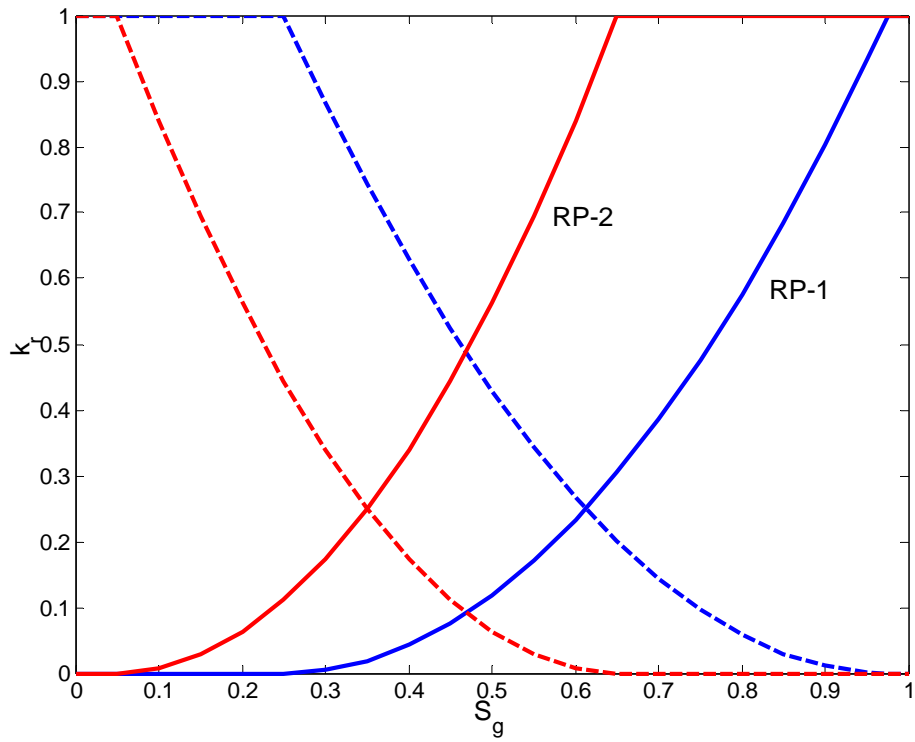


**Figure 25:** RP-1 (gas wet) and RP-2 (water wet) relative permeability curves.

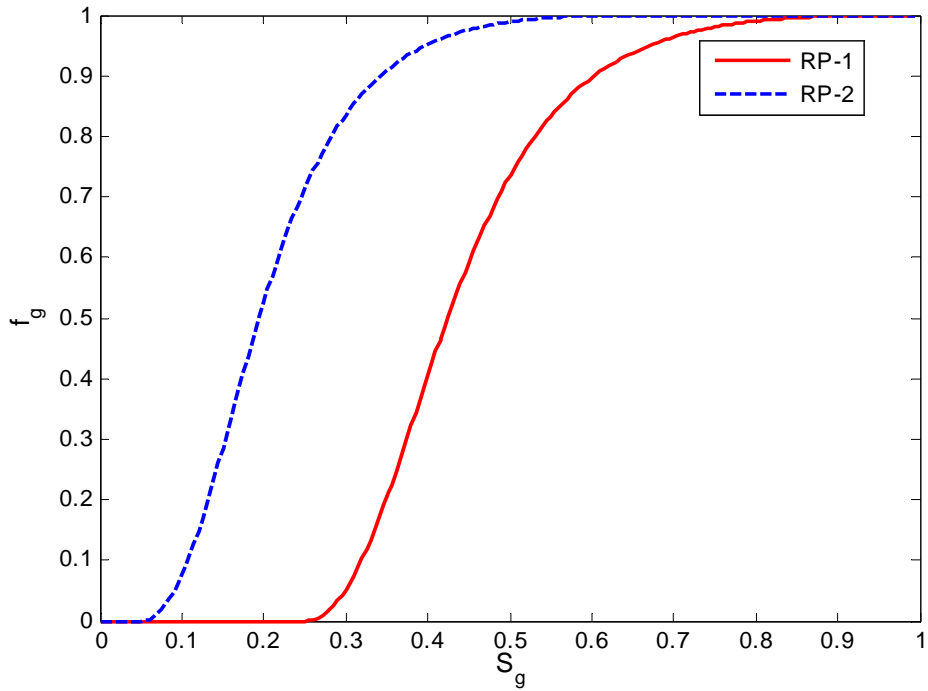


**Figure 26:** Fractional flow curves for RP-1 and RP-2.

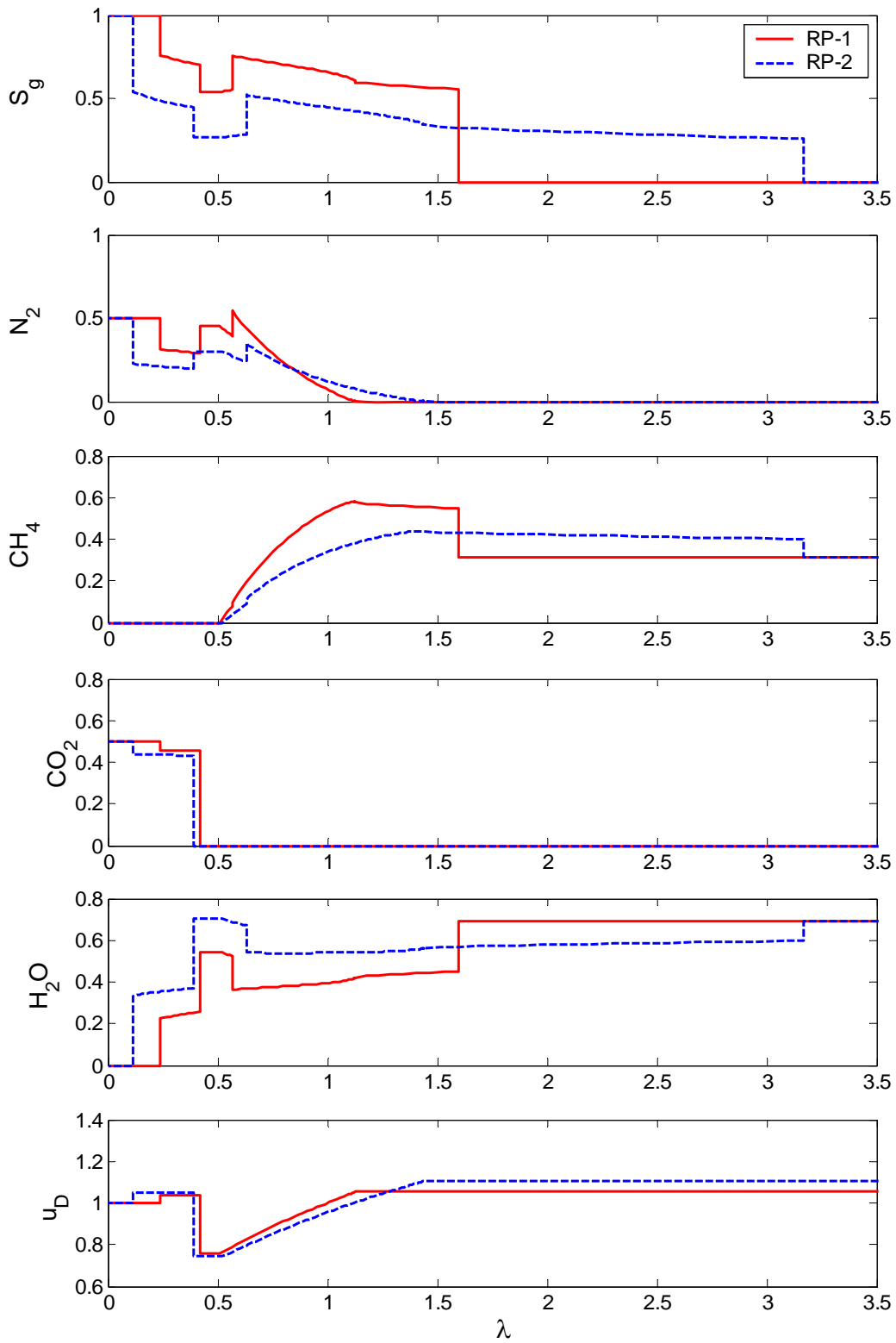


**Figure 27:** Comparison of solution profiles for RP-1 and RP-2 relative permeability models.

The crossover point between gas and liquid relative permeability for RP-2 occurs at a lower gas saturation than that of RP-1 (Figure 25). Gas is more mobile at lower saturations in RP-2 than in RP-1. Chaturvedi [2] observed changes in wettability as a function of pH. When CO<sub>2</sub> is injected into a water saturated coal, CO<sub>2</sub> forms H<sub>2</sub>CO<sub>3</sub>, decreasing the pH of the brine. At high pH, coal was observed to be more water wet than at low pH. This is manifested in the relative permeability curves as a shift of the crossover point to a lower gas saturation. Figure 27 compares solution profiles for the two wettability cases. To demonstrate the effect of multiphase flow parameters on displacement, a gas mixture of 50% N<sub>2</sub> and 50% CO<sub>2</sub> injected into a coal saturated with 31% CH<sub>4</sub> and 69% H<sub>2</sub>O is considered. The solution profile of RP-1 is compressed relative to the solution profile of RP-2. In Figure 28, the region of gas mobility for the RP-1 model is narrower and shifted to higher gas saturations than the window of gas mobility for RP-2. This translation is reflected in the higher gas saturations accessed in the solution profile. Because the mobile region of the fractional flow function of RP-1 is shifted to the higher gas saturations, the tangent construction for the leading shock results slower velocities than those of RP-2. The critical gas saturation in RP-2 is lower than that of RP-1. Gas is more mobile at lower saturations in RP-2 than RP-1, resulting in a faster displacement because gas is mobile at earlier saturations. There is a small effect on the upstream segments of the solution. At high gas saturations encountered in the trailing edge of the displacement, the variation of wave velocities is relatively narrow compared to the range that occurs at lower gas saturations. When gas is more mobile at lower gas saturations, the leading edge of the displacement moves faster than for a relative permeability model where gas is less mobile. As CO<sub>2</sub> injection proceeds, the coal is expected to become more gas wet and the speed of the displacement will decrease as gas is able to fill the smaller pore space as it propagates through the coal, further benefiting CO<sub>2</sub> sequestration efforts.

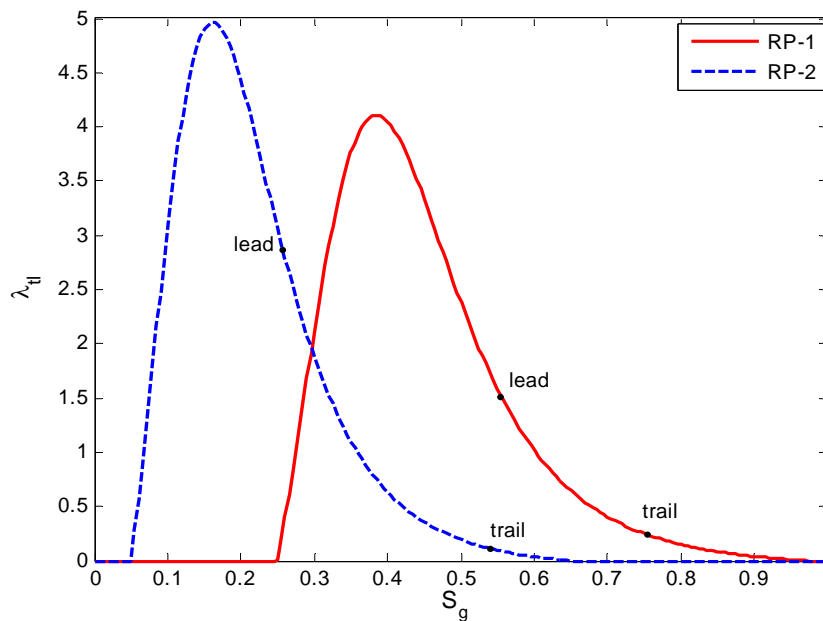


**Figure 28:** Comparison of regions of gas saturations and wave velocities accessed in the displacement.

### *Summary*

Analytical solutions provide improved understanding in the interaction between multiphase flow, phase behavior and adsorption. Sensitivity of the displacement to model parameters, such as relative permeability, adsorption strength, etc..., can be quickly assessed, assisting in the interpretation of laboratory experiments and acquisition of model parameters.

Undersaturated coalbeds are attractive candidates for carbon sequestration. Additional gas is required to reduce the partial pressure of the coal to saturated conditions, resulting in a greater ratio of CO<sub>2</sub> sequestered to CH<sub>4</sub> produced than saturated analogues. A delay in breakthrough of injection gas with the additional gas injection required to bring the coal to saturated conditions, resulting in a longer sequestration project life than saturated coals.

Features of the displacement such as CO<sub>2</sub> breakthrough time and CH<sub>4</sub> bank arrival times are sensitive to parameters in the relative permeability model and adsorption strength. Sorption hysteresis affects the interaction of gas species with the solid surface. When hysteresis is considered, sorption strength on the desorption path is stronger than along the adsorption path, resulting in broader banks of species affected by hysteresis. There is an interplay between the number of molecules of gas added into the flowing phase as gas is desorbed and adsorption strength retarding propagation of compositions.

Changes to surface properties, such as wettability, can be modeled through modification to the relative permeability model. Water wet coals have faster CH<sub>4</sub> production response to gas injection than gas wet coals. In water wet coals, gas is more mobile at lower saturations, resulting in faster breakthrough time. These sensitivities of the displacement to model parameters demonstrate the importance of confidence in model parameter data on understanding the physics of the displacement.

### **3.2 Numerical Modeling of Gas Flow**

Another facet of our coalbed modeling effort is numerical modeling of gas adsorption, desorption, and transport and subsequent validation of the numerical results versus experimental data. Comparison of dynamic results (i.e., versus time) provides an excellent test to gauge whether the details of multicomponent sorption are captured.

The experimental data available for model validation consists of a suite of methane displacement experiments. Various injection gases with compositions that ranged from pure nitrogen to mixtures of nitrogen and carbon dioxide to pure carbon dioxide were injected to displace methane from coal surfaces. The flow geometry is one-dimensional. The coal was ground and then repacked in a Hassler-sleeve type coreholder so that a confining pressure was applied. All experiments results reported here were conducted with no initial moisture within the coal.

Gas sorption isotherms were also collected for the same coal sample for pure gases. Isotherms are displayed in Figure 29. Several features are of note in the figure. First the relative amounts of adsorption are ordered as  $\text{CO}_2 > \text{CH}_4 > \text{N}_2$ . The ordering of the strength of adsorption indicates that carbon dioxide and nitrogen mixtures should be separated within the coal system due to the preferential adsorption of carbon dioxide. Sorption isotherms also display hysteresis that depends on whether gas pressure is increasing or decreasing.

### Model

The conceptual model resulting from interpretation of our relatively simple experiments is rich in physical complexity. Some elements to be captured numerically include:

- multiple porosity of the coal porous medium that ranges from primary porosity within the coal matrix to secondary porosity created by the space between coal particles;
- shrinkage and swelling of the coal matrix as  $\text{CH}_2$  is replaced by  $\text{N}_2$  and  $\text{CO}_2$ , respectively, and these aspects are accommodated within the flow context as changes in porosity and permeability of the coal;
- preferential selectivity of the coal surface by various gas species that leads to chromatographic separation of gas species;
- path dependent sorption hysteresis as indicated in Figure 29.

Our starting points for casting the analytical model are the work and concomitant assumptions of Zhu et al.[9] and existing models of multicomponent gas adsorption. The assumptions are consistent with the experimental results outlined above. The governing equations for single-phase flow of gas species  $i$  in a porous medium including sorption are written

$$\phi \frac{\partial C_i}{\partial t} + (1 - \phi) \frac{\partial a_i}{\partial t} + \nabla \cdot (\underline{v}C_i) = q_i \quad (26)$$

The symbol  $C_i$  is the molar concentration of component  $i$  in the gas phase

$$C_i = y_i \rho_y, \quad (27)$$

where  $y_i$  is the mole fraction of component  $i$  in the gas phase and  $\rho_y$  is the molar density of the gas phase. Next,  $a_i$  is the molar concentration of component  $i$  adsorbed on the coal surface. The adsorbed amount is obtained from pure component isotherms using either the extended Langmuir [10] or ideal adsorbed solution model [11](IAS) isotherms.

Additionally, the ground coal particles have internal porosity. A typical matrix porosity for coal is 2 to 8 % [12, 13] and this porosity is exhibited within coal grains. We term the grain porosity secondary porosity,  $\phi_2$ . Secondary porosity is dead-end pore space

that does not contribute to the overall flow, but participates in the adsorption of gases. The secondary porosity is assumed to be in instantaneous equilibrium with the bulk phase composition of the primary pore porosity ( $\phi_1$ ). Accordingly the overall porosity of the coal packs is written

$$\phi = \phi_1 + \phi_2 \quad (28)$$

As secondary porosity is difficult to measure in our system, it is implemented as the single adjustable parameter in our binary displacements.

Equation (26) is rewritten for one-dimensional (1D) flow, the primary/secondary porosity concept is implemented, and time and distance are nondimensionalized as  $\tau$  and  $\xi$  respectively

$$\frac{\partial C_i}{\partial \tau} + \frac{(1-\phi)}{\phi} \frac{\partial a_i}{\partial \tau} + \frac{\partial v_d C_i}{\partial \xi} = Q_i, \quad (29)$$

with

$$\tau = \frac{v_{inj} t}{\phi L} \quad (30a)$$

$$\xi = \frac{x}{L} \quad (30b)$$

$$v_d = \left( \frac{v}{v_{inj}} \right) \left( \frac{\phi}{\phi_1} \right). \quad (30c)$$

### *Numerical Approach*

The conservation equations were solved numerically using explicit time stepping and single-point upstream weighting of component fluxes. The adsorption and desorption of gas molecules on the coal surface during the displacement of  $\text{CH}_4$  introduces a sharpening behavior of the species concentration within the gas phase that renders the displacement calculations significantly less sensitive to numerical diffusion than traditional convection dominated flows. Hence, no requirement for more sophisticated numerical schemes was suggested to reduce artificial diffusion. Phase properties were predicted by the Peng-Robinson (PR) equation of state (EOS) [14]. For the purpose of evaluating phase behavior, we assumed that the pressure drop along the displacement length is negligible and use the value of the initial pressure throughout the displacement calculation.

As gas is injected into the coal pack and partitions between the coal surface and the free gas phase, new mixtures are formed with partial molar volumes different from the original fluid in place. In addition, gas species adsorb with different affinity to the coal surface, as seen from the sorption measurements. Thus, the porosity is partially filled with immobile adsorbed species. Computationally, the secondary porosity is filled before filling the primary porosity. Accordingly volume change of the adsorbed species on mixing/sorption plays a role and was included in the simulation of the displacement processes.

We approximated the volume occupied by the adsorbed phase ( $V_{\text{ads}}$ ) using

$$V_{\text{ads}} = \sum_i z_i b_i \quad (31)$$

as recommended by Hall et al [15], where  $b_i$  is the hard-sphere, volume of component  $i$  predicted by the PR EOS and  $z_i$  is the mole fraction of component  $i$  in the adsorbate ( $z_i = a_i/\sum a_k$ ). This is, in fact, identical to the procedure used to obtain volume of the adsorbed phase during adsorption/desorption measurements.

As the pressure equation (volume balance) is not solved at each time step during the simulation, an explicit correction of the local flow velocity is applied to ensure simultaneous volume and mass conservation. In the explicit treatment, we carry any volume discrepancy forward in time and correct the velocities of a grid cell  $k$  by [16]

$$v_{d,k+1/2} = v_{d,k-1/2} + \varepsilon \frac{\Delta\tau}{\Delta t} (q_{\text{vc}} - 1), \quad (32)$$

where  $q_{\text{vc}} = V_{\text{fluid}}/V_{\text{cell}}$  and the coefficient  $\varepsilon$  ( $<1$ ) is introduced to ensure stability of the overall numerical scheme.

## Results

Sample results are given first for binary, Figure 30, gas displacements and then ternary, Figure 31, systems. The concentration at the outlet versus the pore volume of gas injected (PVI) is presented. The secondary porosity is adjusted slightly to achieve a match of  $\text{CO}_2$  breakthrough time in binary displacements. Thereafter, no adjustable parameters are employed and the grid is a relatively coarse 25 grid blocks. In Figure 30(a) the results obtained from standard implementation of the extended Langmuir equation are reported. Pure  $\text{CO}_2$  is injected and the figure presents experimental data as symbols and model predictions as smooth lines. Note that the breakthrough time for  $\text{CO}_2$  is underpredicted by roughly 0.5 PV and the shape of the elution of  $\text{CO}_2$  is not represented faithfully by the model. Subsequent implementation of IAS to describe multicomponent adsorption results in nearly exact prediction of  $\text{CO}_2$  breakthrough time as well as the details of the tailout of methane production and the increasing production of carbon dioxide.

Implementation of the extended Langmuir approach for a ternary gas system with injection of a roughly equimolar mixture of  $N_2$  and  $CO_2$  as summarized in Figure 31(a) does yield some of the qualitative features of the experiments, but quantitative agreement is substantially lacking. Notably, the breakthrough time for  $CO_2$  is underpredicted by more the 1 PV. The extent of  $N_2$  banking is similarly misrepresented by the extended Langmuir calculations. On the other hand, IAS results in Figure 31(b) yields much better agreement among experimental and theoretical results. The breakthrough time for  $CO_2$  is almost predicted exactly and the details of the  $N_2$  bank are computed with greater realism. Additionally, the experimental results and both approaches for multicomponent adsorption display chromatographic separation of the injection gas by the coal. Early  $N_2$  production and banking are evident as is the relatively slow movement of  $CO_2$  through the coal.

The IAS approach yields more accurate results because it embodies sensitivity in the concentration of adsorbed species due to changes in concentration of free gas in the pore space as well as pore pressure. The selectivity of various gas species for surface, as predicted by extended Langmuir, is insensitive to free gas concentration and pore pressure.

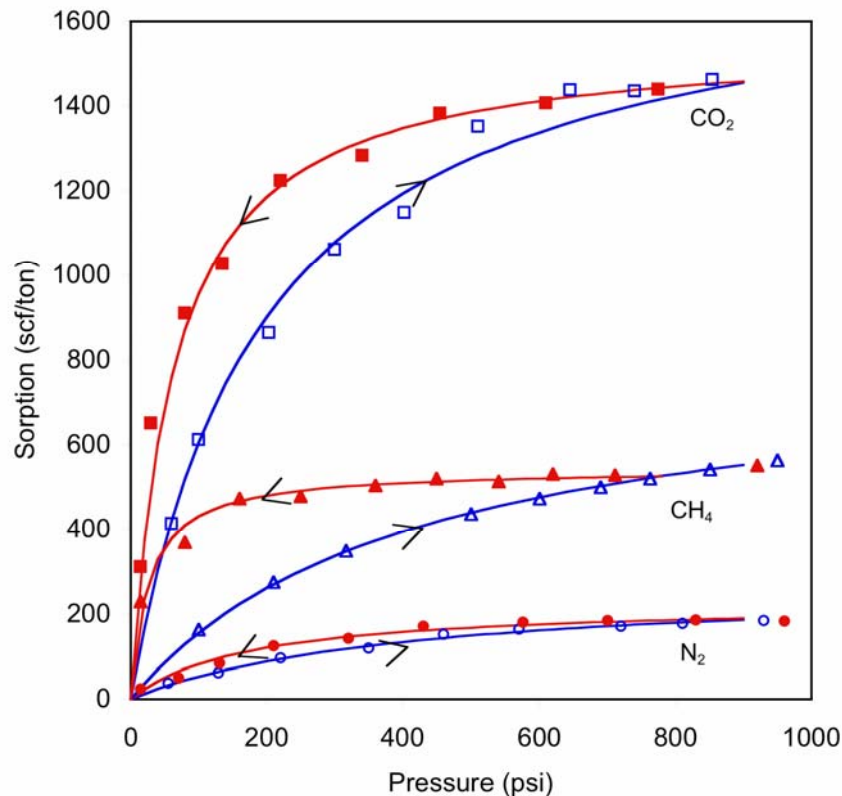


**Figure 29:** Sorption isotherms for pure gases on dry, ground Powder River Basin coal,  $T=22^{\circ}C$ . Arrows in the direction of increasing pressure indicate adsorption whereas arrows in the direction of decreasing pressure indicate desorption.

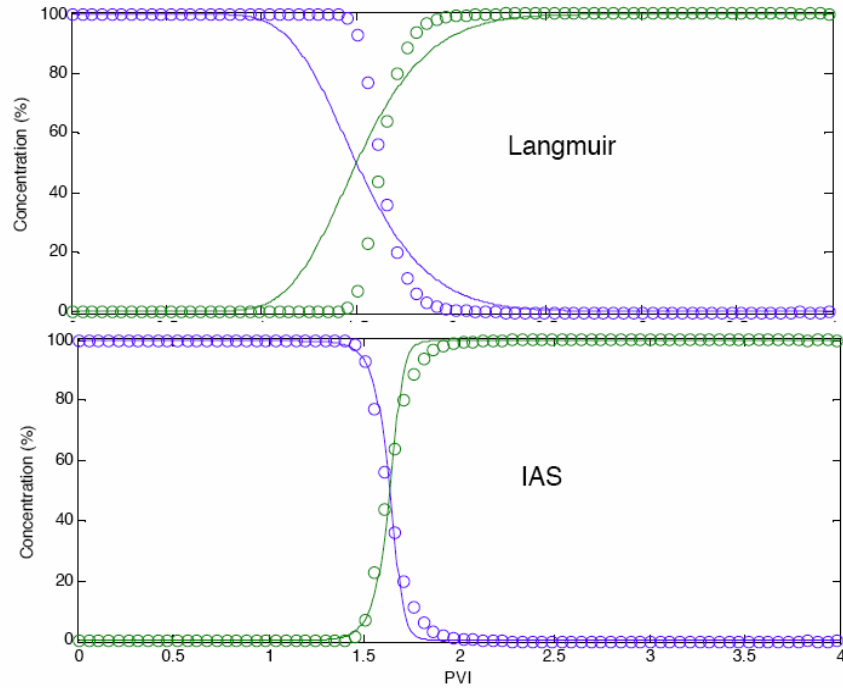


**Figure 30:** Effluent gas concentration resulting from the injection of pure CO<sub>2</sub> into a dry methane saturated coal. Symbols are experimental results and solid lines are numerical calculations. The (a) upper panel employs the extended Langmuir equation and (b) the lower panel employs IAS.

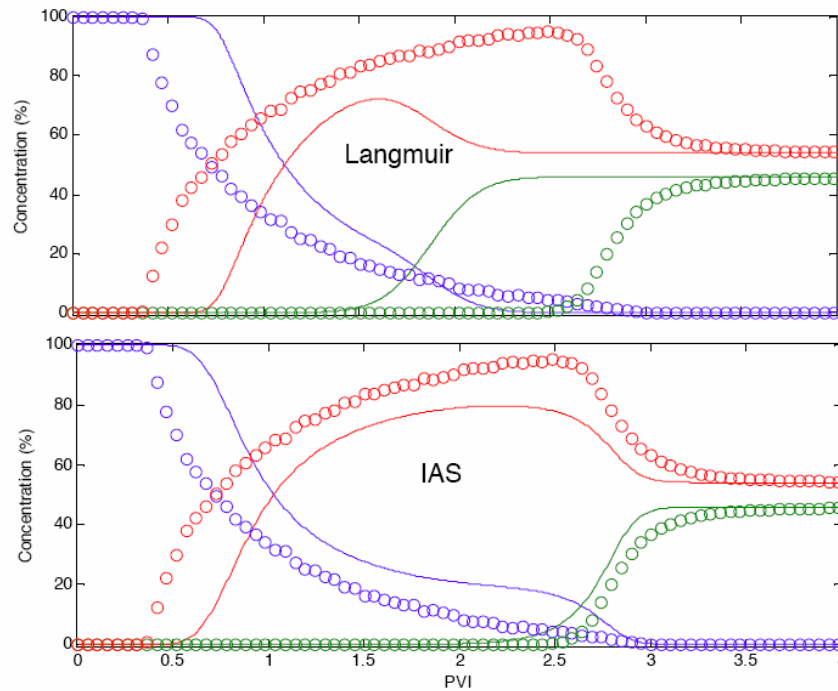


**Figure 31:** Effluent gas concentration resulting from the injection of a mixture of 46% carbon dioxide/54% nitrogen into a dry methane saturated coal. Symbols are experimental results and solid lines are numerical calculations. The (a) upper panel employs the extended Langmuir equation and (b) the lower panel employs IAS.

### 3.3 CO<sub>2</sub> Sequestration and ECBM in Coalbeds of the Powder River Basin

We have examined the feasibility of sequestering CO<sub>2</sub> in unmineable coalbeds by conducting a reservoir characterization study and fluid flow simulations on unmineable coalbeds in the Powder River Basin (PRB), Wyoming (Figure 32). In particular, we were interested in the ECBM potential of CO<sub>2</sub> sequestration and modeling the effects of horizontal hydraulic fractures on CO<sub>2</sub> injectivity. Our study focused on the sub-bituminous Big George coal, part of the Wyodak-Anderson coal zone of the Tertiary Fort Union Formation. A 3D stochastic reservoir model of the Big George coal was constructed in an area of the PRB where the least principal stress is vertical, thereby guaranteeing horizontal hydraulic fractures. We built our model using well logs from coalbed methane (CBM) wells, and populated the model with permeability and porosity values using geostatistical techniques and history-matching.

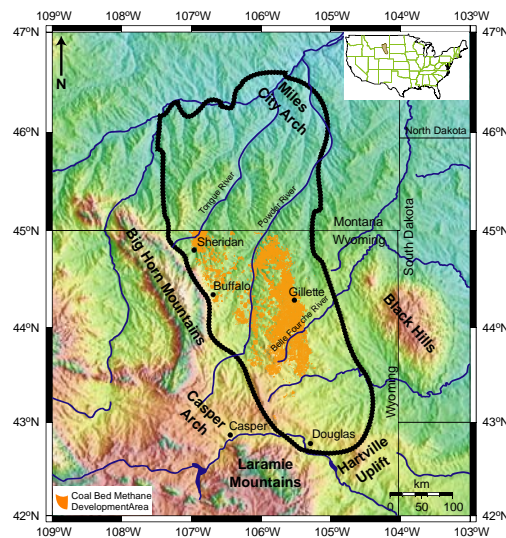


**Figure 32:** Location map of the Powder River Basin, Wyoming (modified from [21]). Orange dots correspond to CBM wells.

#### *Powder River Basin Geology*

The PRB is part of southeast Montana and northeast Wyoming, and is an asymmetrical syncline enclosed by the Bighorn Mountains in the west, the Miles City Arch in the northeast, the Black Hills in the east, the Hartville Uplift in the southeast, and the Casper-Arch-Laramie Range in the southwest (Figure 32). The axis of the basin is close to its western side (NW-SE), with the eastern flank dipping gently to the west at 2-5° and the western flank dipping to the east at 20-25° [23]. The basin is composed of Upper Cretaceous barrier shoreface-marine sandstones and shales, and overlying Upper Cretaceous and Tertiary marine and fluvial deposits [24]. The Tertiary units contain the coal-bearing Fort Union (Paleocene age) and Wasatch (Eocene age) formations, which were deposited in mires connected to fluvial systems that were fed from highland plateaus [24]. The Tongue River Member of the Fort Union Formation is the primary coal-bearing unit of the PRB and is composed of interbedded sandstone, conglomerate, siltstone, limestone and coal [17, 23]. The coalbeds range in thickness from a few

centimeters to 61 m, are elongate to lenticular in shape, and hundreds of meters to tens of kilometers in lateral extent [23, 24].

### *Reservoir Characterization*

We have focused our study on the sub-bituminous Big George coal, which is located in the central part of the PRB, is an amalgamation of five coalbeds and is part of the Wyodak-Anderson coal zone of the Tongue River Member [23]. The average depth of the Big George coal is 335 m and it varies in thickness from 14 to 62 m. Cleat spacing in the Wyodak-Anderson coal zone ranges from less than a cm to 12 cm and face cleat orientation varies from NE to NW [24].

We used water enhancement tests and gamma ray logs to characterize the Big George coal in our study area. Gamma ray logs from active CBM wells gave us the depth and thickness of the coal, and water enhancement tests were analyzed to determine the direction of hydraulic fracture propagation in the coal. Water enhancement tests are used by CBM operators in the PRB to connect the CBM wells to the natural coalbed fracture network. During these tests it has been found that the operators are successfully hydraulically fracturing the coal and in some areas the hydraulic fractures propagate vertically, whereas in others they grow horizontally [21]. Knowing where vertical hydraulic fractures will form in the coal is especially important when choosing a site for CO<sub>2</sub> sequestration because hydraulic fractures that propagate vertically may penetrate the overlying strata, creating potential leakage conduits for CO<sub>2</sub>, and are therefore areas undesirable for injecting CO<sub>2</sub>. We constructed our 3D model of the Big George coal in an area of the PRB where Colmenares and Zoback [21] observed horizontal hydraulic fracture growth (Figure 33).

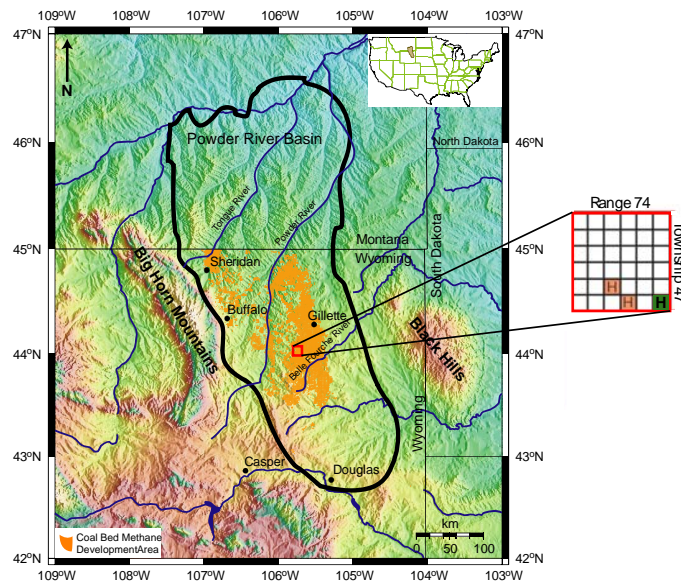


**Figure 33:** Location map of our study area. The red box corresponds to the township and range location of our study area. The green square corresponds to the section in which our 3D stochastic reservoir model was built and is in a section where Colmenares and Zoback [21] identified horizontal fracture growth from water-enhancement (H stand for horizontal hydraulic fracture).

### 3D Reservoir Model Construction

In our 3D model the Big George coal is approximately 16 m thick and ranges in depth (to the top) from 315-361 m, with a slight dip to the west. The number of grid blocks in our model is 10332 (42 x 41 x 6) (V). We chose the grid spacing outlined in Table 3.3-I because it optimizes running time and helps maintain numerical stability with a minimal loss of detail.

**Table V:** The dimensions of our simulation grid.

nx	42	dx	20 m
ny	41	dy	20 m
nz	6	dz	Top 3 layers at 4 m Bottom 3 layers at 1.3 m

We used triangular distributions, simple kriging and sequential Gaussian simulation (SGS) to populate our 3D model with equally probable cleat and matrix permeability and porosity realizations (to capture the heterogeneity of the coal and to model the uncertainty in the cleat and matrix permeability and porosity distribution) [105]. Our initial permeability and porosity values came from literature on PRB coal [24, 36, 31, 19, 37]. In addition, Laubach et al. [29] conducted a study on coal cleat properties and observed that face cleat permeabilities can be 3 to 10 times greater than butt cleat or vertical permeabilities. To capture this anisotropy in cleat permeability we forced the butt cleat and vertical permeabilities to be less than the horizontal face cleat permeability (Table VI). For the total cleat porosity per grid block we used constant values, initially set at 0.02, because the simulator does not allow matrix shrinkage and swelling modeling with a variable cleat porosity field.

We constrained the cleat permeability and porosity values further through history-matching water production data from the active CBM wells used to build our 3D model (keeping gas production fixed) [39]. The results of our history-match are detailed in Table VII and the final cleat permeability values are illustrated in Figure 34 and outlined in Table VIII.

**Table VI:** Triangular distribution values for matrix and cleat permeability and porosity.

Property	Minimum and Maximum Value	Mode
Horizontal face cleat permeability	100-500 mD	300 mD
Horizontal butt cleat permeability	10-160 mD	100 mD
Vertical face cleat permeability	10-160 mD	100 mD
Matrix permeability	0.04-0.7 mD	0.5 mD
Matrix porosity	0.011-0.1	0.05

**Table VII:** Results from history-matching water production data from active CBM wells used to build our 3D model.

Production Wells	True Water Production per Month (bbl/month) (WOGCC, 2006)	History-matched Water Production per Month (bbl/month)
Well 1	1768	1699
Well 2	2844	2750
Well 3	1696	1683
Well 4	3153	3198
Well 5	937	1111

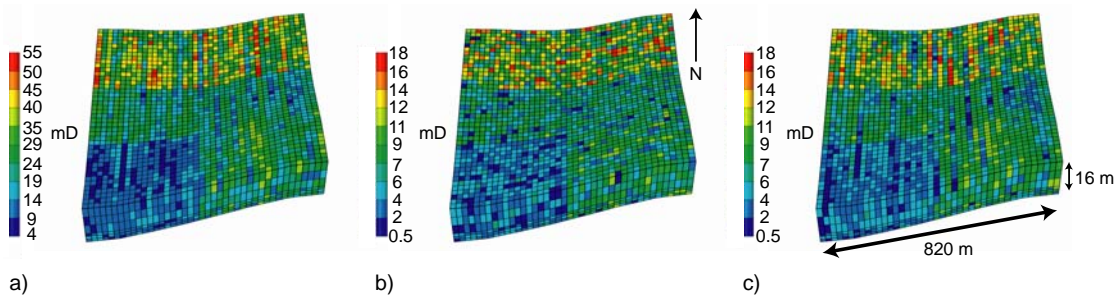


**Figure 34:** a) Horizontal face cleat permeability. b) Horizontal butt cleat permeability. c) Vertical face cleat permeability. This figure shows our 3D model populated with cleat permeability values for one realization. The heterogeneity and anisotropy in coal cleat permeability is modeled using geostatistical techniques. The horizontal face cleat permeability is higher than in the butt cleat and vertical directions [29].

### *Fluid Flow Simulation Set-up*

Reservoir fluid flow simulations were run on a 5-spot well pattern (four production wells at each corner and one injection well in the center) with 80-acre well spacing using the Computer Modelling Group’s ECBM simulator GEM. Our model and simulation input parameters are listed in Table VIII. We have run our base case simulations with pure CO<sub>2</sub> gas injection, with and without coal matrix shrinkage and swelling, and with and without a horizontal hydraulic fracture placed at the base of the injection well. The horizontal hydraulic fracture was modeled as a square fracture with dimensions 100 m x 100 m, porosity of 30%, and permeability of 1000 mD. To prevent accidental hydraulic fracturing of the coal near the injection well, we set the maximum value of the bottom hole pressure (BHP) less than 6200 kPa (900 psi), the fracture pressure in this area [21]. Finally, we assume that the coalbed is overlain by a thick confining unit by using no-flow boundaries in our simulations.

**Table VIII:** Input parameters for our base case fluid flow simulations.

Input Parameters	Values	References
Initial temperature, °C	22	Tang et al. [35]
Reservoir pressure gradient, kPa/m	7.12 (0.315 psi/ft)	Advanced Resources International, Inc. [17]
Coal gas composition	90% CH <sub>4</sub> , 0% CO <sub>2</sub> , 10% N <sub>2</sub>	
Water saturation	99% in cleats, 0% in matrix	[17]
Injector BHP constraint, kPa	4000	Less than the fracture pressure in study area, 6200 kPa [21]
Producer BHP constraint, kPa	1700	History-matching
Cleat spacing, cm	10	Flores[24], Ayers [19]
Matrix permeability, mD	0.04-0.7	[24]
Matrix porosity	0.011-0.1	[17]
Cleat permeability, mD	Horizontal face cleat direction, 4-55, horizontal butt cleat direction, 0.5-18 and vertical direction, 0.5-18	Literature [24, 31,36, 19,29, 37] and history-matching
Total cleat porosity per grid cell	0.017-0.63	Literature [36, 31, 17, 37] and history-matching
Adsorption/desorption parameters for PRB coal samples (dry coal desorption for CH <sub>4</sub> and N <sub>2</sub> and moist coal adsorption for CO <sub>2</sub> )	Langmuir volume: 0.577 gmol/kg for CH <sub>4</sub> , 1.67 gmol/kg for CO <sub>2</sub> Inverse Langmuir pressure, 1.7E-3/kPa for CH <sub>4</sub> , 8.5E-4/kPa for CO <sub>2</sub>	[35]
Diffusion coefficient, cm <sup>2</sup> /s	0.000001 (100 days) for CH <sub>4</sub> and CO <sub>2</sub>	Kovscek and Orr [28]
Rock compressibility	Rock compressibility, 1.45E-7/kPa for matrix and 2.9E-5/kPa for cleats Reference pressure, 2246 kPa for matrix and cleats	Law et al. [30] for matrix and USGS [37] for cleats
Shrinkage/swelling for modified Palmer and Mansoori equation in GEM 2005	Strain Langmuir pressure for CH <sub>4</sub> , 2069 kPa and CO <sub>2</sub> , 345 kPa	Harpalani [26]
	Young's modulus, 0.413E7 kPa	Jones et al. [27]
	Poisson's ratio, 0.39	[27]
	Strain at infinite pressure for CH <sub>4</sub> , 0.007 and CO <sub>2</sub> , 0.013	[26]
	Exponent, 3	Palmer and Mansoori [33, 34]
S <sub>3</sub> , kPa	6200	Colmenares and Zoback [21]

### *Feasibility of CO<sub>2</sub> Sequestration and ECBM in the PRB*

Our first base case simulation is of primary production for 18 years with no CO<sub>2</sub> injection, whereas subsequent base case simulations include CO<sub>2</sub> injection after 5 years of CBM production, with a total simulation time of 18 years. The additional base cases include 1) pure CO<sub>2</sub> injection after 5 years of primary production with no matrix

shrinkage and swelling modeling and no hydraulic fracture, 2) pure CO<sub>2</sub> injection with matrix shrinkage and swelling modeling but no hydraulic fracture, 3) pure CO<sub>2</sub> injection with no matrix shrinkage and swelling modeling but with a horizontal hydraulic fracture placed at the base of the injection well and 4) pure CO<sub>2</sub> injection with matrix shrinkage and swelling modeling and with a horizontal hydraulic fracture placed at the base of the injection well.

Our fluid flow simulations of CO<sub>2</sub> injection into the Big George coal of the PRB suggest that gravity and buoyancy are the major driving forces behind gas migration within the coal, that coal matrix swelling results in a reduction in CO<sub>2</sub> injectivity, and that ECBM results in a significant increase in CH<sub>4</sub> production. Fluid flow maps reveal that the injected CO<sub>2</sub> migrates upwards at first and then along the top of the coal (Figure 35). The upward migration of gas is caused by buoyancy forces, owing to the density difference between injected CO<sub>2</sub> and resident water that create gravity override between the gas and water.

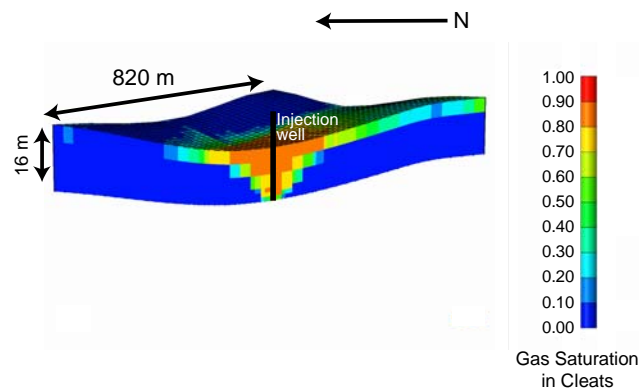


**Figure 35:** Cross section through our simulation model showing gas saturation in the cleats after 13 years of CO<sub>2</sub> injection. Note that the gas rises to the top of the coal before migrating laterally. The figure is from our base case simulation that models matrix shrinkage and swelling but contains no hydraulic fracture.

Our simulations suggest that after 13 years of injection we can sequester ~99% of the total CO<sub>2</sub> injected into the Big George coal, that CH<sub>4</sub> production will be ~5-8 times greater with CO<sub>2</sub> injection than without (depending on the base case scenarios. Figure 36), and that one injection well will be able to sequester ~9 kt of CO<sub>2</sub> a year. Based on this injection rate, it would take ~7,000 injection wells (each with a lifetime of ~13 years) to sequester the current CO<sub>2</sub> emissions for the State of Wyoming (~63 million tonnes/yr (EIA, 2007)). Based on the volume of coal in the PRB (at depths greater than 300m) (Nelson et al., 2006), we estimate that unmineable coalbeds in the PRB can sequester a total of 1.35 billion tonnes of CO<sub>2</sub> (assuming the coal properties everywhere in the basin are the same as in our model). Therefore, at Wyoming's current CO<sub>2</sub> emissions rate the coal resources of the PRB can sequester Wyoming's annual emissions for the next 20 years.

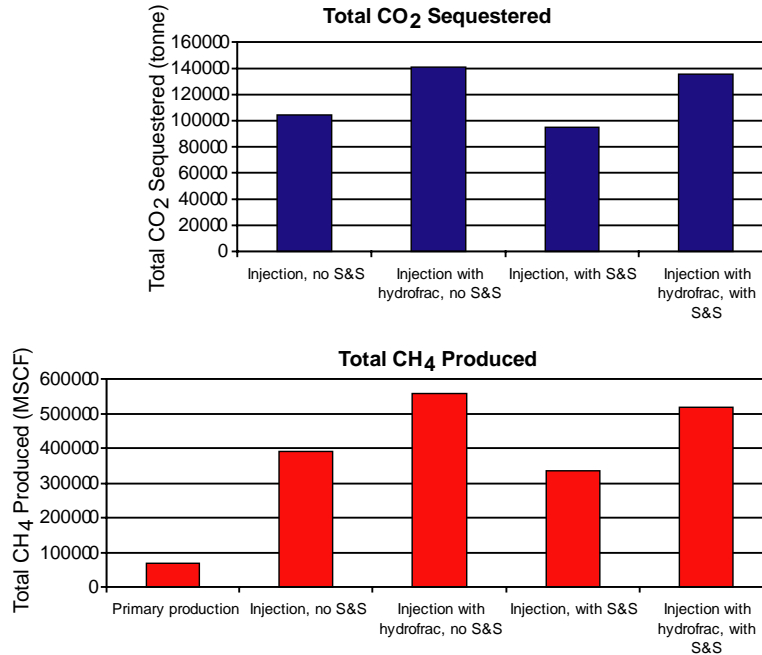


**Figure 36:** Total volume of CO<sub>2</sub> injected and total volume of CH<sub>4</sub> produced after 13 years of CO<sub>2</sub> injection. Hydraulically fracturing the coal at the base of the injection well increased the total volume of injected CO<sub>2</sub> by ~40%. With ECBM there was a ~5-8 fold increase in CH<sub>4</sub> production. Hydrofrac stands for hydraulic fracture and S&S stands for matrix shrinkage and swelling.

Our simulations also show that coal matrix swelling will reduce CO<sub>2</sub> injectivity (~10% reduction in injectivity), but that hydraulically fracturing the coal close to its base will mitigate the negative effect of permeability reduction on injection rate (Figure 36). Placement of a hydraulic fracture at the base of the injection well increased the total volume of CO<sub>2</sub> injected into the coal by ~40% (Figure 36). However, the addition of a hydraulic fracture also led to a ~500% increase in the total amount of CO<sub>2</sub> produced at 6720 days (total simulation time was 6720 days), and breakthrough<sup>1</sup> occurred at 6720 days for the case with a hydraulic fracture and no matrix shrinkage and swelling modeling, but no breakthrough was observed for the case with a hydraulic fracture and with matrix shrinkage and swelling modeling (at the time simulations were stopped there was also no breakthrough in the base cases without hydraulic fractures).

### Gas Buoyancy

As mentioned earlier, gravity and buoyancy are the major driving forces behind gas migration in water-saturated coalbeds. Figure 35 shows CO<sub>2</sub> gas at the injection well migrating to the top of the coal and then flowing along the top towards the production wells. We find that only ~25% of the coal actually comes in contact with the migrating

<sup>1</sup> We define CO<sub>2</sub> breakthrough as the time at which 1% of the total CO<sub>2</sub> injected is produced. We are interested in maximizing CO<sub>2</sub> sequestration, so do not allow recycling of the produced CO<sub>2</sub>.

CO<sub>2</sub> which has important implications for screening models that use the total volume of coal in a basin and CO<sub>2</sub>:CH<sub>4</sub> replacement ratios to determine the CO<sub>2</sub> sequestration capacity of coal-bearing basins. Our simulations show that not all of the coal volume will store CO<sub>2</sub>, so many of the current sequestration volume estimates are probably larger than what can be sequestered in reality.

The gas buoyancy effect is also important for fluid flow simulations used for pilot study screening and prediction. Single layer models will not show the buoyancy effect between water and gas and therefore they underestimate the time to breakthrough and overestimate the total volumes that can be sequestered and produced. We carried out simulations on a single layer model and compared the results against a 6 layer model, using homogenous coal properties for simplicity (Table IX). We observe that after 6720 days the model with one layer in the z direction is able to inject more CO<sub>2</sub> (~10%) and produce slightly more CH<sub>4</sub> (~5%) than the model with 6 layers. However, the largest discrepancy is observed in the breakthrough times between the two models, where breakthrough for the one layer model is at 5420 days compared to 2460 days for the model with 6 layers. If CO<sub>2</sub> sequestration was terminated at the time of breakthrough, the one layer model would predict significantly greater total volumes for sequestration and ECBM over the 6 layer model (325% and 450% respectively) (Figure 37).

We recommend that simulation models contain more than a single layer so that sequestration and ECBM volumes are not overestimated and so that breakthrough is more accurately predicted. This is especially critical for pilot studies, as was seen at RECOPOL, where breakthrough was faster than had been modeled because the simulation model contained only a single layer even though the coals are water saturated [38].

**Table IX:** Coal cleat and matrix permeability and porosity values used in our single layer and 6 layer models (in the z direction).

Property	Value
Horizontal face cleat permeability	100 mD
Horizontal butt cleat permeability	50 mD
Vertical face cleat permeability	50 mD
Total cleat porosity per grid cell	0.07
Matrix permeability	0.41 mD
Matrix porosity	0.05

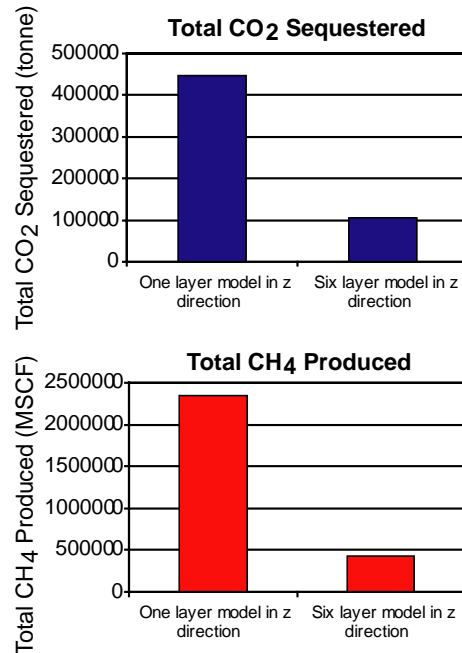


**Figure 37:** Total CO<sub>2</sub> sequestered and CH<sub>4</sub> produced at time of CO<sub>2</sub> breakthrough for the model with one layer in the z direction and the model with 6 layers in the z direction. Both simulations were run with matrix shrinkage and swelling modeling but no hydraulic fracture.

### *Cap rock seal*

Coalbeds are an appealing option for geologic storage of CO<sub>2</sub> because the CO<sub>2</sub> is adsorbed onto the coal matrix surfaces and effectively “locked” into the coalbed. However, as we have shown above, buoyancy forces between the gas and inherent water cause the injected CO<sub>2</sub> to rise to the top of the coal and flow along the top to the production wells (Figure 35). CO<sub>2</sub> leakage will not occur if the coal is overlain by a laterally extensive cap rock, but if the cap rock pinches out so that the coal is overlain by sand, the gas may migrate into the overlying sand unit. In the PRB, the coalbeds are typically overlain by a confining unit and it is rare that they are in direct contact with a sand body (J. Wheaton, personal communication, 2007; Applied Hydrology Associates and Greystone Environmental Consultants, 2002; Bartos and Ogle, 2002).

However, we have run a number of simulations looking at the potential leakage of CO<sub>2</sub> into overlying sand units. Our leakage simulation cases include a sand-sand sequence (4 m and 12 m thick respectively) overlying a coalbed (16 m thick) and a shale-sand sequence (4 m and 12 m thick respectively) overlying the coalbed. We have varied the permeability and porosity of the sands and shale to see what effect these properties may have on gas migration into overlying units (we have used constant values rather than

geostatistical distributions for simplicity) (Table X).<sup>2</sup> For the cleat and matrix permeability and porosity distributions for the coalbed we have used our history matched distributions illustrated in Figure 34 and outlined in Table IV.

**Table X:** Sand and shale permeability and porosity values used in each of our leakage scenarios.

Scenario	Stratigraphy	Property	Sand	Shale
1	sand- sand	Permeability (mD)	300	
		Porosity	0.1	
2	sand- sand	Permeability (mD)	70	
		Porosity	0.1	
3	shale-sand	Permeability (mD)	300	0.009
		Porosity (mD)	0.1	0.1
4	shale-sand	Permeability (mD)	70	0.009
		Porosity (mD)	0.1	0.1
5	shale-sand	Permeability (mD)	70 in x-y; 7 in z	0.009 in x-y; 0.002 in z
		Porosity (mD)	0.1	0.1

The simulation grid used in this analysis contains 14256 grid cells, with 36 in the x direction, 33 in the y direction and 12 in the z direction. The grid dimensions are outlined in Table XI. We use a 5-spot well pattern (4 production wells surrounding one injection well) with 80-acre well spacing, and inject CO<sub>2</sub> for 18 years, as soon as production begins. The production wells are only completed within the coalbed, there is no horizontal hydraulic fracture at the base of the injection well and no-flow boundaries have been used at the edges of the model.

**Table XI:** Grid dimensions for leakage model.

Unit	nx, dx	ny, dy	nz, dz
Coal	36, 30 m	33, 30 m	5, 4 m
Unit directly above coal (unit 1)	36, 30 m	33, 30 m	4, 1 m
Top unit (unit 2)	36, 30 m	33, 30 m	3, 4 m

We found that for all our leakage scenarios the gas migrated into the overlying units, rather than being trapped within the coal (Figure 38). For scenarios 1 and 2, almost all of the CO<sub>2</sub> migrated straight into the overlying sands and went to the top of the sand body (Figures 38a and b). For the lower sand permeability scenario (2), migration was slower through the sand units, so lower sand layers have higher gas saturations than in scenario 1

<sup>2</sup> We have used sand and shale porosity and permeability values from Applied Hydrology Associates and Greystone Environmental Consultants (2002). The sands contained in the Wasatch and Fort Union formations are fine to medium grained (Flores, 2004; Applied Hydrology Associates and Greystone Environmental Consultants, 2002).

(Figure 38b). For scenarios 3 and 4, the shale acts as a confining unit and gas is able to migrate further away from the injection well within the coal than in scenarios 1 and 2 (Figures 38c and d). However, even after one year of CO<sub>2</sub> injection gas has migrated into the confining unit and up into the top layer of the sand unit (~30-40% gas saturation in the shale unit and top layer of the sand unit directly above the injection well) (Figures 38c and d). After 18 years of CO<sub>2</sub> injection the top layer of the sand in both scenarios has gas saturations of 70-90%. In scenario 5 we have reduced the vertical permeability in both the sand and shale units to values given by Applied Hydrology Associates and Greystone Environmental Consultants for vertical conductivities (2002) (they calculated vertical hydraulic conductivities for sands in the Wasatch Formation and we have converted those values to permeability in mD). The lower vertical permeability in both units means that gas migration into the shale and sand is more limited than in the other scenarios, so that after one year of CO<sub>2</sub> injection the shale has gas saturations of only ~20% immediately above the injection well and no gas has migrated into the overlying sand (Figure 38e). After 18 years of injection a small volume of gas has managed to migrate into the overlying sand and the top layer of the sand unit has gas saturations of ~10% immediately above the injection well.

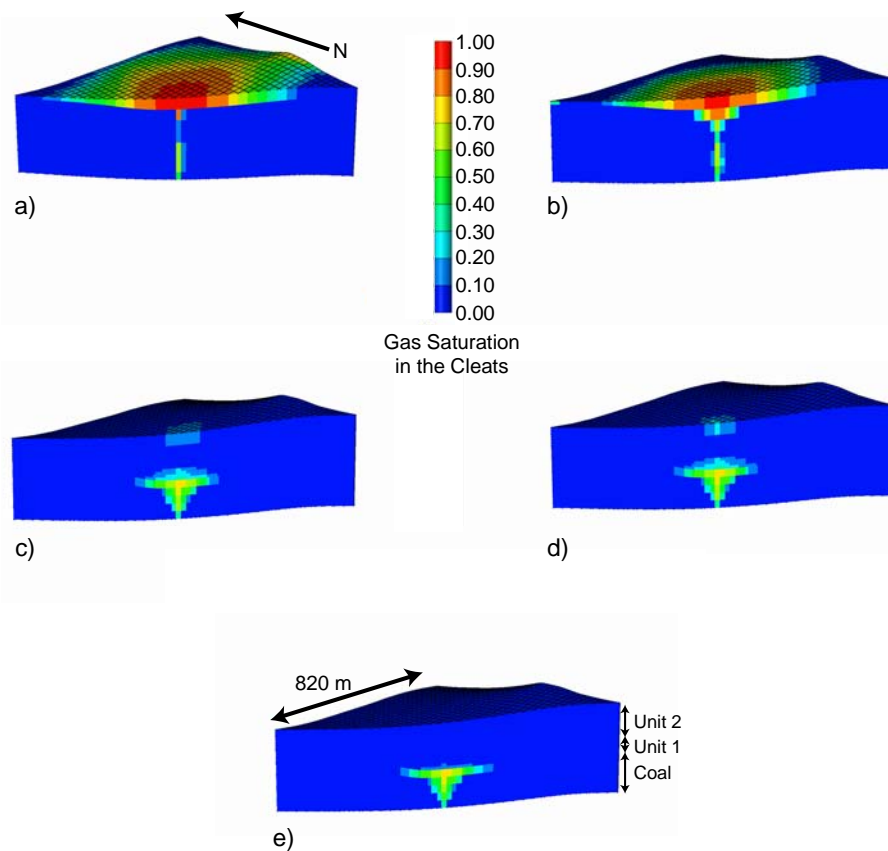


**Figure 38:** Gas saturation in the coal cleats after 1 year of CO<sub>2</sub> injection. a) Scenario 1 in Table X. b) Scenario 2 in Table X. c) Scenario 3 in Table X. d) Scenario 4 in Table X. e) Scenario 5 in Table X.

A much finer simulation grid would reveal a clearer picture of gas migration through the coal and into the shale and/or sand. However, our coarse simulations do show that it is imperative that coalbeds are overlain by cap rocks with permeabilities lower than  $\sim 0.002$  mD in the vertical direction, or gas migration into overlying sands will occur (gas diffusion and adsorption in coal occurs at a much slower rate than gas flow through the cleats and therefore most of the gas is able to migrate into overlying units, rather than being adsorbed, if there is no cap rock to stop migration and keep the gas within the coal).

### *Conclusions*

To determine the feasibility of sequestering CO<sub>2</sub> in unmineable coalbeds of the PRB we have carried out a reservoir characterization study and fluid flow simulations. We used geophysical and geological data from the PRB to develop a 3D model of the Big George coal, and used geostatistical techniques to populate our model with numerous coal cleat and matrix permeability and porosity realizations. Results from fluid flow simulations show that gravity and buoyancy drive gas migration, and matrix swelling reduces gas injectivity. However, placing a horizontal hydraulic fracture at the base of the injection well helps to overcome the negative effect of matrix swelling on injection rates. Our simulations suggest that after 13 years of injection we can sequester  $\sim 99\%$  of the total CO<sub>2</sub> injected into the Big George coal, that CH<sub>4</sub> production will be  $\sim 6$  times greater with CO<sub>2</sub> injection than without, and that one injection well will be able to sequester  $\sim 9$  kt of CO<sub>2</sub> a year. Based on this injection rate, it would take  $\sim 7,000$  injection wells (each with a lifetime of  $\sim 13$  years) to sequester the current CO<sub>2</sub> emissions for the State of Wyoming. In addition, our simulation results suggest that the CO<sub>2</sub> sequestration potential of the PRB (for coal at depths greater than 300 m) is  $\sim 1.35$  billion tonnes and at the current CO<sub>2</sub> emissions rate for the State of Wyoming the coal resources of the PRB can sequester Wyoming's annual CO<sub>2</sub> emissions for the next 20 years.

Finally, in regards to CO<sub>2</sub> sequestration feasibility and screening studies in coal-bearing basins around the world, it is important that the heterogeneous nature of the coal is captured in the simulation models, that models contain more than one layer in the vertical direction to account for gas buoyancy when water is present, and that potential coalbed sequestration sites are overlain by low permeability cap rocks. If the simulation models do not contain multiple layers in the vertical direction and heterogeneous permeability and porosity fields the CO<sub>2</sub> sequestration potential of coal-bearing basins will be over-estimated. In addition, the absence of a cap rock will lead to CO<sub>2</sub> migration into overlying formations and eventual leakage to the surface.

#### 4. Dynamic Imaging for Seismic Monitoring of CO<sub>2</sub> Storage in Coal

Flow simulation is used to predict the flow and storage of CO<sub>2</sub> in coalbeds. However, the behavior of injected CO<sub>2</sub> is not fully predictable because sites are never fully described, and in situ processes are not fully understood. Therefore, we will need to monitor the storage during and after the injection. When compared with other geological settings, e.g. depleted oil and gas reservoirs and deep saline aquifers, coalbeds present special challenges and features to exploit in monitoring. Figure 39 captures the monitoring workflow and shows the research activities on monitoring. It also shows the relationship between the monitoring activities. CO<sub>2</sub> flow simulation, the DARS laboratory measurements. The monitoring research is a simulation study involving the creation of proper time-lapse seismic models from flow simulations and two paths of image simulation: (A) Simulations that capture as best we know the physics of wave propagation in visco-elastic media and the subsequent space-time imaging/inversion process; (B) Simulations that yield idealized seismic images (perhaps 100's) extremely fast for testing acquisition configurations and temporal integration.

The goal of this approach is to develop a seismic imaging method that recursively constructs time-lapse subsurface images of CO<sub>2</sub> from continuously recorded data. We call this “dynamic subsurface monitoring” because it must exploit the temporal integration of measurements, knowledge of the changes in coals due to injected CO<sub>2</sub>, and model predictions from flow simulations or other sources. This dynamic imaging concept builds from the high-resolution baseline survey that is recorded for purposes of site selection and site characterization. To this baseline dataset, we propose to add small increments of data and perform lower-resolution reconnaissance imaging on a quasi-continuous basis. Should a reconnaissance image indicate a problem with CO<sub>2</sub> containment, acquisition resources are deployed to implement a high-resolution survey targeted on the problem area. Due to the relatively shallow nature of coalbeds, we exploit integrated source-detector geometries that might be considered impractical for deeper petroleum reservoirs or deep aquifers. This research is divided into two closely related tasks: (1) dynamic time-lapse imaging from sparse datasets; and (2) feature-enhanced model parameterization.

A diagram for the data flow of dynamic imaging is shown in Figure 40. This approach applies traditional tomography as follows: (1) Data are recorded with source-detector geometries (embedded for repeatability) from sources and detectors at the surface and in shallow slim boreholes. This geometry allows any combination of surface-to-surface profiles, quasi-vertical profiles, and quasi-crosswell profiles; (2) smart parameterization wherein a spatially variable mesh is used in the inversion to parameterize model updates, i.e., fewer unknowns in sections not expected to change and more unknowns in areas where changes are anticipated. The variable mesh is derived from flow predictions and temporal model history; (3) model evolution is used to assist development of the spatial mesh in order to reduce the number of spatial parameters in the update model; (4) data evolution is used to reduce the number of new samples needed in the time-lapse data volume. Data evolution complements the sparse data recordings by filling out the data array with estimates predicted from data history. A simplistic

approach to data evolution is to replace old data by zipping new data into the previous dataset. A better approach is to use a Kalman filter or other processing algorithm to predict data. Each component of this model plays an important role in the development of quality images from sparse datasets. The generic term tomography is used here to describe the process of imaging, and can be implemented from any source-detector geometry for transmitted, reflected, or diffracted wave events or any combination of these events.

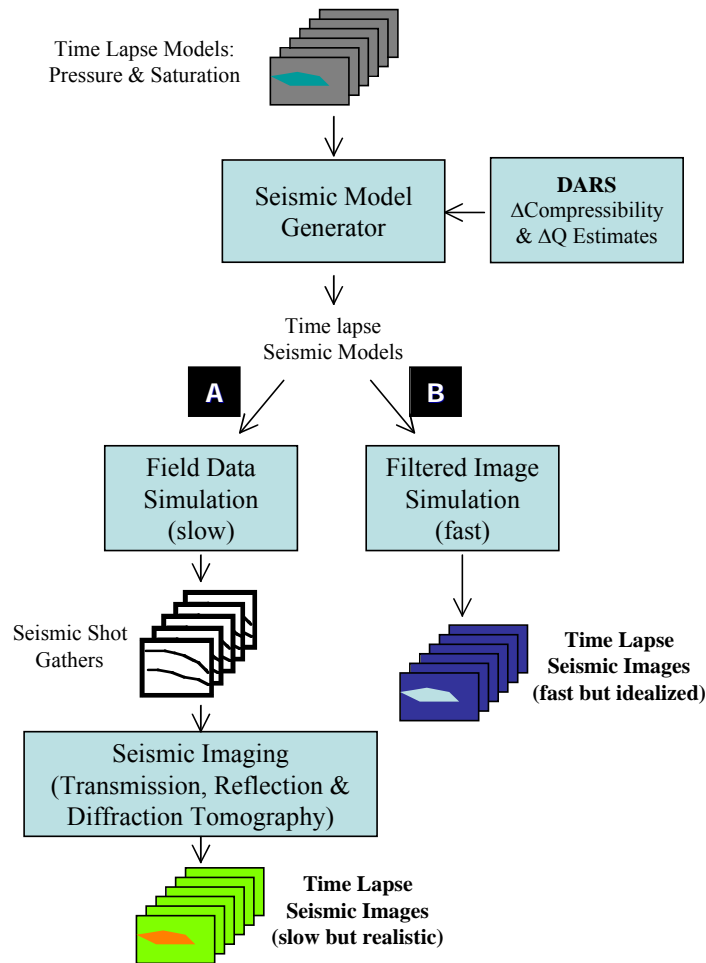


**Figure 39:** Workflow for the CO<sub>2</sub> monitoring studies. Flow simulation provides a series of pressure and saturation models corresponding to different times during CO<sub>2</sub> injection. The pressure and saturation changes are then converted into seismic property models with help from laboratory measurements of rock properties. Two paths are implemented for simulating the seismic images; (A) the expensive and slow process of simulating data acquisition and imaging; (B) an inexpensive and fast process of generating idealized seismic image.

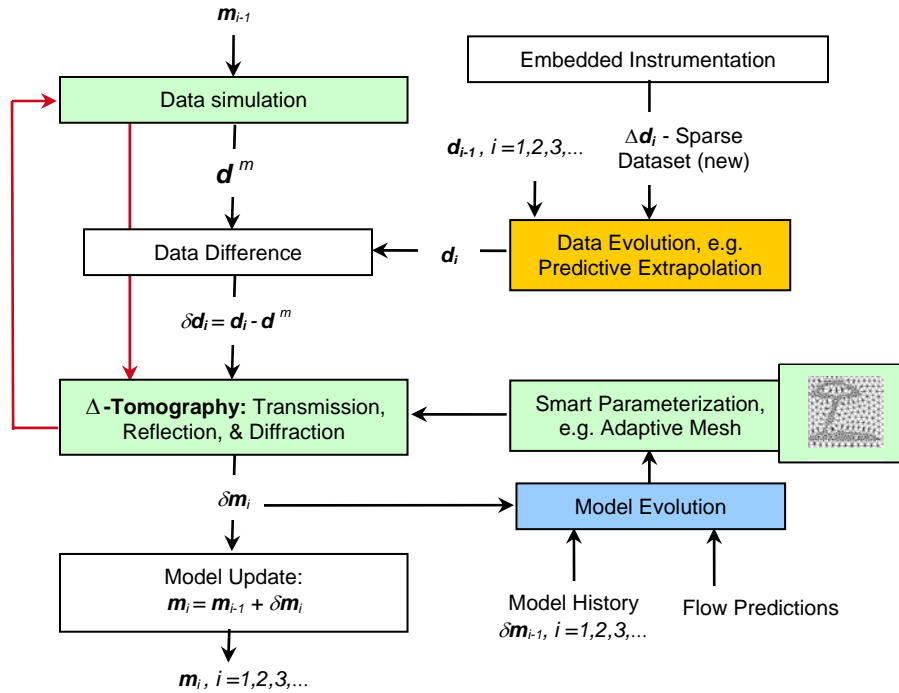


**Figure 40:** The data processing flow for dynamic subsurface monitoring combines elements of feature-enhanced parameterization and imaging from sparse datasets.

### Review of Field Seismic Studies for Coal

A literature review on coal seismic field studies is helpful for us to develop new seismic monitoring methods for coalbeds. Seismic methods have been extensively used for coal mine characterization and fault evaluation [40, 42, 43, 44, 45, 46, 47, 49], though not as much as in the oil and gas industry. Those coal surveys included 3-D high resolution seismic, vertical seismic profiling (VSP), crosswell seismic profiling, and sonic logging. Coals have low densities and low seismic wave velocities, typically *in situ*  $P$ -wave velocities in a range of 2–3 km/s. Coalbeds usually have large contrast against surrounding rocks, and as a result strong guided waves may exist in a coal layer. Figure 41 shows a typical  $P$ -wave velocity profile adapted from [47], which will be used for some modeling later in this report. Coalbeds of interest tend to be relatively shallow, with depths less than about 1000 m. Coals typically have high attenuation (or low  $Q$ -values); the *in situ* measurement of  $Q$ -value given in [42] is about 45. Coalbeds may have strong anisotropy [42] due to aligned fractures and micro layering. Lab measurements on coal samples show as much as 40%  $P$ -wave anisotropy [41].

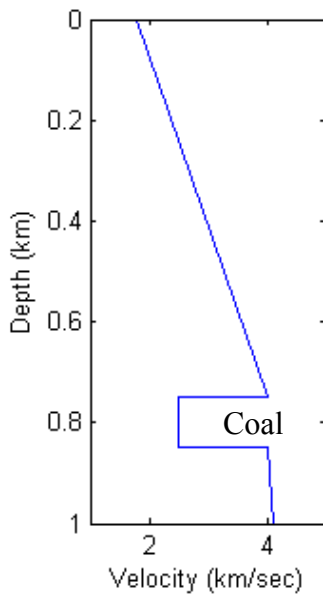


**Figure 41:** A *P*-wave velocity profile adapted from [47] from a coal mine.

### *Configurations for Seismic Monitoring*

We are proposing a special configuration of seismic sources and detectors system suitable for monitoring of CO<sub>2</sub> storage in coal, or other shallow subsurface monitoring projects. Figure 42 shows a diagram of this 3-D configuration implemented with embedded instrumentation. Circular array(s) on the surface acquires surface reflection data. Vertical arrays are located in near surface boreholes. Optionally, a deep array is embedded near the storage zone in the injection borehole. If we assume the target to be at a depth  $d$  which is relatively shallow, the vertical array is 20% or less of  $d$  (~200 m). We use the 20% vertical array to demonstrate that the slim instrumentation boreholes should be affordable. The optimum length of the vertical array has yet to be determined. If the length is too long, they will cost too much and also could penetrate the storage area possibly creating risks to CO<sub>2</sub> leaks. If the array length is too short, the aperture would be too small to improve imaging of the target. The applications of vertical arrays for seismic data acquisition can be found in [50, 51, 52].

This configuration can record reflection and refraction data from several different source-detector configurations. We show in Figure 42 only one circular array along with six vertical arrays near the surface. In fact, we can adaptively expand the diameter of the circular array or place as many additional vertical arrays as needed to improve coverage the volume. Using the velocity model shown in Figure 41, we have calculated the ray paths for different survey geometries and will discuss these below. In the case of enhanced coal bed methane (ECBM), CO<sub>2</sub> replaces CH<sub>4</sub>. In this multi-component case, the injected CO<sub>2</sub> may not cause detectable velocity changes but may have detectable attenuation changes. In this situation, passive seismic monitoring may be an effective method because it detects induced seismicity associated with pressure and fluid flow

front. The proposed acquisition configuration provides good coverage for passive microseismic observations as well as active seismic imaging, though passive seismic monitoring is not part of this project.

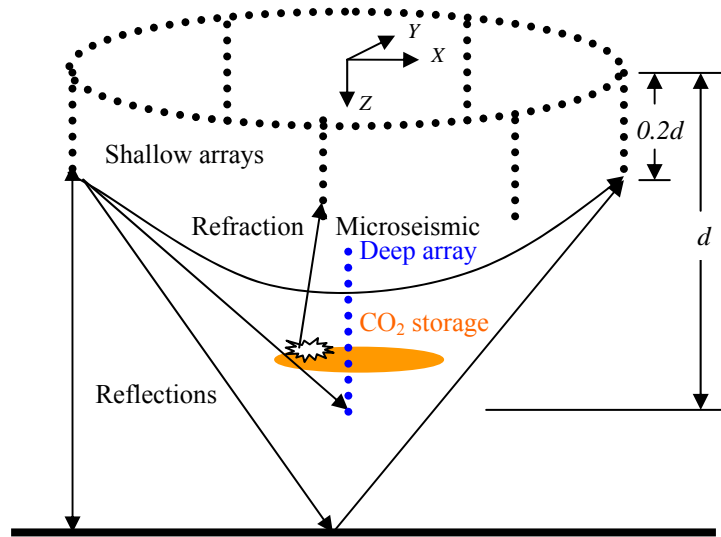


**Figure 42:** Source-detector configuration for seismic monitoring of shallow coalbeds.

Figure 43 illustrates ray paths of transmitted-refracted waves recorded with the vertical arrays. The near surface velocity gradient makes it possible to detect velocity changes below the transducers. Moreover, the length of the vertical array provides an aperture to improve imaging of the volume below. The penetration depth of the refraction wave depends on the velocity gradient and the horizontal separation of the vertical arrays. Although these waves may not penetrate the storage region of the coalbed, they will provide seismic surveillance above the coal and in the near subsurface for any upwelling  $\text{CO}_2$  in the event of a leak. Although the circular array records traditional surface reflection data, these near surface vertical arrays can also record reflections as displayed in Figure 43a. The reflections come from above and below the coal boundaries. In comparison with transmitted-refraction tomography in Fig 43a, reflections of the type shown in Fig. 43b have higher vertical resolution. Using both refraction and reflection data improves resolution and coverage of the subsurface.

The third option is to place a deep detector array behind casing of the injection well to further improve image resolution and coverage without significantly increasing cost. This configuration is a vertical seismic profile or VSP, for which typical reflection raypaths are shown in Figure 43c. Strong transmitted waves (not shown) from sources in the vertical arrays are also useful for velocity estimation and amplitude calibration.

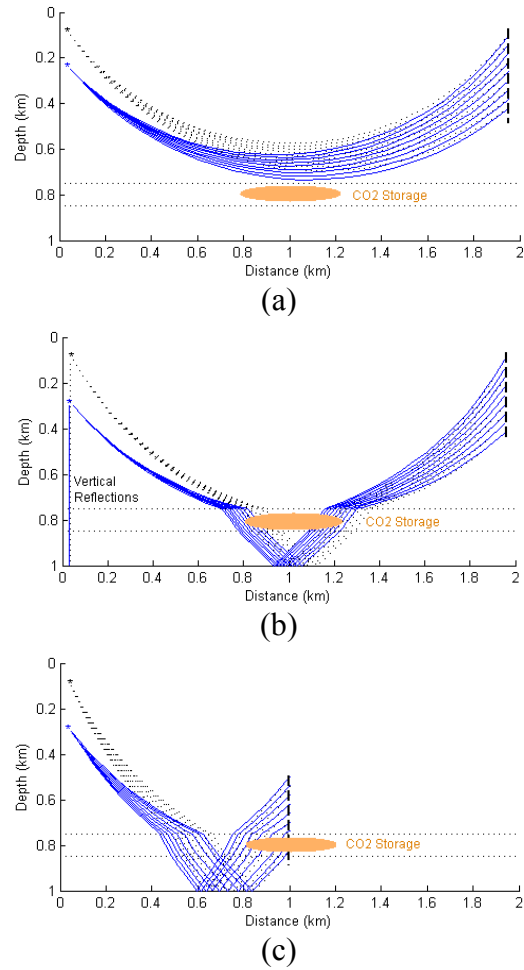


**Figure 43:** Typical raypaths recorded from vertical arrays: (a) Transmitted-refraction waves; (b) Reflected-refraction waves; (c) VSP reflected-refracted waves.

The types of images we can construct with these configurations of source and detectors are summarized in Table 4.1. As mentioned above, the design of this configuration is directed towards the relatively shallow subsurface targets of coalbed storage. In the case of deep targets, the length of the embedded vertical arrays and the diameter of the circular array would not be large enough to provide adequate imaging apertures.

**Table XII:** Possible image reconstructions with data from the various arrays.

	Transmission Tomography	Reflection Tomography	Diffraction Imaging
Circular surface array(s)		X	X
Shallow vertical arrays	X	X	X
Deep borehole array	X	X	X

### *Diffraction Tomography Filters for Studying Acquisition Geometries*

In order to test the various strategies for quasi-continuous monitoring, we require a modeling technique that is capable of modeling hundreds of time—sequential models, produced say from a flow simulator. The three “rigorous” steps of a modeling procedure are: (1) generate a synthetic seismic dataset by simulating every source and detector location for each time-lapse model; (2) processing each dataset to separate the wavefield event to be used in imaging; (3) invert each dataset for the time-lapse image. This procedure, as outlined above, is much too slow and expensive to perform on the numerous models that come from the flow simulator. Moreover, we may need to repeat the steps many times for the same model as we test various acquisition geometries. In this subsection, we describe a fast method of simulating the ideal seismic image resulting from a specific data acquisition geometry for a given geo-flow model. This fast image simulation method (path B in Figure 39) applies multi-dimensional spatial filters to the geo-flow model to generate the image. The results of this study helps to understand the seismic imaging with a hybrid combination of surface and vertical arrays. Studying these acquisition geometries described above for advantages and disadvantages under various conditions of CO<sub>2</sub> storage. This spatial filter approach comes from diffraction tomography [67, 58]:

$$O(x, z) = \frac{1}{(2\pi)^2} \iint \tilde{O}(K_x, K_z) \exp[i(K_x x + K_z z)] dK_x dK_z,$$

where  $\tilde{O}(K_x, K_z)$  is the filtered spatial Fourier transform of the model,  $\mathbf{K} = (K_x, K_z)$  is the spatial frequency vector constructed from the source-detector geometry, and  $O(x, z)$  is the reconstruction of the model as viewed through this seismic filter. Different acquisition geometries and signal properties yield different filters of the earth model. Figure 44a shows the “full aperture” spectral coverage for surface reflection profiles (SRP), crosswell seismic profiles (XSP) and vertical seismic profiles (VSP) acquisition geometries at the same frequency. It can be seen that the range of spatial frequencies covered is incomplete with either geometry, which means the inverted model will not yield a perfectly reconstructed image. Because more than one frequency is used in field experiments and the acquisition apertures are less than 180°, it is noteworthy to show the more realistic limited aperture multi-frequency filters (Figure 44b).

To illustrate the utility of this approach we manually created 221 time-lapse models. (We are working on the creation of these kinds of leaky models using a coal flow simulator). The first one (M<sub>0</sub>) is the baseline model. CO<sub>2</sub> is injected near the bottom right side. We assume that CO<sub>2</sub> saturation reduces the velocity. The filters used are shown in Figure 45. The frequency ranges for the three geometries are different: 1-50 Hz, 700-1000 Hz, and 1-150 Hz for SRP, XSP, and VSP, respectively.

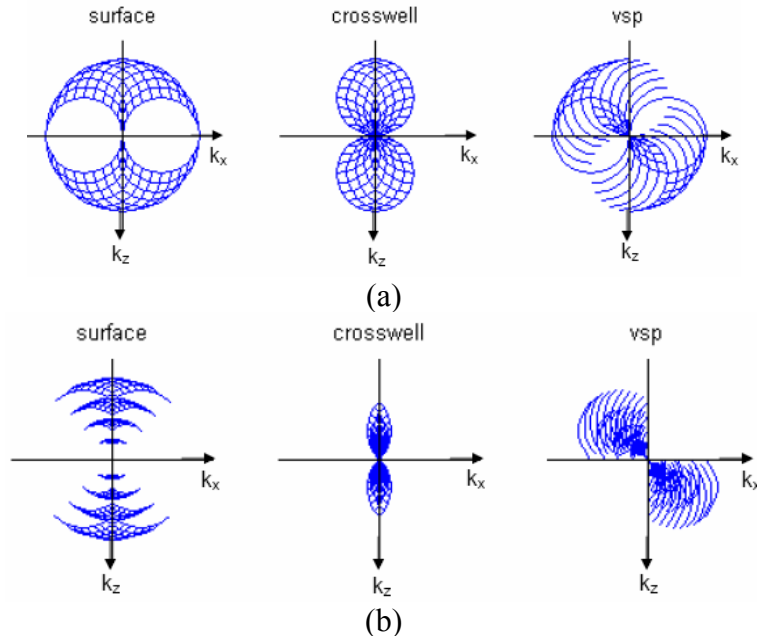


**Figure 44:** The single-frequency spatial filters obtained for 3 geometries from (a) full 180° apertures; (b) more realistic “limited apertures” with 90° maximum angular range.

The models are shown along the top row of Figure 46 and the SRP images for these models in the second row. The “true” model differences are presented in the third row of Figure 46 and the difference images for the SRP geometry in the fourth row. Finally, we show the XSP and VSP images in the lower two rows. Starting from Model 120 ( $M_{120}$ ), an upward leak can be seen to develop and create a thin vertical feature. The seismic images fail to capture this leak because of poor coverage in the lateral direction for the SRP and XSP geometries as can be seen from the absence of  $K_x$  samples in the filters shown in Figure 45. The VSP geometry has better  $K_x$  coverage and its reconstructed image resolves this small vertical feature best. This idealized image simulation approach shows how different acquisition geometries sample the Fourier components of the model. It can produce ideally-reconstructed images in minutes for hundreds of time-lapse models, in contrast to path A in figure 39 that would take months to simulate.

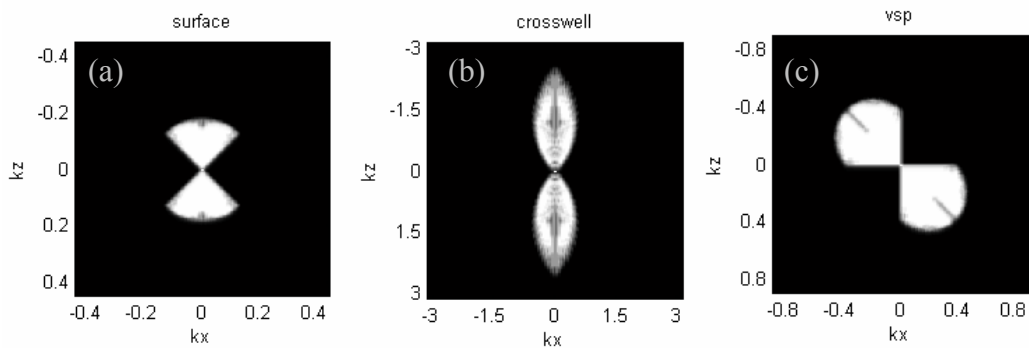


**Figure 45:** Spatial frequency filters used in the filtered image models (Fig 46).

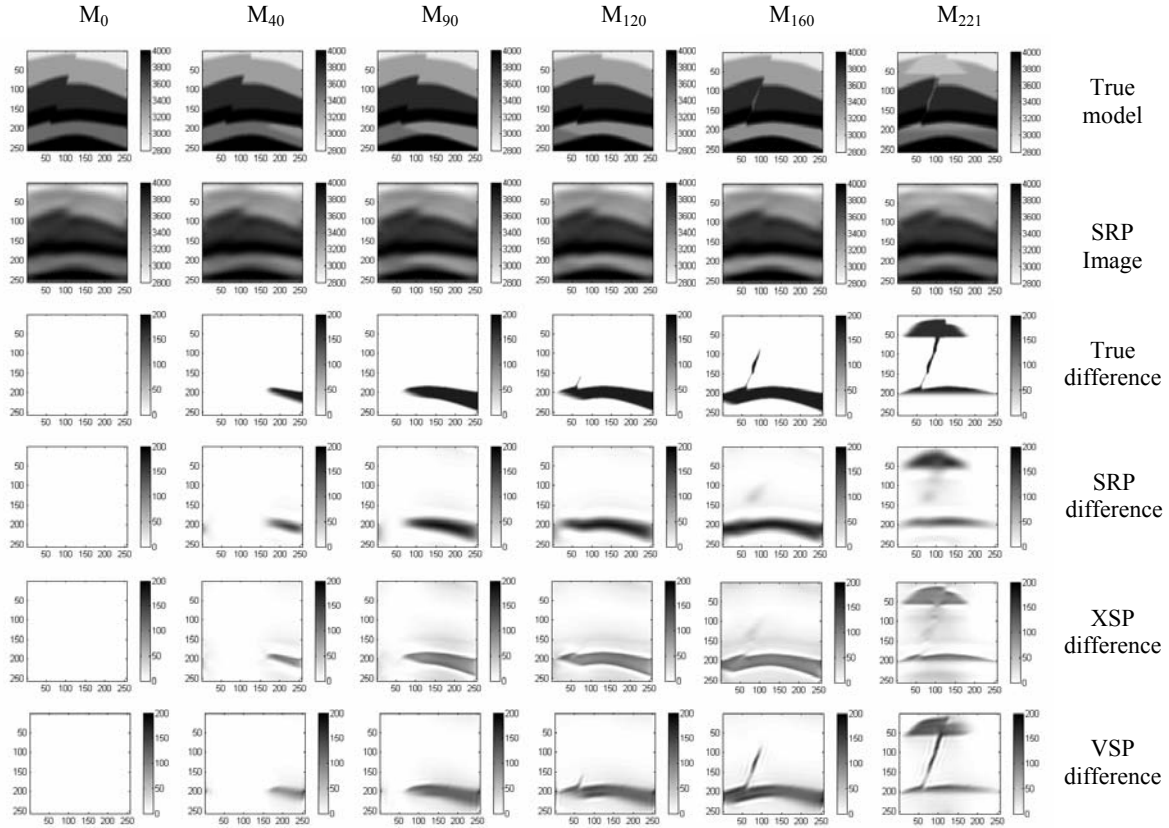


**Figure 46:** Filtered diffraction tomography for surface seismic reflection profiles (SRP), crosswell seismic profiles (XSP) and vertical seismic profiles (VSP).

We will use this fast simulation tool to address fundamental questions on optimal acquisition geometries, advantages and disadvantages of combined arrays, and test of the temporal integral loop.

### *Imaging with Feature-enhanced Adaptive Meshes and Temporal Regularization*

The expected subsurface changes are expected to occur in localized regions due to CO<sub>2</sub> and pressure. The geology changes little if any. Conventional imaging approaches often estimate many more parameters than needed because these main structural features do not change. This results in image artifacts from computing differences between surveys due to different successive estimations of these static geological structures [63]. In order to minimize such undesirable effects, we propose a temporal integration technique combined with a reduction in the number of model parameters to be estimated. Temporal integration is accomplished through joint inversion of incremental new data with data from previous surveys. New data are more strongly related with current subsurface models and therefore should have heavier weights in this joint inversion.

Reduction in the number of parameters is achieved by feature-enhanced adaptive meshing. One of the advantages of the adaptive triangular mesh [53] is the resolution achieved through use of a finer mesh near the front of the injected CO<sub>2</sub> plume. Another advantage is the implicit spatial regularization that occurs due to the use of coarser meshes in slow-varying regions. Thus, we use adaptive triangular adaptive meshes, temporal integration and spatial regularization [66] for the time-lapse imaging. Moreover, the triangular mesh is used to reduce the number of model parameters. However, we also want to keep the simple formulation of the tomographic matrix and regularization for conventional regular grids. Thus, we derived a different formulation for the use of triangular meshes that allows mapping between triangle vertexes and a regular grid. This approach can be used as a general framework to solve linear inverse problems for different areas using triangles instead of cells as basic elements, with minimal impact to original problem formulation. The key concept is to describe each cell of a regular grid as a linear combination of control nodes values at triangle vertexes, considering the respective triangle that covers each region of regular grid. Thus, a linear operator  $T$  may be explicitly defined to map any regular grid into control nodes of a triangular mesh. This approach also keeps the possibility of using its inverse mapping  $T^{-1}$  to find a regular (or rectangular) grid representation from a triangular representation, which is useful to display the resulting image of tomographic inversion.

The algorithm that computes matrix  $T$  has the following steps for each triangle of mesh: (1) Identify its three vertexes to compute vertex weights based on relative position of interior cells of the triangle; (2) compute weights for each cell of regular grid within current triangle using barycentric coordinates interpolation; (3) store these weights into a matrix  $T$  that maps each cell value as a linear combination of control nodes triangle vertexes. The interpolation using barycentric coordinates is based on the areas of three imaginary triangles formed by lines between triangle vertexes and an interior point [55]. These three areas are used as a measurement of influence of each control node vertex onto a point belonging to a triangular mesh element, resulting in three respective weights for each interior point. Considering  $v_1$ ,  $v_2$  and  $v_3$  as the control values at respective positions  $\mathbf{r}_1$ ,  $\mathbf{r}_2$  and  $\mathbf{r}_3$  corresponding to vertexes of each triangle, the weights for each interior point at position  $\mathbf{r}$  are given by the following expressions:

$$w_1(\mathbf{r}) = \frac{(\mathbf{r} - \mathbf{r}_2) \times (\mathbf{r}_3 - \mathbf{r}_2) \cdot \mathbf{e}_3}{(\mathbf{r}_1 - \mathbf{r}_2) \times (\mathbf{r}_3 - \mathbf{r}_2) \cdot \mathbf{e}_3},$$

$$w_2(\mathbf{r}) = \frac{(\mathbf{r} - \mathbf{r}_1) \times (\mathbf{r}_3 - \mathbf{r}_1) \cdot \mathbf{e}_3}{(\mathbf{r}_2 - \mathbf{r}_1) \times (\mathbf{r}_3 - \mathbf{r}_1) \cdot \mathbf{e}_3},$$

$$w_3(\mathbf{r}) = \frac{(\mathbf{r} - \mathbf{r}_1) \times (\mathbf{r}_2 - \mathbf{r}_1) \cdot \mathbf{e}_3}{(\mathbf{r}_3 - \mathbf{r}_1) \times (\mathbf{r}_2 - \mathbf{r}_1) \cdot \mathbf{e}_3},$$

where  $\mathbf{e}_3$  is the unitary vector (0,0,1). This leads to the following expression that maps nodes control values from triangular mesh into a regular grid cell value  $o(\mathbf{r})$  for each triangle:

$$o(\mathbf{r}) = \sum_{i=1}^3 w_i(\mathbf{r})v_i(\mathbf{r}).$$

The matrix  $T$  performs this mapping for each cell of regular grid using respective triangles that covers its different regions. Thus, nodes control values at triangle vertexes are mapped into a regular grid using the forward mapping expression  $\mathbf{o} = T\mathbf{v}$  and the inverse mapping from regular grid into control nodes values of triangular mesh is given by  $\mathbf{v} = T^{-1}\mathbf{o}$ . This allows a straightforward modification to convert a regular grid method into a triangular mesh method. From a simple regular grid formulation for linear problems  $\mathbf{p} = W\mathbf{o}$ , where  $\mathbf{p}$  is the data vector and  $\mathbf{o}$  is the model parameter vector, one may use the expression for triangular meshes  $\mathbf{p} = WT\mathbf{v}$ . For linear inverse problems, this expression may be applied to estimate triangular mesh control node values from data vector

$$\mathbf{v} = (WT)^+ \mathbf{p},$$

where the superscripted plus symbol means pseudo-inverse [61] computed using SVD. An equivalent regularized system may also be obtained from

$$\begin{bmatrix} W \\ \lambda D \end{bmatrix} T\mathbf{v} = \begin{bmatrix} \mathbf{p} \\ \mathbf{0} \end{bmatrix},$$

where  $D$  is a numerical derivative matrix and  $\lambda$  is a constant [65]. After parameter estimation, the resulting triangular mesh control values can be easily displayed as a regular grid using forward mapping of linear operator  $T$ , as described earlier.

The second component this scheme is time regularization. Time-lapse imaging conventionally inverses different data sets independently and then analyzes image subtraction to identify changes. This straightforward approach repetitively estimates fixed geology structures as well model changes due to pressure and saturation, ignoring the similarities between successive images that could be useful during inversion. A smarter approach uses a temporal derivative operator to integrate data along time using previous information combined with repeated surveys [54]. It requires solving an integrated linear system that contains previous survey equations and temporal derivative equations minimization. We adopted a different approach that integrates previous surveys information but uses a scalar factor to damp the influence of each previous survey into the latest survey information available by forming an augmented system

$$\begin{bmatrix} W_k \\ \alpha_{k-1}W_{k-1} \\ \vdots \\ \alpha_{k-ns+1}W_{k-ns+1} \end{bmatrix} \mathbf{o} = \begin{bmatrix} \mathbf{p}_k \\ \alpha_{k-1}\mathbf{p}_{k-1} \\ \vdots \\ \alpha_{k-ns+1}\mathbf{p}_{k-ns+1} \end{bmatrix},$$

where index  $k$  represents the newest survey,  $ns$  is the number of available surveys and  $\alpha_{k-i}$  is a normalized scalar proportional to the influence of earlier survey  $k-i$  into current inversion, being smaller for older surveys. Since relevant information from previous surveys is included in this equivalent system, a new smaller and less expensive survey

may be performed to update subsurface image. This procedure can be repeated for newer datasets and keeps relevant information from previous ones, increasing the number of rows by the number of newer survey equations but keeping fixed the number of columns of equivalent linear system, which may not occur when using temporal derivative operator approaches.

The imaging method with triangular mesh and temporal integration discussed above can be used for relatively general linear geophysical inversion. We now apply it to seismic diffraction tomography [67, 58], where the incident field from a source at  $\mathbf{r}_s$  can be represented through the Green's function  $G(\mathbf{r}_s | \mathbf{r}')$  and the scattered field at receiver  $\mathbf{r}_g$  can be calculated by

$$P_s(\mathbf{r}_s, \mathbf{r}_g) = -k_0^2 \int O(\mathbf{r}') G(\mathbf{r}' | \mathbf{r}_s) G(\mathbf{r}_g | \mathbf{r}') d\mathbf{r}'$$

This formula is the space domain forward modeling equivalent to the diffraction tomography formula used above to create the fast filter image simulator. Discretization of the above equation leads to the linear system  $\mathbf{p} = \mathbf{W}\mathbf{o}$ , which has to be inverted in order to recover  $O(\mathbf{r})$  [64]. In this work the inversion was done using SVD, but could be done using other linear system solvers.

Next, we simulate a CO<sub>2</sub> monitoring experiment to test this time regularization algorithm. As discussed above, we have 221 time-lapse CO<sub>2</sub> flooding models. Five of these time-lapse models are presented in Figure 47 for the VSP geometry. The figures show only the velocity difference compared with the background medium (~4,000 m/s). There is a negative velocity contrast (2%) caused by CO<sub>2</sub> injection. Data are simulated for each model for 28 sources and 28 receivers. Triangular adaptive meshes (column b) are generated based on velocity gradient from *a priori* information, leading to the inversion results shown in column c. A regular grid would provide good results for this base survey as well, since a reasonable number of sources and receivers are employed. As discussed above, *a priori* information from reservoir flow simulation or from previous surveys may be used to generate adaptive meshes. The adaptive mesh inversion reduces the number of parameters but maintains robustness, since triangles at slow-varying velocity fields regions are coarser but still useful to perform good imaging even with low quality *a priori* information. Since the previous datasets is integrated into inversion, the successive updates use a fewer and consequently less expensive datasets. In our example, we use a constant scalar for the immediately previous survey  $\alpha = 0.3$  and adopt respectively  $\alpha^2$ ,  $\alpha^3$  and so on when other earlier surveys were available and evenly sampled along time. We apply spatial regularization for order 2 and  $\lambda = 0.02$  for all inversions. A naive regular grid inversion for such image resolution would require 50 sources and 50 receivers for each time-lapse inversion, which means that it would require three times more data measurements than we used here. This reduction in the number of parameters is reinforced by temporal integration of previous survey to achieve current subsurface image. Thus, problems that are originally underdetermined can be reformulated as overdetermined without the drastic decrease of resolution required for regular grids under similar circumstances.

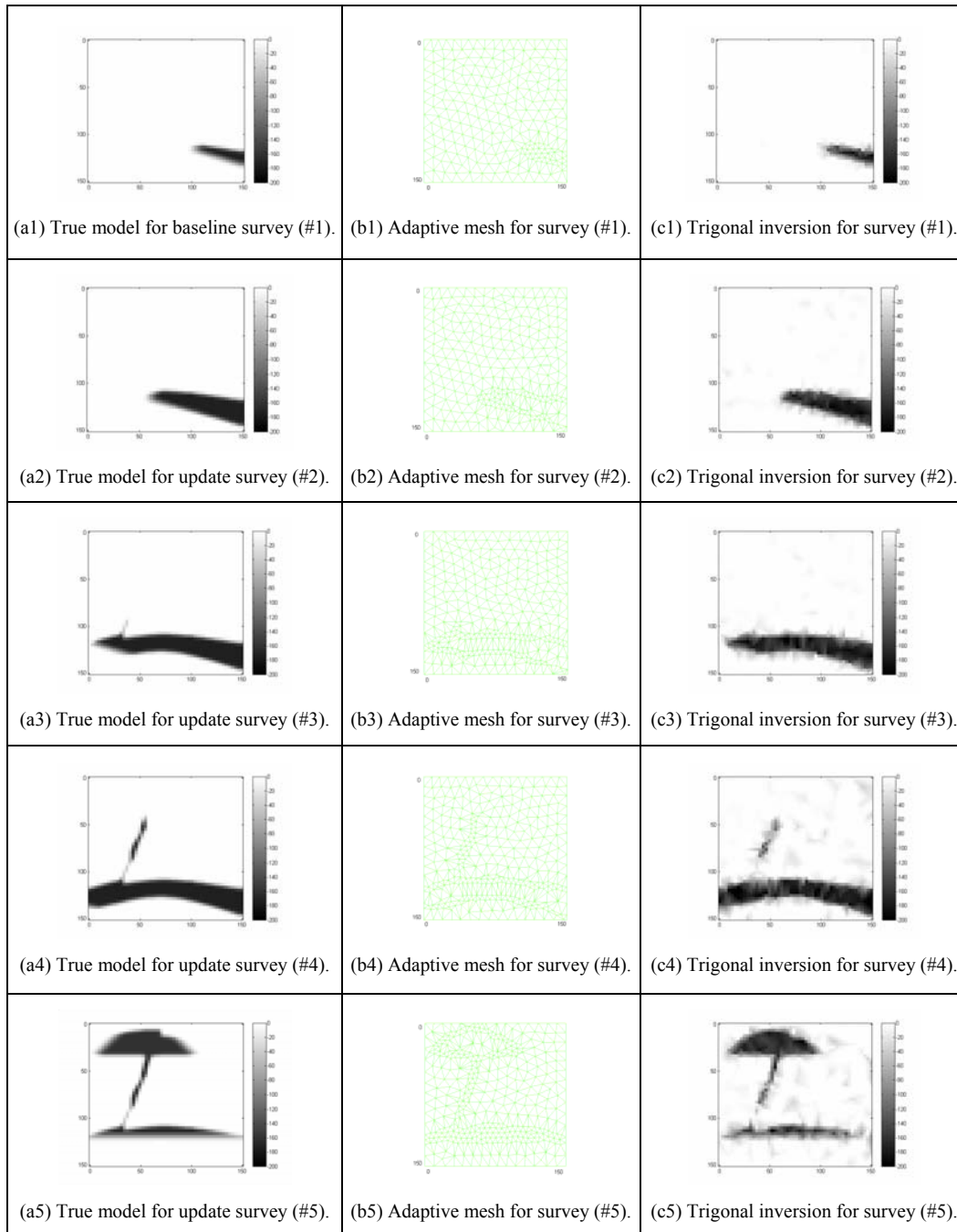


**Figure 47:** Monitoring test with adaptive triangular meshes. True models, adaptive meshes and reconstructions are shown in columns a, b and c, respectively. Distances are in meters and velocities in m/s.

### *Data Evolution and Model Evolution*

As outlined in Figure 39, we plan to use sparse datasets to update the baseline model on a quasi-continuous basis. One problem with this concept is that sparse datasets often lead to undesirable image artifacts because the inversion problem is underdetermined. To

address this problem, we first reduced the number of unknown parameters in the inverse model, e.g., the adaptive mesh from the previous section. In this section, we add the additional features of data and model evolution or prediction in order to further reduce the requirements on the underdetermined inversion algorithm. The data ( $\mathbf{d}$ ) here can be travel time, amplitude, the full seismic trace, or other seismic observables; seismic velocity, reflectivity or other subsurface parameters are the model ( $\mathbf{m}$ ) to be estimated. This estimation problem can be formally expressed as

$$\mathbf{d} = G\mathbf{m} ,$$

where  $G$  is an operator relating model and data. The length of the data vector  $\mathbf{d}$  equals to  $N$ , the number of source-receiver pairs, data points or groups of data points.  $N$  should be large enough so that a proper inversion can be done.

Data  $\mathbf{d}$  and model  $\mathbf{m}$  are time-varying because of the CO<sub>2</sub> injection process. Assume that a large and complete dataset  $\mathbf{d}_{i-1}$  is obtained corresponding to model  $\mathbf{m}_{i-1}$ , i.e., the baseline survey. We have

$$\mathbf{d}_{i-1} = [d_{i-1}^{(1)} d_{i-1}^{(2)} \dots d_{i-1}^{(N-1)} d_{i-1}^{(N)}]^T .$$

For a true 4-D monitoring, data acquisition must be continuous or quasi-continuous. As the model changes from  $\mathbf{m}_{i-1}$  to  $\mathbf{m}_i$ , only partial new dataset (say,  $P$  records,  $P \ll N$ )  $\Delta\mathbf{d}_i$  are collected:

$$\Delta\mathbf{d}_i = [d_i^{(1)} d_i^{(2)} \dots d_i^{(P)}]^T .$$

If we use  $\Delta\mathbf{d}_i$  to invert  $\mathbf{m}_i$  as an underdetermined inverse problem, the quality of the resulting image would be very poor because of incompleteness of the data. As illustrated in Figure 40, we may use one of several different methods to estimate or evolve a complete dataset. This estimation problem is formally described as a merging of the old dataset with the new incremental dataset:

$$\mathbf{d}_i = \mathbf{d}_{i-1} \oplus \Delta\mathbf{d}_i = [\hat{d}_i^{(1)} \hat{d}_i^{(2)} \dots \hat{d}_i^{(N-1)} \hat{d}_i^{(N)}]^T , \quad (33)$$

where  $\oplus$  is an operator representing the data evolution algorithms and  $\hat{d}_i^{(k)}$  is the data estimated with these evolution algorithms. The simplest approach to obtaining  $\mathbf{d}_i$  may be the replacement of data records 1,2, ...,  $P$  in  $\mathbf{d}_{i-1}$  by  $\Delta\mathbf{d}_i$ , that is

$$\mathbf{d}_i = \mathbf{d}_{i-1} \oplus \Delta\mathbf{d}_i = [d_i^{(1)} d_i^{(2)} \dots d_i^{(P)} \dots d_{i-1}^{(N-1)} d_{i-1}^{(N)}]^T .$$

Another method is to predict the missing data from data history giving

$$\mathbf{d}_i = \mathbf{d}_{i-1} \oplus \Delta \mathbf{d}_i = [d_i^{(1)} d_i^{(2)} \dots d_i^{(P)} \dots \hat{d}_i^{(N-1)} \hat{d}_i^{(N)}]^T,$$

where  $\hat{\mathbf{d}}_i = A_{i-1} \mathbf{d}_{i-1}$  describes a prediction process such as extrapolation and “^” means that the value is estimated. Here  $A_{i-1}$  is a prediction operator.

A more advanced approach is to predict  $\mathbf{d}_i$  from history data and then update the predicted data with current observed data  $\Delta \mathbf{d}_i$ , which is defined as

$$\hat{\mathbf{d}}_i = P(\Delta \mathbf{d}_i | \mathbf{d}_1, \dots, \mathbf{d}_{i-1}).$$

The Kalman filter [106] is a classical algorithm for this recursive prediction-update procedure. Let  $\hat{\mathbf{d}}_0$  be the initial dataset and  $\hat{C}_0 = \text{cov}(\hat{\mathbf{d}}_0)$  be the initial prediction error covariance. Then we can recursively evolve the temporal datasets with Kalman filter described by

$$\begin{aligned} \hat{\mathbf{d}}_{k+1} &= A_k \hat{\mathbf{d}}_k + K_k (\mathbf{d}_k - \hat{\mathbf{d}}_k) \\ \hat{C}_{k+1} &= (A_k - K_k) \hat{C}_k (A_k - K_k)^T + Q_k + K_k R_k K_k^T, \\ K_k &= A_k \hat{C}_k (\hat{C}_k + R_k)^{-1} \end{aligned} \quad (34)$$

where  $K_k$  is Kalman gain,  $Q_k$  is process noise covariance,  $R_k$  is measurement noise covariance, and  $\mathbf{d}_i$  is observed data that may be obtained through Equation (33) in our case. We have found some practical problems (e.g., large matrix dimensions and lack of reliable estimates for the covariance matrixes) for applying this standard Kalman filter shown in Equation 34. We need to develop an adequate form of the Kalman filter for our special purpose of temporal seismic data evolution.

Similar to data evolution, we may also apply the recursive prediction-update procedure to model evolution, so that we can incorporate history models and flow simulation results for the subsurface imaging. For the model evolution we define this estimation problem as

$$\mathbf{m}_i^* = P(\mathbf{m}_i | \mathbf{d}_1, \dots, \mathbf{d}_i),$$

and implement it by the Kalman filter. First, we use the flow simulation, history data  $(\mathbf{d}_1, \dots, \mathbf{d}_{i-1})$  and an initial model to predict the model recursively by

$$\begin{aligned} \hat{\mathbf{m}}_{k+1} &= F_k \mathbf{m}_k + K_k (\mathbf{d}_k - G_k \hat{\mathbf{m}}_k) \\ \hat{C}_{k+1} &= (F_k - K_k G_k) \hat{C}_k (F_k - K_k G_k)^T + Q_k + K_k R_k K_k^T, \\ K_k &= F_k \hat{C}_k G_k^T (G_k \hat{C}_k G_k^T + R_k)^{-1} \end{aligned} \quad (35)$$

where  $F_k$  is the model prediction operation defined by flow simulation. Second, we incorporate the predicted model  $\hat{\mathbf{m}}_i$  from Equation 35 to update the model using current observation  $\mathbf{d}_i$  :

$$\begin{aligned}\mathbf{m}_i^* &= \hat{\mathbf{m}}_i + K_i(\mathbf{d}_i - G_i\hat{\mathbf{m}}_i) \\ \hat{C}_i &= (1 - K_iG_i)\hat{C}_i \\ K_i &= \hat{C}_iG_i^T(G_i\hat{C}_iG_i^T + R_i)^{-1}\end{aligned}$$

Data  $\mathbf{d}_i$  can be either time evolved or directly acquired.

We performed a seismic monitoring simulation using the Kalman filter for model evolution, i.e., without data evolution. The result of the simulation was poor, but showed why additional information and/or constraints are required. Here, we briefly summarize the results of this Kalman filter test. In that simulation test, the crosswell geometry was used for demonstration purposes. The finite difference simulation method was used to calculate the full seismic wave field. Figure 48 shows the baseline model and a common source gather of the simulated data. We created a total of 221 time-lapse models and chose four of them for this monitoring test. A complete crosswell survey was run first; then four incremental partial time-lapse surveys were simulated (see Figure 49a). Figure 49b shows the true velocity differences between time-lapse models and the baseline model. Figure 49c gives the inversion results of the velocity differences. Because only partial surveys are used for the recursive dynamic estimation, the reconstructed images are poor, though we can roughly identify the area saturated with CO<sub>2</sub>. This test has shown that direct use of partial surveys would result in an underdetermined inversion. We must use the history data plus current partial data to evolve a full data set for the dynamic imaging.

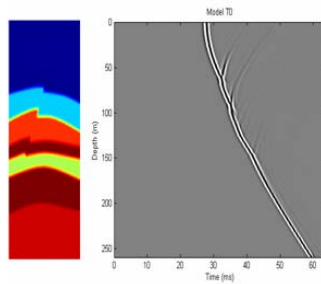


**Figure 48:** The geological model (left) and a common source gather of the simulated crosswell seismic data (right).

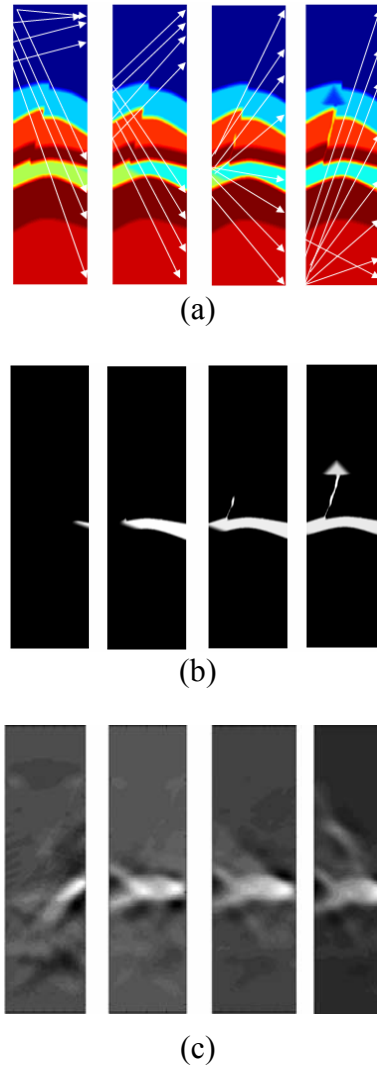


**Figure 49:** Kalman Filter tests. (a) Four partial surveys are collected as the model changes; (b) True model differences between time-lapse models and baseline model; (c) reconstructed velocity differences using Kalman filter for model evolution.

### *Monitoring Summary*

Our monitoring research has yielded results in three areas: (1) A data acquisition configuration that is unique for coal has been developed. This configuration incorporates circular surface arrays, shallow vertical arrays in one or more deep injection boreholes. (2) A fast image simulation procedure that allows us to quickly generate numerous idealized seismic images from time-lapse models. This procedure allows us to efficiently test data gathering and temporal integration strategies. (3) A unified inversion strategy for quasi-continuous monitoring using sparse incremental datasets. The strategy incorporates both data evolution and model evolution along with temporally adaptive and variable mesh that can be derived from flow predictions and model history. Our tests with Kalman filters yielded unexpectedly poor results, but we still believe Kalman filters will be useful when integrated with other methods, namely smart parameterization, and data evolution.

## 5. Observations of a Coalbed Fire

A coalbed fire refers to a phenomenon when subsurface coal ignites and combusts underground over a time period ranging from days to hundreds of years. The depths of these fires are variable; and they can be as deep as several hundred meters or as shallow as a few meters. Coalbed fires occur worldwide and can be found in countries such as China, India, Indonesia and the U.S. [91, 92].

Coalbed fires can have negative impacts on various levels. They can affect the economics of coal production, since the fire consumes coals that could otherwise be excavated. Health of those living near the coal fire is at risk from prolonged exposure to toxic gases such as carbon monoxide. Furthermore greenhouse gases such as CO<sub>2</sub> and CH<sub>4</sub> are released into the atmosphere when the coal is combusted. The amount of CO<sub>2</sub> released from coal fires in China is estimated to be as high as 360 million metric tons per year, a figure that is comparable to the CO<sub>2</sub> emissions from the entire US transportation sector [90].

Coalbed fires began receiving attention in recent years because of the large CO<sub>2</sub> emissions. Early research on these fires largely focused on tracking the fire through remote sensing methods with tools such as thermal cameras and satellites. These studies have characterized the migration of fires through time lapse images of the same area.

We seek to identify relationships among the most important variables that govern fluid flow and combustion by collecting field data and using them to build a representative numerical model. In particular, we want to understand the relationship between combustion front propagation velocity and the pressure gradient that drives flow of gas at the front. Ultimately, this relationship will be used to determine whether we can stop the propagation of the fire by injecting a fluid with the same pressure gradient in the opposing direction.

In order to build a physical model of coalbed fires, we are currently collecting data from a coalbed fire site in southwest Colorado. This fire was first discovered around 1998, and the same coalbed continues to burn a decade later. Coalbed fires can start in several ways, including lightning strikes, forest fires, spontaneous combustion of coal and negligence such as burning garbage near coal outcrops [89]. In the case of the Colorado fire, the source of ignition may have been forest fires started by lightning strikes. Burned tree roots that penetrated to the coal can be found at locations near where the coal is currently burning.

The surface expression of the underground fire is a set of fissures. These surface fissures, which connect the surface and the combusting coal, can be as long as 10m and as wide as 0.25m. These fissures act as O<sub>2</sub> influx points as well as vents for combustion gases. These surface fissures do not grow randomly—rather they form along stress fracture patterns found on the 0.3m thick sandstone which lies 0.2~0.25m below the surface. Figures 50a and 50b show two newly emerged surface fissures observed over the coal fire, and Figures 51a and 51b show the sandstone fracture that lies below respective surface fractures.



**Figure 50:** a) A newly formed surface fissure facing the NW 60 direction covered by topsoil and b) An older surface fissure facing the NE 30 direction.

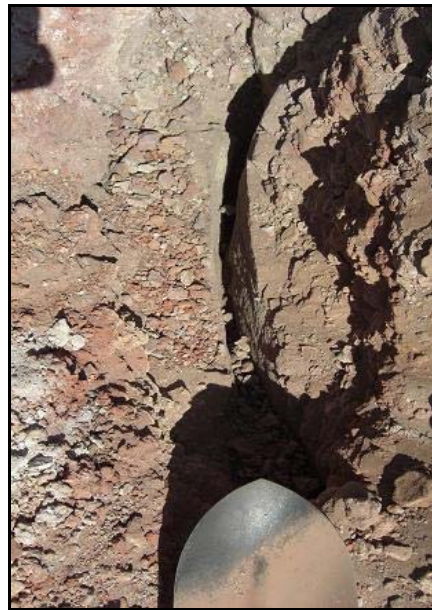


**Figure 51:** a) The NW 60 fissure excavated to the sandstone level, and b) The NE 30 fissure excavated to the sandstone level. Both fractures are about 2.5 cm inch wide.

These fractures are believed to have existed before the fire began. The idea of preexisting fractures is well supported by the systematic orientation of the fissures observed at the site. There are only two primary directions of fissure propagation, NE 30 and NW 60, the same directions as the limited number of sandstone fractures observed

directly. Perpendicular fracture sets are commonly observed in other geological formations. In addition, fractures in the same orientations were observed in the same sandstone formation layer far away from the fire, strengthening the notion that these fractures existed prior to the ignition of the coal layer.

We hypothesize that preexisting fractures in the sandstones provide a pathway for escape of combustion product gases generated nearby as the combustion zone propagates. There is apparently a sequence of events through which a fracture generates a surface fissure. Fissure growth at the surface can be broken down into roughly three steps. This sequence is shown in Figure 52. First, the ground where the future fissure is going to appear becomes damp, presumably due to the moisture that is driven off from both the coal and the topsoil and the water in the combustion gases. The topsoil during this initial stage of fissure growth becomes very wet and heavy. As temperature increases, the topsoil dries, and small vents form where the topsoil is the weakest above the sandstone fractures. Sulfur and ammonium chloride, which are evaporated and formed by high temperature gases underground, respectively, are deposited around these vents as the emitted gases cool. These vents eventually connect to form a surface fissure above the sandstone fracture. Figure 52 shows this in a sequence. The timescale of growth of these surface fissures has not been documented.



**Figure 52:** a) A line of moisture indicates where a fissure will develop in the near future, b) vents along the moisture line form, releasing combustion gases and precipitating ammonium chloride and c) the vents connect to form a surface fissure.

Both vents and fissures can be a source of significant amount of heat, as gas is convected out of these openings. Field recordings indicate that the temperatures can exceed  $1000^{\circ}\text{C}$  in the hottest regions. Temperature measurements were taken with an infrared temperature sensor over these fissures, and initial results show that fissures located at a higher surface elevation have higher temperatures. Also, the temperature gradients were observed along some of the fissures, an indication of the location of combustion front. In addition to the temperature measured with the infrared sensor,

thermal images of the area were also made. From the thermal images, it is possible to see that regions around the fissures are significantly hotter than are locations without fissures. High temperatures were recorded in some areas even where the topsoil had not yet opened up to form a fissure. Figures 60a and 60b show a fissure and its thermal image, respectively.

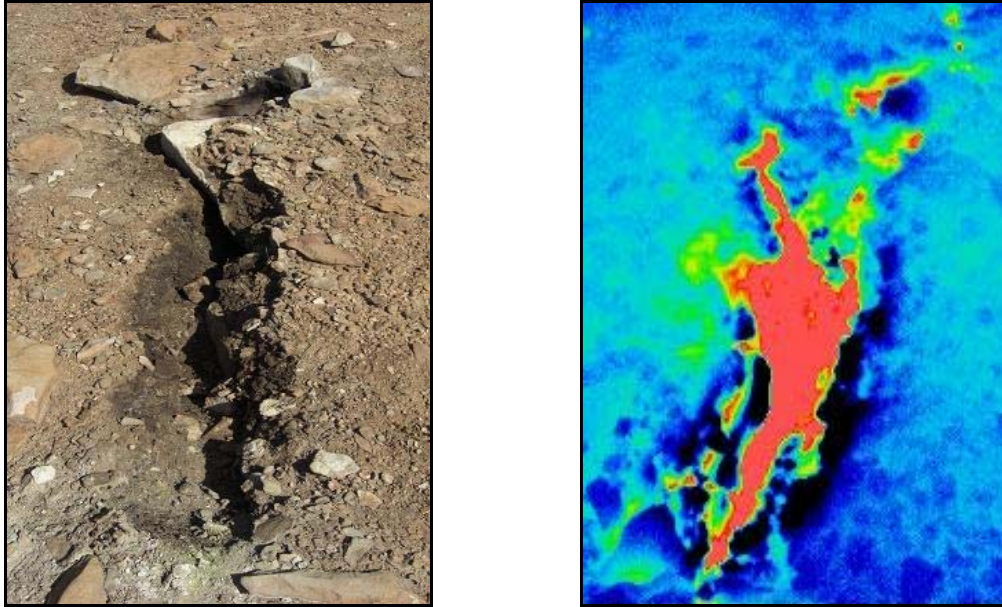


**Figure 53:** a) the surface expression above an active coal fire and b) the thermal image at the same location. The hottest recorded surface temperature is 759°F over this fissure.

Additional data are needed to characterize the fire as a way to help formulate a numerical model of the fire. However, we have begun identifying various numerical models that explore solid phase combustion in the presence of oxidizer convection. The most relevant model is that of [88]. In this work, consumption of the solid phase by a moving combustion wave is considered. A constant flux of an oxidizer is injected into the system (termed forced convection), a condition that can be observed at the Colorado fire, where wind gusts provide  $O_2$  through the fissures to the burning coalbed.

There are three sets of data that will be collected before the boundary conditions for Aldushin's model can be adapted appropriately. The first is a set of gas measurements by gas chromatography (GC) of the compositions of venting gases. Compositions of gases from different areas of the field may allow us to monitor the directionality of fire growth, as compositions of product gases are strong functions of temperature. The second set is an image of the subsurface using a device such as a ground penetrating radar (GPR), which may indicate whether or not coal in between the fissures is being consumed as well. Based on our observations to date, we are certain that the combustion zone propagates along the fissures, but there are no data indicating whether the combustion front can also propagate in the direction transverse to the fissures. Lastly, we hope to be able to collect core samples from the area. This can be done fairly easily given the

shallow depth to the coal formation. Core samples will help us determine how deeply the coal fire has penetrated the 10m thick coal layer.

After the coalbed fire is accurately characterized based on field observations, we will create the simplest numerical model that represents these physics. From the numerical model, we will delineate a relationship between the combustion front propagation velocity, its direction, and the pressure gradient governing its movement through the coal seams. This functional relationship will be used to explore possible fluid injection schemes to slow or stop the fire propagation. In addition, fluids that can starve the region of O<sub>2</sub> and effectively remove heat from combustion regions will be considered.

## 6. Seal Integrity and Feasibility of CO<sub>2</sub> Sequestration in the Teapot Dome EOR Pilot: Geomechanical Site Characterization

One of the main issues to be addressed for CO<sub>2</sub> sequestration to be a viable carbon management solution is the risk of CO<sub>2</sub> leakage. From a technical perspective, depleted or mature oil and gas reservoirs hold great promise as sequestration sites due to the fact that hydrocarbons were held in them for geological periods of time, implying the presence of effective trap and seal mechanisms. However, it has long been known (e.g., Raleigh et al. 1976) that fluid injection causes changes in the pore pressure and stress field that could potentially alter the initial seal of the reservoir by either hydraulically fracturing the cap rock or by triggering slip on pre-existing faults by reducing the effective normal stress on the fault plane (see review by Grasso [74]).

It is thus essential to study the relationship between faults and the present-day stress field to predict which faults could be potential leakage routes. Another way of compromising seal integrity is by hydrofracturing the cap rock, which occurs when the pore pressure at the top of the reservoir is as high as the least principal stress in the overlying unit. In both cases, geomechanical characterization can be used to derive the pressures and rates of injection needed to reach those critical values and can therefore help in evaluating the potential risk of leakage.

### *Teapot Dome CO<sub>2</sub> EOR-Carbon Storage Pilot*

The Teapot Dome Field Experimental Facility (Figure 54) is owned by the U.S. government and operated by the U.S. Department of Energy (DOE) and the Rocky Mountain Oilfield Testing Center (RMOTC). To evaluate the scientific and technical feasibility, the project team is working with interested industry and research partners to design the first CO<sub>2</sub> injection experiment, a small, short-duration EOR pilot, which would use existing wells and infrastructure. Project execution will be primarily contingent upon receiving adequate support from RMOTC's industry and research partners. The project envisioned would target the Tensleep Formation, with a minimum of ~60 tons/day CO<sub>2</sub> for a minimum of ~1.5 months.

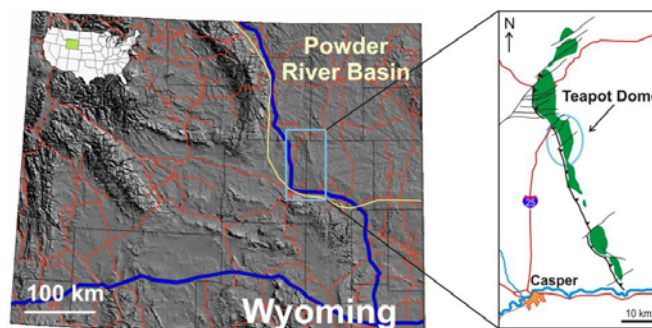


**Figure 54:** Location of Teapot Dome. Satellite image of Wyoming (left), Salt Creek structural trend, topographic relief in green (right) (courtesy of RMOTC).

### Geology of Teapot Dome

Teapot Dome is an elongated asymmetrical, basement-cored anticline with a north-northwest axis. It is part of the Salt Creek structural trend (Figure 54), located on the southwestern edge of the Powder River Basin (Cooper and Goodwin 1998, Beinkafner 1986). The anticline (Figure 55) is interpreted as a west verging fault propagation fold, typical of many Laramide age folds in the Rocky Mountain Region [77, 80].

The stratigraphy of Teapot Dome consists of Upper Cretaceous to Mississippian strata of diverse origin ranging from offshore sediments to coastal sandstone dunes over a granitic basement. The Tensleep Formation, of Pennsylvanian age, is the deepest hydrocarbon producing interval in the anticline. In this area it consists of interdune deposits such as eolian sandstones, sabkha carbonates, evaporites (mostly anhydrite), and extensive beds of very low permeability dolomiticrites. The average porosity is 10 % (5 – 20 % range), and the average permeability is 30 mD (10 – 100 mD range). The average net thickness is 15 m. The reservoir has a strong aquifer drive and therefore hydrostatic reservoir pressure, and the reservoir temperature is ~88°C. The Tensleep Formation is divided into several intervals, of which the approximately 30 m thick B-Sandstone is the main producing horizon and the proposed storage interval for this experiment. The Opeche Shale plus the anhydrite of the Minnekahta Member of the Permian Goose Egg Formation comprise the regional seal of the Tensleep Formation throughout Wyoming.

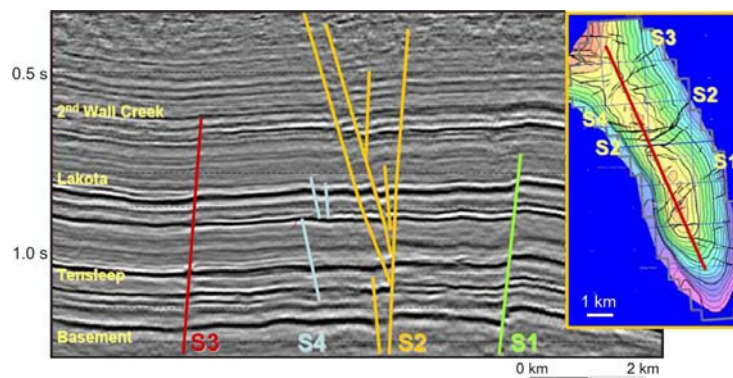


**Figure 55:** NW-SE cross section through Teapot Dome (left). Depth-structure map of 2nd Wall Creek Sandstone with locations of seismic line (right) [72].

In the area under study the Tensleep Formation has its structural crest at 1675 m below surface covering an area of approximately 1.2 km<sup>2</sup> (Figure 56). The reservoir is trapped against a NE-SW trending fault to the north resulting in a three-way closure trap. A three-way trap is one in which the fluids are trapped by structural relief and the top seal on three sides of the trap, and by a sealing fault on the fourth side. The trapping fault, named S1, has been described as an oblique-slip basement-cored right-lateral tear fault [80]. Figure 56 is a time-structure map of the Tensleep Formation. In a time-structure map the formation structure is mapped in two-way seismic travel time (TWTT) expressed in milliseconds (ms), instead of depth/elevation. The red line, corresponding to the 1050 ms contour, indicates the oil/water contact. There is approximately 40 ms TWTT of

structural closure (approx. 100 m at velocity = 2500 m/s) which is the vertical distance from structural crest to the spill point of structure on this reservoir. This means that around 100 m of fluid column height can be trapped.

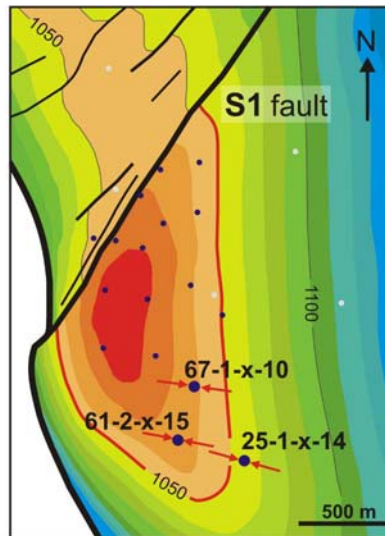


**Figure 56:** Time-structure map in milliseconds (ms) of Tensleep Formation in Section 10 area showing the S1 fault, oil-contact area (red contour line),  $S_{Hmax}$  direction and analyzed wells (blue dots).

#### *Geomechanical Characterization*

To obtain the geomechanical model and perform a critically stressed fault analysis we follow the methodology of Zoback et al. [87] for assessing the stress state and Wiprut and Zoback [85] for assessing fault stability. The parameters needed for a full definition of the stress state are summarized in Table XIII along with the data sources used to constrain the parameters.

**Table XIII:** Parameters and data needed to define the stress tensor and the geomechanical model.

Parameter	Data
Vertical Stress ( $S_v$ )	Density logs: $S_v(z_0) = \int_0^{z_0} \rho g dz$
Minimum horizontal Stress ( $S_{hmin}$ )	LOT, XLOT, minifrac
Maximum horizontal Stress ( $S_{Hmax}$ )	Modeling wellbore failures
Stress orientation	Orientation of wellbore failures
Pore Pressure	Measure, sonic logs
Rock strength	Lab, logs, modeling well failure
Faults and fractures	Seismic, wellbore imaging

Density, sonic and Formation Microresistivity Imager (FMI) logs in the 67-1-x-10, 61-2-x-15 and 25-1-x-14 wells (see Figure 56 for well locations) were analyzed to quantify the stress tensor ( $S_v$ ,  $S_{Hmax}$  and  $S_{hmin}$ ) in the area of interest

Drilling-induced tensile fractures were analyzed in FMI logs from the three study wells. Interactive image analysis yielded 420 observations of drilling-induced tensile fractures over a depth range of 400 – 1800 m. The average maximum horizontal stress ( $S_{Hmax}$ ) direction is  $116^\circ \pm 15^\circ$  AZ (N64°W). This value is consistent with the  $S_{Hmax}$  orientation of  $105^\circ$  AZ (N75°W), observed by Milliken and Koepsell (2003) in well 67-1-x-10. If we consider only the drilling-induced tensile fractures in the Tensleep Formation, the direction of  $S_{Hmax}$  is  $100^\circ \pm 15^\circ$  AZ (N80°W).

In well 67-1-x-10 tensile fractures are found through most of the column while in well 25-1-x-14 there are surprisingly fewer features, even though the two wells were drilled with similar mud weights. In well 61-2-x-15 only part of the Tensleep Formation was imaged, where tensile fractures are present as well. Note the lack of breakouts at the depth of the Tensleep Formation.

The rock strength used in the horizontal stresses magnitude estimations was determined from sonic logs using an empirical relationship developed by Chang et al (2006) for weak and unconsolidated sandstones in the Gulf Coast. The average estimated value of the B-Sandstone rock strength varies from 55 MPa to 65 MPa in the three wells.

The magnitudes of  $S_{Hmax}$  and  $S_{hmin}$  were estimated from observed occurrence of drilling-induced tensile fractures and non-occurrence of wellbore breakouts, following Zoback et al. (2003). Since no breakouts were observed it was assumed that the calculated rock strength is the lower bound for the actual rock strength of the rock and acts as an upper bound for the  $S_{Hmax}$  magnitudes, as well as the zero tensile strength blue line. The mud weight and temperature, obtained from the drilling reports, were also considered and with these constraints the range of possible stress magnitudes was estimated. From the data in this particular well  $S_{Hmax}$  could range from 31.5 to 43.0 MPa and  $S_{hmin}$  from 24.5 to 28.5 MPa.

The analysis of the three studied wells yielded a NF/SS faulting stress state where  $S_{Hmax} \approx S_v > S_{hmin}$ . This is supported by fault movement observed in the youngest sections of the 3D seismic cube and by the displacements on NE/SW faults observed in the surface outcrops and trenches [78].

Due to the absence of leakoff or minifrac tests in the Tensleep Formation to obtain the magnitude of  $S_{hmin}$  (which would also better constrain the magnitude of  $S_{Hmax}$ ), the critically stressed fault analysis was first performed with an  $S_{hmin}$  gradient of  $0.6 S_v$  and  $S_{Hmax} = S_v$  expected for a NF/SS environment. Available data from a minifrac test performed in the 2nd Wall Creek reservoir confirms  $S_{hmin} = 0.6 S_v$ . This minifrac test was performed in the well 71-1-ax-4, approximately 2 km northwest of the area under

study, where the 2nd Wall Creek reservoir is at approximately 900 m depth and 720 m above the top of the Tensleep Formation.

With this information, a 2nd order stress tensor ( $S$ ) that only varies with depth was defined as the base case scenario to estimate the leakage potential of the S1 fault. Since the present stress state corresponds to a NF/SS environment,  $S_1 = S_{Hmax}$ ,  $S_2 = S_v$  and  $S_3 = S_{hmin}$ .

#### *Fault Slip Potential Using Coulomb Criterion*

The S1 fault was mapped in the available 3D seismic survey and converted to depth using the seismic dip processing moveout (DMO) velocities. To determine the risk of leakage through the S1 fault, the authors evaluated the state of stress and pore pressure acting on the fault plane following the methodology of Wiprut and Zoback [85], which will be described below.

It is important to note that the orientation of the S1 fault has an azimuth of  $36^\circ$  which is nearly perpendicular to  $S_{Hmax}$  (see Figure 56). Therefore it immediately appears unlikely that this fault could slip in a NF/SS stress field.

To perform the quantitative analysis, the shear ( $\tau$ ) and normal stresses ( $S_n$ ) were calculated for each element of the fault. Then Coulomb failure criteria were applied to predict the critical pressure ( $P_c$ ) necessary to reactivate fault slip, assuming a coefficient of friction ( $\mu$ ) of 0.6.

$$P_c = S_n - \tau / \mu \quad (36)$$

Comparing this  $P_c$  with a reference  $P_p$ , modeled from the pressure data of the field, a critical pressure perturbation ( $P_{cp}$ ) was obtained.  $P_{cp}$  indicates the pore pressure change to enable a fault element to slip given the stress state, fault orientation and reference  $P_p$ . In this analysis it is assumed that active faults are potential conduits for fluid migration such that  $P_{cp}$  indicates the leakage potential for each portion of the fault (Figure 57a). It is important to note that this is a conservative approach for evaluating likelihood of  $CO_2$  leakage along the fault, even though the amount of potential leakage could be quite small if the area of fault slip is small.

For the base case stress scenario defined in the previous section, at the depth of the Tensleep Formation (red line in Figure 57a), approximately 17 MPa of excess pressure would be required to cause the fault to slip. This corresponds to a  $CO_2$  column height of approximately 2500 m (at a density of  $700 \text{ kg/m}^3$ ). Since the average closure of the Tensleep Formation in this area is no more than 100 m, it is anticipated that the S1 fault is not at risk of reactivation and therefore will not be a leakage pathway for  $CO_2$  migration.

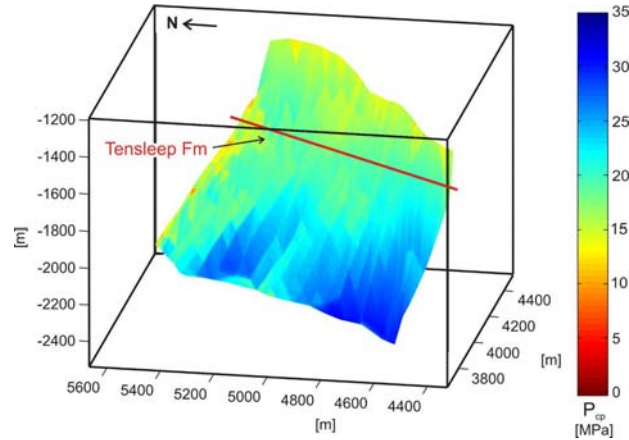


**Figure 57a:** Fault surface color-coded with critical pressure perturbation values indicating the fault slip potential. At the Tensleep Formation (red line), ~ 17 MPa of excess pressure would be required to cause the fault to slip.

To evaluate how poro-elastic effects affect fault stability, Equation 37 was incorporated in the previous analysis. This equation was derived for an isotropic, porous and elastic reservoir that is infinite in extent. Segall and Fitzgerald [83] showed that this relationship is also valid if the ratio of lateral extent to thickness of a reservoir is greater than 10:1 (which is the present case).

$$\Delta S_{Hor} = \alpha \frac{(1-2\nu)}{(1-\nu)} \Delta P_p \quad (37)$$

$S_{Hor}$  corresponds to both  $S_{Hmax}$  and  $S_{Hmin}$ ,  $\alpha$  is Biot's coefficient and  $\nu$  is Poisson's ratio [69].

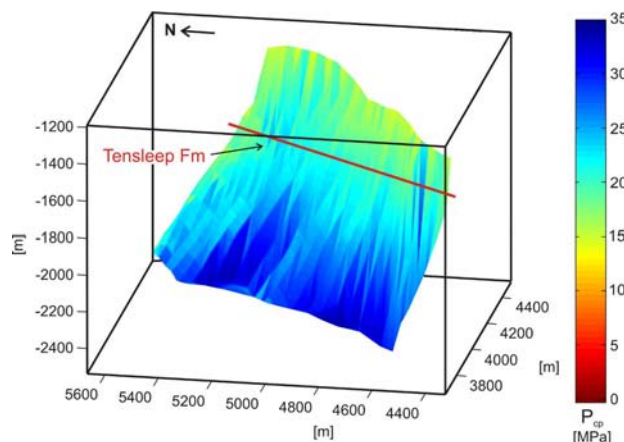


**Figure 57b:** Fault surface color-coded with critical pressure perturbation values indicating the fault slip potential considering the poro-elastic effect. At the Tensleep Formation (red line), ~ 20 MPa of excess pressure would be required to cause the fault to slip.

$P_{cp}$  was estimated for a potential CO<sub>2</sub> injection-induced increase in  $P_p = 10$  MPa,  $\alpha = 1$  and  $\nu = 0.25$ . As it is shown in Figure 57b, the poro-elastic effects increase the amount of extra pressure needed to cause slip in the S1 fault. At the depth of the Tensleep Formation (red line in Figure 57b) approximately 20 MPa of excess pressure would be required.

### Critical Pressure Perturbation Sensitivity Analysis

To evaluate how the uncertainties in the horizontal stress magnitudes and in the strike and dip of the fault with respect to the stress field affect the slip potential of the S1 fault, a sensitivity analysis of those parameters was performed. In the case of the fault orientation we need to account for the limits in the seismic resolution as well as for the uncertainties in the time-depth conversion of the structures mapped. During the seismic acquisition, the travel time of a wave from the surface to the objective at depth is measured. To convert the measured travel time to depth it is necessary to assume the velocity of the wave, from which comes the uncertainty on real depths and geometry of the bodies under consideration.

Random distributions of the components of the stress tensor were generated based on the mean, minimum and maximum stress values estimated for each well. For the base cases of a normal fault ( $S_1 = S_v$ ,  $S_2 = S_{Hmax}$  and  $S_3 = S_{hmin}$ ) and strike-slip ( $S_1 = S_{Hmax}$ ,  $S_2 = S_v$  and  $S_3 = S_{hmin}$ ), cases were analyzed separately using over 10,000 Monte Carlo Simulations. In the case of normal faulting,  $S_{Hmax}$  is less than  $S_v$  and greater than  $S_{hmin}$ . In the strike-slip case,  $S_v$  is less than  $S_{Hmax}$  and greater than  $S_{hmin}$ . Figure 58, for the normal faulting case, shows the fault slip potential probability as a function of reservoir pressure for variations of the indicated component of the stress tensor (while the others remained fixed). From this analysis it was established that in 99.9% of the cases a pressure perturbation of more than 10 MPa would be necessary to induce slip on the S1 fault.

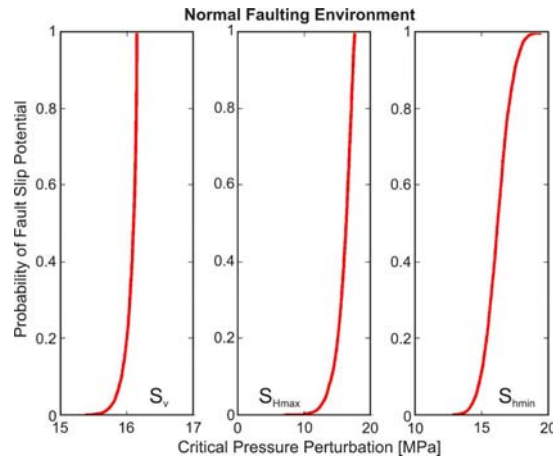


**Figure 58:** Fault slip potential probability for Normal Fault environment, as a function of each of the components of the stress tensor, varying  $S_v$  (maintaining  $S_{Hmax} = 34.4$  MPa and  $S_{hmin} = 25.7$  MPa fixed) (left); varying  $S_{Hmax}$  (maintaining  $S_v = 39.9$  MPa and  $S_{hmin} = 25.7$  MPa fixed) (center) and varying  $S_{hmin}$  (maintaining  $S_v = 39.9$  MPa and  $S_{Hmax} = 34.4$  MPa fixed) (right).

To account for the uncertainties with respect to the geometry of the fault, we also evaluate fault slip probability as a function of variations in fault azimuth and dip. These cases were evaluated with the mean values of the stress tensor. The dip angle has the biggest impact on the fault slip potential. In 99.9% of the test scenarios, the critical pressure perturbation values are above 10 MPa.

In summary, even in the most pessimistic risk scenario, a CO<sub>2</sub> column height of approximately 1500 m (using a reasonable average density  $\sim 700 \text{ kg/m}^3$ ) is required to reach the lowest estimated  $P_{cp}$  value ( $\sim 10 \text{ MPa}$ ).

### *Hydraulic Fracture Limit for Caprock*

Better constraints on the least principal stress ( $S_{hmin}$ ) in both the reservoir and the caprock are necessary not only to more precisely estimate the magnitudes of  $S_{hmin}$  and  $S_{Hmax}$ , but also to get more exact values for the maximum pressure increase at the top of the structure that the reservoir could sustain before hydrofracturing the overlying unit.

Knowledge on the hydraulic fracture limit of the caprock is important for two reasons. It is useful for evaluating the risk of leakage, and it provides a constraint on the maximum CO<sub>2</sub> column height that the reservoir can contain if hydraulic fracturing of the overlying unit occurs before the column reaches the spill point of the structure. In other words, the hydraulic fracture limit helps to evaluate whether there is a dynamic constraint for the CO<sub>2</sub> column in the area under study (e.g. [72]).

In order to better estimate the value of  $S_{hmin}$  we need either a leak-off test or minifrac in the caprock. In the drilling reports of the three studied wells, no fluid loss information was recorded and no leak-off test or minifrac test data are available at Teapot Dome, other than the one mentioned in the 2<sup>nd</sup> Wall Creek reservoir.

With the better constrained value of  $S_{hmin}$  it will be possible to evaluate whether the hydrofracture limit of the Tensleep Formation or the caprock could be a lower constraint in the sustainable injection pressure than the estimated  $P_{cp}$  on the fault.

### *Conclusions*

A comprehensive geomechanical model for the Tensleep Formation was generated in the context of providing the technical foundation required for RMOTC and its partners to consider and design a CO<sub>2</sub> injection project at Teapot Dome. This model allows the project team to quantitatively estimate the pore pressure at which the S1 fault would slip, and therefore supports predictions about the risk of leakage in the target storage unit.

The components of the stress tensor as well as the geometry of the fault were considered in a probabilistic sensitivity analysis, from which it was established that for even the most pessimistic scenario (lower values of fault dip), 99.9% of the cases would require at least 10 MPa of excess pressure to cause the S1 fault to reactivate. This pressure would be seen at the top of a CO<sub>2</sub> column of approximately 1500 m in height. As the average closure of the Tensleep Formation structure in this area does not exceed

100 m, the S1 fault does not appear to be at risk of reactivation and therefore providing a leakage pathway for CO<sub>2</sub> under the present stress field.

Planned refinements to this analysis are direct measurements of  $S_{hmin}$  in the Tensleep Formation as well as in the caprock. These data will provide more reliable estimates for the maximum sustainable pressure before hydrofracturing the caprock, as well as for the maximum CO<sub>2</sub> column height that this structure could support. The sensitivity analysis highlighted the influence of the fault dip angle in the  $P_{cp}$  estimation. Thus refining the time-depth conversion model to accurately estimate the dip of the fault is also essential. The possible presence of faults with smaller displacements than the one detectable by the seismic (but potentially more favorable orientations for reactivation) will have to be evaluated. These can be observed either in FMI fracture interpretations and well correlation, or from surface reservoir analogs at Tensleep Formation outcrops, which could have the same deformation style present in the subsurface.

## 7. Progress

The potential for significant storage of anthropogenic CO<sub>2</sub> in deep, unmineable coalbeds depends on:

1. the amounts of CO<sub>2</sub> and other gases that adsorb as a function of pressure, temperature, and composition of the injected gas,
2. our ability to predict the flow of CO<sub>2</sub>, so that the quantity of CO<sub>2</sub> that can be stored can be estimated along with the number of wells needed,
3. understanding of the effects of the CO<sub>2</sub> on the properties of the coal, both for reasons of managing the resulting effects on permeability and flow and for understanding changes in properties that might enable measurements to determine the extent of CO<sub>2</sub> propagation in the subsurface,
4. our ability to predict the situations in which CO<sub>2</sub> might leak from a coalbed,
5. our ability to detect the movement of CO<sub>2</sub> in the subsurface and leakage from the intended zone of storage if it occurs.

This report outlines progress in each of these areas. Measurements of adsorption of N<sub>2</sub>, CH<sub>4</sub>, and CO<sub>2</sub> have been completed, and provide a framework for studying the effects of adsorption on the permeability of powdered coal samples. Experimental evidence suggests that permeability can be maintained by injecting a mixture of N<sub>2</sub> and CO<sub>2</sub> rather than a pure stream of CO<sub>2</sub>. A new measurement technique and laboratory system has been developed for estimating the low-frequency compressibility and attenuation of coal samples using Differential Acoustic Resonance Spectroscopy (DARS). Compressibility data obtained from the DARS system can be directly applied to seismic monitoring field and modeling studies. Measurements of the static elastic properties and strength of intact coal samples have begun. It is anticipated that these data will improve models of the effect of hydraulic fracturing on injectivity of CO<sub>2</sub> in coal seams.

Three types of models of flow in coalbeds have been constructed. Analytical solutions have been obtained for the flow of water and gases (CH<sub>4</sub>, CO<sub>2</sub>, and N<sub>2</sub>) in coal in one dimension. This approach delineates the interplay of adsorption and flow to determine the separations of components that take place during flow in a coal bed. Numerical models of laboratory-scale flows have been developed and used to demonstrate that the standard Langmuir model of adsorption is not sufficient to describe observations in relatively simple flow settings, but the ideal adsorbed solution model provides a better description. Field-scale modeling reveals the impact of gravity segregation on the fraction of a coalbed that can be contacted, and it indicates that barriers to vertical flow above the coalbed will be required if leakage is to be avoided.

Analysis of the stress setting of a potential CO<sub>2</sub> storage project in an oil reservoir demonstrates techniques for analysis of how the local stress setting controls the potential for faults to provide potential leak paths. Those techniques will be equally valuable in similar analyses of fault activation in coalbeds.

Observations of a subsurface fire in a coalbed have been made. Such fires account for significant CO<sub>2</sub> emissions, and if they can be understood in sufficient detail, it may be possible to develop ways to extinguish them. The observations reported are a first step toward building that understanding.

Efficient monitoring will be an important component of the subsurface behavior of any CO<sub>2</sub> storage project. New techniques to do that have been developed and are being explored.

The extent to which coalbeds will be feasible locations to store CO<sub>2</sub> remains to be seen. The progress reported here indicates that it will be possible to adsorb CO<sub>2</sub> in the subsurface. Quantitative assessment of the potential worldwide will require additional progress outlined in the next section.

## 8. Future Plans

### 8.1 Integrated Laboratory Measurements of the Physical and Transport Properties of Coal

#### *DARS Measurements of Attenuation and Compressibility*

DARS I measurements can be used to accurately estimate the acoustic properties of small samples of coal at room temperature and atmospheric pressure using a single reference fluid (silicon oil). The DARS I measurements discussed above are robust and highly repeatable. However, the acoustic properties of coal are affected by pressure and saturation. For purposes of CO<sub>2</sub> monitoring, the changes in compressibility and attenuation as a function of pressure and saturation are needed under simulated in situ conditions. We are completing design for a new system, DARS II, with variable pressure and fluid saturation control. DARS II will permit the measurement of changes in acoustic properties with changes in pressure and saturation under in situ injection conditions, and for diagnosing the dynamics of CO<sub>2</sub> adsorption in the laboratory. The DARS II conceptual design is illustrated in Figure 59. The challenge in this design is to move the sample (relative to the cavity under pressure) in order to generate the DARS profile. A major part of the future work is the final design of DARS II and its construction (expected in late summer, 2007). We then plan to make a suite of measurements for compressibility and attenuation on several samples of coal at various pressures and saturations of carbon dioxide and methane, and integrate the DARS results with the other laboratory measurements from the labs of Zoback and Kovscek.

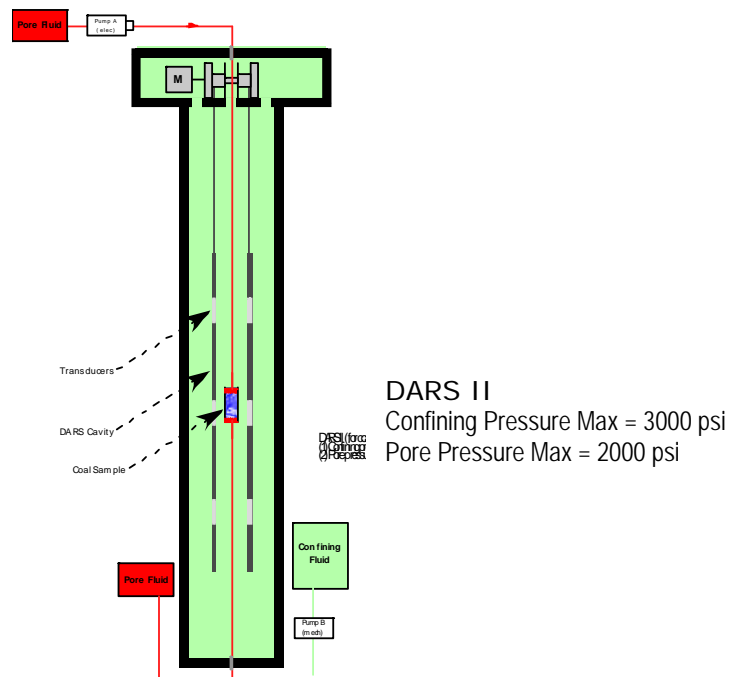


**Figure 59:** The DARS II design incorporates a fixed sample under differential confining pressure and with variable fluid saturation. The cavity is moved to generate the DARS profile.

### *Sorption-Induced Permeability Change of Coal during Gas-Injection Processes*

Most experiments performed to date were conducted on ground coal. A similar set of experiments will be performed using coal core. Transient and steady state permeability will still be measured for different gas compositions and pore pressures at constant net effective stress. The amount and composition of the adsorbed gases will be measured at the same time as the measurement of permeability. Swelling of coal due gas injection will be also measured by tracking the volume of confining fluid in the annular space of the coreholder. By measuring adsorption, permeability, and swelling simultaneously, we will be able to directly calculate the porosity change of the sample. We are planning to modify our existing laboratory system to accomplish these experimental goals (Figure 60). In the new setup, two additional mass flow meters measure the mass of gas flowing into and out of the core; the pump is for providing overburden pressure and measuring swelling; and the gas analyzer is for measuring the outlet gas composition.

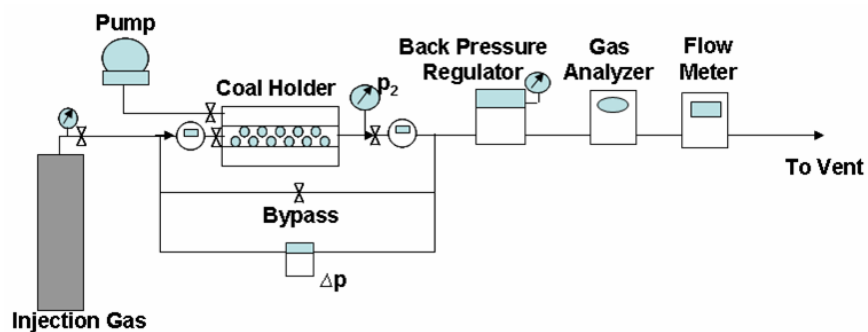


**Figure 60:** Experimental setup for measuring permeability reduction and gas adsorption. The circular devices shown at the inlet and outlet of the coal holder represent additional flow meters.

### *Coalbed Wettability and Relative Permeability*

We plan to continue our development of air-water-coal relative permeability curves. Comparing the relative permeability curves of coal systems as a function of pH provides insights about how multiphase flow and wettability are affected by dissolution of  $\text{CO}_2$  into coal-water systems. In order to better characterize the effect of  $\text{CO}_2$  on coal wettability and synthesize these results with our measurements of gas permeability and adsorption, we plan to migrate our experimental systems from powdered coal samples to intact whole core samples. Moving to intact core samples also eases the integration of our data with data collected on whole core samples for geomechanical and acoustic properties.

### *Measurements of Static Physical Properties, Ultrasonic Velocities, and Permeability*

We plan to continue measuring the elastic properties and flow properties of intact coal samples for a variety of stress boundary conditions and gas compositions. We are particularly interested in studying the shrinkage and swelling of coal as a function of adsorption, as we have the capability to measure changes in volumetric strain and porosity directly, using axial and radial displacement gauges placed on the sample and core holders. We plan to test the validity of the widely used Palmer-Mansoori equation, and modify it as necessary to accurately model our observations. We also plan to study the strength and plasticity of coal as a function of both temperature and gas composition. Our goal is to produce a complete data set that could be used for geomechanical and fluid flow models of carbon dioxide injection into unmineable coal beds. We will continue to work closely with the other experimental groups, and propose the following workflow for an integrated set of laboratory measurements on coal samples.

### *Example workflow for the integrated laboratory effort*

Our proposed workflow is shown in Figure 61 takes into account the need to keep the sample in a relatively constant state during testing, to facilitate comparison of the data collected in the individual laboratories. Therefore, the order for sample testing is based on the potential of each laboratory apparatus to permanently alter the sample. Because the DARS II apparatus is non-destructive, the workflow begins there.

Following careful characterization of a coal sample, including CT scanning to map cleats, cracks, and damage, the sample would be moved to the Harris laboratory for testing in the DARS II apparatus. Attenuation and compressibility would be measured as function of frequency and pressure for a range of gas and water saturation levels. The sample would then be scanned again to ensure that it has not been altered or damaged.

Following this second characterization step, the sample would go to the Kavscek laboratory, where permeability would be measured as a function of adsorption and pore pressure (constant effective pressure) for various gas saturations. In addition, the displacement of nitrogen, methane, or other gases by CO<sub>2</sub> might be measured.

Following this step, the sample would be scanned once again, before being moved to the Zoback laboratory. Here, initial porosity would be measured by the gravimetric method, for comparison against prior helium porosity measurements. Finally, the static elastic properties, ultrasonic velocities, and permeability of the sample would be measured as a function of effective stress and adsorption. In addition, strength and plasticity as a function of temperature or the volumetric swelling of the sample due to CO<sub>2</sub> adsorption could be measured.

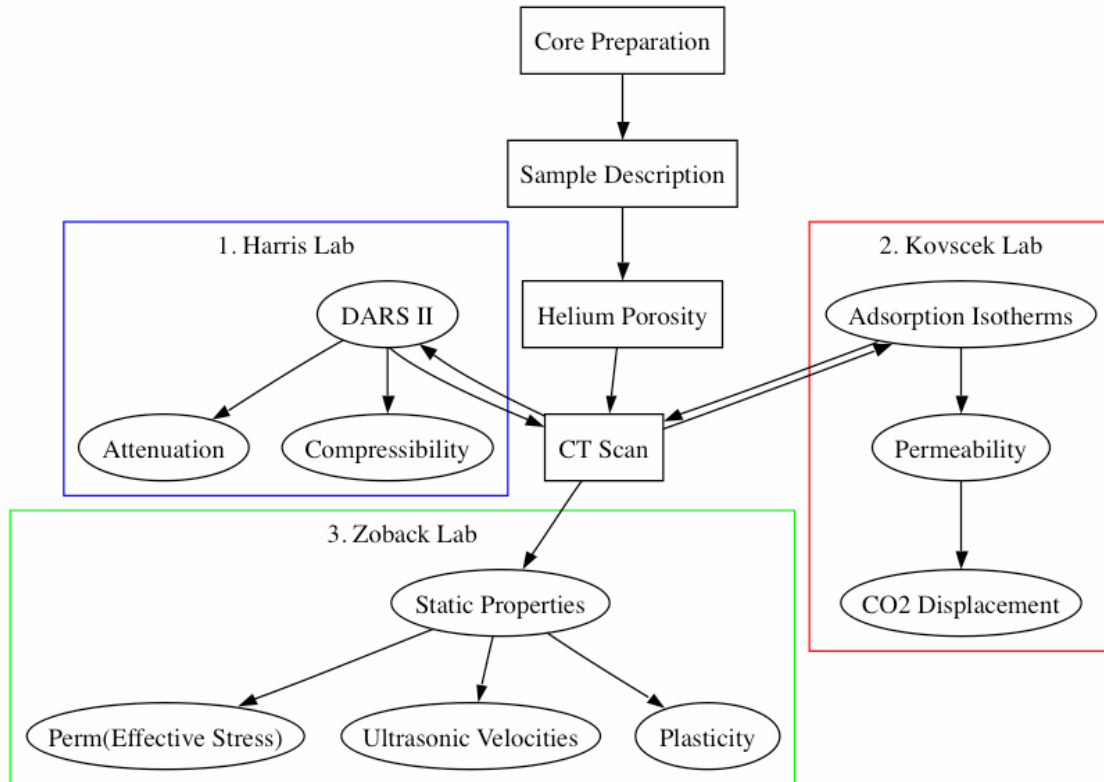


**Figure 61:** Proposed workflow for the integrated laboratory effort.

## 8.2 Analytical and Numerical Modeling of the Flow and Transport Properties of Coal

Research to develop analytical solutions for one-dimensional flow of three-component gases and water through fractured coal is now complete. The solutions obtained illustrate the sensitivity of flow behavior to adsorption strength, the volume change that occurs as components adsorb and desorb, and the relative permeability of the coal to gas and water. Experiments to test those predictions are underway, in measurements funded by the GCEP project and in the coal equivalent of a slim tube measurement being performed with other support. Development of simulation tools continues for numerical solutions of the differential equations for flows in one, two and three dimensions with more than four components present and for flows in three dimensions in which gravity segregation of the injected gas mixture is also important. Extensions of our work in this area include:

- incorporation of nonideality for the gas phase because at test pressures the fugacity coefficient of carbon dioxide is substantially less than 1;
- calculations to date have not included hysteresis among adsorption and desorption of gas species and inclusion of this effect may improve the accuracy with which nitrogen banking and elution are predicted;
- an exploration of the degree of numerical dispersion in our numerical solutions;

- verification of the numerical results versus our full suite of gas displacement experimental results that span from injection of pure nitrogen to mixtures of nitrogen and carbon dioxide to pure carbon dioxide.

### **8.3 Modeling and Field Studies of Coalbed Fires**

The effort to understand coalbed fires is now well underway with observations at a field site occurring simultaneously with work on modeling the flow setting that controls supply of O<sub>2</sub> to the combustion zone. The field work will provide one example of how the combustion zone propagates in the subsurface, and the modeling work will develop quantitative estimates of the pressure gradients that arise from the buoyancy-driven flows that cause hot combustion products to exit through surface fissures and that draw air into the subsurface. The objective of that work is to develop a picture of the pressure gradients sufficient to allow design of ways to disrupt the pressure gradients in such a way as to exclude O<sub>2</sub> from the combustion zone. A key issue is how to represent the boundary conditions for gas intake and exit and to understand the modes of propagation of the combustion zone in the subsurface. A combination of observations and modeling of the interplay of convection, reaction, and heat transfer will be required to understand the initiation and propagation of coalbed fires.

### **8.4 Simulation Studies of Quasi-continuous Seismic Monitoring**

The monitoring research is focused on quasi-continuous subsurface imaging. The major effort for the future falls in two categories: (1) implement and test the temporal integration strategy; (2) Test a “realistic” full simulation scenario of the quasi-continuous seismic imaging. The temporal integration strategy involves finding the optimal combination of data evolution, model evolution, and inversion algorithms that will permit quasi-continuous imaging from sparse datasets at reduced computational effort. The full simulation scenario involves using results from flow models, coal properties measured with DARS, and realistic seismic modeling and imaging methods to illustrate and assess the spatial and temporal resolution capabilities of the quasi-continuous monitoring strategy. An underlying task for all the monitoring research is to expand our existing 2-D numerical simulators to full 3-D. This effort may require some parallelization of the algorithms. An important though ancillary result will be the comparison of the fast technique for simulating an idealized image with the slow technique of simulating the more realistic image generated by modeling and inversion of the entire seismic acquisition and imaging process. If the former proves to produce accurate results under various conditions, we will have a fast way of quickly simulating monitoring strategies and storage/leak scenarios for 100’s of time-lapse models generated from flow simulations.

## Publications

1. Chiaramonte, L., Zoback, M., Friedmann, J. and Stamp, V. (in press). Seal Integrity and Feasibility of CO<sub>2</sub> Sequestration in the Teapot Dome EOR Pilot: Geomechanical Site Characterization. *Journal of Environmental Geology*. Submitted: June 2006.
2. Hesse, M.A., Tchelepi, H.A., Cantwell, B.J., and Orr, F.M., Jr.: "Transition in the propagation regime of a gravity current in a horizontal porous layer," in press *J. Fluid Mech.* 2006.
3. Lucier, A., M.D. Zoback, N. Gupta and T. S. Ramakrishnan, 2006, Geomechanical aspects of CO<sub>2</sub> sequestration in a deep saline reservoir in the Ohio River Valley region: *Environmental Geosciences*, **13**, 1-19.
4. Riaz, A., Hesse, M., Tchelepi, H. and Orr, F.M., Jr.: "Onset of Convection in a Gravitationally Unstable, Diffusive Boundary Layer in Porous Media," *J. Fluid Mech.* **548** (2006) 87-111.
5. Spiteri, E.J., Juanes, R., Blunt, M.R., and Orr, F.M., Jr.: Impact of relative permeability hysteresis on geological CO<sub>2</sub> storage, *Water Resour. Res.*, **42**, W12418, doi:10.1029/2005WR004806, 2006.
6. Tang, G.-Q., K. Jessen, and A. R. Kovscek, "Laboratory and Simulation Investigation of Enhanced Coalbed Methane Recovery by Gas Injection," *Transport in Porous Media*, submitted Nov. 2006.
7. Chiaramonte, L., Zoback, M., Friedmann, J. and Stamp, V. (2006). Geomechanical Reservoir Characterization for Prediction of the Likelihood of Faulting Induced by CO<sub>2</sub> Sequestration, *Eos Trans. AGU*, **87** (52), Fall Meet. Suppl., Abstract T12A-07.
8. Chiaramonte, L., Zoback, M., Friedmann, J. and Stamp, V. (2006). CO<sub>2</sub> Sequestration, Fault Stability and Seal Integrity at Teapot Dome, Wyoming. NETL 5th Annual Conference on Carbon Capture & Sequestration Proceedings, Alexandria, VA.
9. Chiaramonte, L., Zoback, M., Friedmann, J. and Stamp, V. (2006). CO<sub>2</sub> sequestration, fault stability and seal integrity at Teapot Dome, Wyoming. Proceedings of the 8th International Conference on Greenhouse Gas Control Technology, Trondheim, Norway, June 19-22
10. Lucier, A., M. D. Zoback, N. Gupta and T. S. Ramakrishnan, 2006, Geomechanical aspects of CO<sub>2</sub> sequestration near coal-burning power plants in the Midwestern United States: Proceedings of the 8th International Conference on Greenhouse Gas Control Technologies, Trondheim, Norway, June 19-22.
11. Ross, H. E. and Zoback, M. D., 2006, Reservoir characterization of coals in the Powder River Basin, Wyoming, USA, for CO<sub>2</sub> sequestration feasibility studies: Proceedings of the 8th International Conference on Greenhouse Gas Control Technologies, Trondheim, Norway, June 19-22.
12. Hesse, M.A., Tchelepi, H.A., and Orr, F.M., Jr.: "Natural convection during aquifer CO<sub>2</sub> storage," Proc. 8<sup>th</sup> Intl. Conf. on Greenhouse Gas Control Technologies, Trondheim, Norway, June 19-22, 2006.
13. Ide, S.T., Jessen, K., and Orr, F.M., Jr.: "Time scales for migration and trapping of CO<sub>2</sub> in saline aquifers," Proc. 8<sup>th</sup> Intl. Conf. on Greenhouse Gas Control Technologies, Trondheim, Norway, June 19-22, 2006.
14. Seto, C.J., Jessen, K., and Orr, F.M., Jr.: "Analytical modeling of CO<sub>2</sub> storage and enhanced coal bed methane recovery," Proc. 8<sup>th</sup> Intl. Conf. on Greenhouse Gas Control Technologies, Trondheim, Norway, June 19-22, 2006.
15. Seto, C.J., Jessen, K., and Orr, F.M., Jr.: "Analytical Modeling CO<sub>2</sub> Storage and Enhanced Coal Bed Methane Recovery," SPE 102376, SPE Annual Technical Conference, San Antonio, September 24-27, 2006.
16. Hesse, M., Tchelepi, H., and Orr, F.M., Jr.: "Scaling Analysis of the Migration of CO<sub>2</sub> in Saline Aquifers," SPE 102796, SPE Annual Technical Conference, San Antonio, September 24-27, 2006.
17. Ide, S.T., Jessen, K., and Orr, F.M., Jr.: "Time scales for migration and trapping of CO<sub>2</sub> in saline aquifers," submitted to *J. Greenhouse Gas Control*, March, 2007.
18. Seto, C. J., Tang, G. T., Jessen, K., Kovscek, A. R., Orr, F. M. Jr. "Analytical Modeling and Experimental Investigation of Physical Mechanisms," SIAM Conference on Mathematical and Computational Issues in the Geosciences, Santa Fe, NM, 19-22 March, 2007.
19. Xu, Chuntang, Jerry M. Harris, and Youli Quan, Estimating flow properties of porous media with a model for dynamic diffusion, SEG Expanded Abstract, 2006

20. Xu, Chuntang, 2007, Estimation of effective compressibility and permeability of porous materials with differential acoustic resonance spectroscopy, PhD thesis, Department of Geophysics, Stanford University
21. Lin, W., G.-Q. Tang, and A. R. Kovscek, "Sorptions-Induced Permeability Change of Coal During Gas-Injection Processes," SPE-109855, Proceedings of the SPE Annual Technical Conference and Exhibition, Anaheim, CA. Nov. 11 - 14, 2007.
22. Jessen, K., G.-Q. Tang, and A. R. Kovscek, "Multicomponent Sorptions Modeling in ECBM Displacement Calculations" SPE-110258, Proceedings of the SPE Annual Technical Conference and Exhibition, Anaheim, CA. Nov. 11 - 14, 2007
23. Zoback, M., CO<sub>2</sub> Sequestration in Depleted Oil and Gas Reservoirs, Saline Aquifers and Unmineable Coal Beds, Presentation at Conoco-Phillips, April 2<sup>nd</sup>, 2007.
24. Ross, H., CO<sub>2</sub> sequestration and ECBM in coalbeds of the Powder River Basin, Wyoming, Presentation at BP, Houston, August 9<sup>th</sup>, 2006.
25. Kovscek, A. R., "Geological Storage of Carbon Dioxide: What We Have Found and What Should Be Future Priorities," 6th Annual Conference of Carbon Capture & Sequestration, Pittsburgh, PA May 7-10, 2007.

## References

1. Bell, G. J., Rakop, K. C. "Hysteresis of Methane/Coal Sorptions Isotherms," paper SPE 15454 presented at the 61<sup>st</sup> Annual Technical Conference and Exhibition New Orleans, LA, 5-8 October 1986.
2. Chaturvedi, T. "Spontaneous Imbibition and Wettability Characteristics of Powder River Basin Coal," Master's report, Stanford University, Stanford CA, 2006.
3. Clarkson, C. R., Bustin, R. M. "Binary Gas Adsorption/Desorption Isotherms: Effect of Moisture and Coal Composition Upon Carbon Dioxide Selectivity Over Methane," International Journal of Coal Geology, **42**, vol. 4, 241-271, 2000.
4. Harpalani, S., Zhao, X. "An Investigation of the effect of gas desorption on coal permeability," presented at The Coalbed Methane Symposium, University of Alabama, Tuscaloosa, AB, 17-20 April 1989.
5. Larson, R. G. "The Influence of Phase Behavior on Surfactant Flooding," *SPEJ*, **12**, 411-422, 1979
6. Mazumder, S., Plug, W.-J., Bruning, H. "Capillary Pressure and Wettability Behaviour of Coal-Water-Carbon Dioxide System," SPE 84339, presented at the SPE Annual Technical Conference and Exhibition, Denver, CO, 5-8 October 2003.
7. Seri-Levy, A., Levy, D. "Effect of heterogeneous surface geometry on adsorption." *Langmuir*, **9**, pp. 3067-3076, 1993
8. Seto, C. J. "Analytical Theory for Two-Phase, Multicomponent Flow in Porous Media with Adsorption," Ph. D. dissertation, Stanford University, Stanford, CA, April 2007.
9. Zhu, J., Jessen, K., Kovscek, A. R., and Orr, F. M. Jr., "Analytical Theory of Coalbed Methane Recovery by Gas Injection," *Soc. Pet. Eng. J.* (Dec. 2003) 371-379.
10. Markham, E. C. and Benton, A. F.: "The Adsorption of Gas Mixtures by Silica," *J. Am. Chem. Soc.* (Feb. 1931) 497-507.
11. Myers, A.L. and Prausnitz, J. M.: "Thermodynamics of Mixed Gas Adsorption," *A. I. Ch. E. Journal* (Jan 1965) 11(1) 121-127.
12. Resnik, A. A., Singh, P. K., and Foley, W. K.: "An Analysis of the Effect of CO<sub>2</sub> Injection on the Recovery of In-Situ Methane From Bituminous Coal: An Experimental Simulation," *Soc. Pet. Eng. J.* (Oct. 1984) 521-528.
13. Mavor, M., Pratt, T., and DeBruyn, R.: "Study Quantifies Powder River Coal Seam Properties" *Oil&Gas J.* (Apr. 26 1999) 35-41.
14. Peng, D. Y. and Robinson, D. B.: A New Two-Constant Equation of State," *Ind Eng. Chem Fund.* **15** (1976) 59-64.
15. Hall, F. E., Zhou, C., Gasem, K.A.M., Robinson, R. L., and Yee, D.: "Adsorption of Pure Methane, Nitrogen, and Carbon Dioxide, and Their Binary Mixtures on Wet Fruitland Coal," paper

- SPE 29194 presented at the presented at the SPE Eastern Regional Conference and Exhibition, Charleston, WV 23-26 Sept. 1990.
16. Jessen, K., Gerritsen, M.G., Lambers, J.V., and Mallison, B.T.: "A Fully Adaptive Streamline Framework for the Challenging Simulation of Gas-Injection Processes," paper SPE 97270 presented at the SPE Annual Technical Conference and Exhibition, Dallas, TX 8-12 Oct. 2005.
  17. Advanced Resources International, Inc., Powder River Basin coalbed methane development and produced water management: DOE/NETL-2003/1184, 2002.
  18. Applied Hydrology Associates, Inc. and Greystone Environmental Consultants, Inc., Groundwater modeling of impacts associated with mining coal bed methane development in the Powder River Basin: Technical Report Powder River Basin Oil and Gas Environmental Impact Statement, U.S. Bureau of Land Management, Buffalo Field Office, 2002.
  19. Ayers, W., Coalbed gas systems, resources, and production and a review of contrasting cases from the San Juan and Powder River basins: AAPG Bulletin, 86, 1853-1890, 2002.
  20. Bartos, T. T. and Ogle, K. M., Water quality and environmental isotopic analyses of ground-water samples collected from the Wasatch and Fort Union Formations in areas of coalbed methane development — implications to recharge and ground-water flow, Eastern Powder River Basin, Wyoming: U.S. Geological Survey Water-Resources Investigations Report 02-4045, 88pp, 2002.
  21. Colmenares, L. B. and Zoback M. D., Hydraulic Fracturing and Wellbore Completion of Coalbed Methane (CBM) Wells in the Powder River Basin, Wyoming: Implications for Water and Gas Production: AAPG Bulletin, 91, 51-67, 2007.
  22. Energy Information Administration, State emissions by year: <http://www.eia.doe.gov/environment.html>, 2007.
  23. Flores, R. M. and Bader, L. R., Fort Union coal in the Powder River Basin, Wyoming and Montana: A synthesis: U.S. Geological Survey Professional Paper, 1625-A, PS8-PS29, 1999.
  24. Flores, R. M., Coalbed methane in the Powder River Basin, Wyoming and Montana: An assessment of the Tertiary-Upper Cretaceous coalbed methane total petroleum system: U.S. Geological Survey Digital Data Series, DDS-69-C, chapter 2, 2004.
  25. GEM, GEM 2005.15 User's Guide: Computer Modelling Group Ltd., Calgary, Alberta, Canada, 2005.
  26. Harpalani, S., Gas flow characterization of Illinois coal: Final technical report, ICCI project number 03-1/7.1B-2, 2005.
  27. Jones, A. H., G. J. Bell and R. A., Schraufngel, A review of the physical and mechanical properties of coal with implications for coalbed methane well completion and production: Coalbed Methane, San Juan Basin, Rocky Mountain Association of Geologists, 169-181, 1988.
  28. Kovsky, A. R. and Orr, F. M., Rapid prediction of CO<sub>2</sub> movement in aquifers, coal beds, and oil and gas reservoirs: Stanford University Global Climate and Energy Project (GCEP) Technical Report 2003-2004, 115-147, [http://gcep.stanford.edu/research/technical\\_report/2004.html](http://gcep.stanford.edu/research/technical_report/2004.html), 2004.
  29. Laubach, S. E., R. A. Marrett, J. E. Olson and A. R. Scott, Characteristics and origins of coal cleat: A Review: International Journal of Coal Geology, 35, 175-207, 1998.
  30. Law, D. H. -S., L. G. H. van der Meer and W. D. Gunter, Comparison simulators for greenhouse gas sequestration in coalbeds, part III: More complex problems: 2<sup>nd</sup> Annual Conference on Carbon Sequestration, May 5-8., 2003.
  31. Mavor, M. J., B. Russell and T. J. Pratt, Powder River Basin Ft. Union coal reservoir properties and production decline analysis: SPE 84427, presented at the SPE Annual Technical Conference and Exhibition, Denver, Colorado, October 5-8, 2003.
  32. Nelson, C. R., Geologic Suitability of Coal Deposits in the Northern Great Plains Region of the United States for CO<sub>2</sub> Sequestration: Proceedings of the 8<sup>th</sup> International Conference on Greenhouse Gas Control Technologies, June 19-22, 2006.
  33. Palmer, I. and Mansoori, J., How Permeability Depends on Stress and Pore Pressure in coalbeds: A New Model: SPE 36737, Proceedings of the 71st Annual Technical Conference, Denver, CO, 1996.
  34. Palmer, I., and Mansoori, J., How Permeability Depends on Stress and Pore Pressure in Coalbeds: A New Model: SPE Reservoir Evaluation & Engineering, 52607, 539-544, 1998.
  35. Tang, G. -Q., K. Jessen and A. R. Kovsky, Laboratory and simulation investigation of enhanced coalbed methane recovery by gas injection: SPE 95947, presented at the SPE Annual Technical Conference and Exhibition, Dallas, Texas, October 8-12, 2005.

36. Twombly, G., S. H. Stepanek and T. A. Moore, Coalbed methane potential in the Waikato Coalfield of New Zealand: A comparison with developed basins in the United States: 2004 New Zealand Petroleum Conference Proceedings, 2004.
37. U.S. Geological Survey National Oil and Gas Resource Assessment Team, 1995 National assessment of United States oil and gas resources: U. S. Geological Survey Circular 1118, 1995.
38. van Wageningen, N., Lessons learned from RECOPOL (ECBM) pilot: presented at the fifth International Forum on Geologic Sequestration of CO<sub>2</sub> in Deep, Unmineable Coalseams (Coal-Seq V), Houston, Texas, November 8-9, 2006.
39. Wyoming Oil and Gas Conservation Commission (WOGCC), accessed between 2004 and 2007, <<http://wogcc.state.wy.us/>>.
40. Shuck, E.L., T.L. and R.D. Benson, Multicomponent 3-D characterization of a coalbed methane reservoir: *Geophysics*, Vol. 61, No. 2, P. 315–330, 1996
41. Wang, Z., Seismic anisotropy in sedimentary rocks, part 2: Laboratory data: *Geophysics*, Vol. 67, No. 5, P. 1423–1440, 2002.
42. Buchanan, D. J., P. J. Jackson, and R. Davis, Attenuation and anisotropy of channel waves in coal seams: *Geophysics*, Vol. 18. No. 2, P. 13.1–147, 1983.
43. Dunne, J. and G. Beresfordz, Improving seismic data quality in the Gippsland Basin (Australia): *Geophysics*, Vol. 63, No. 5, P. 1496–1506, 1998.
44. Gochioco, L.M., Shallow VSP work in the U.S. Appalachian coal basin: *Geophysics*, VOL. 63, NO. 3, P. 795–799, 1998.
45. Henson, H., Jr. and J.L. Sexton, Premine study of shallow coal seams using high-resolution seismic reflection methods: *Geophysics*, Vol. 56. No. 9, P. 1494–1503, 1991.
46. Krey, Th., H. Arnetzb, and M. Knecht, Theoretical and practical aspects of absorption in the application of in-seam seismic coal exploration: *Geophysics*, Vol. 47., No. 12, P. 1645–1656, 1982.
47. Ramos, Antonio C. B. and Thomas L. Davisz, 3-D AVO analysis and modeling applied to fracture detection in coalbed methane reservoirs: *Geophysics*, Vol. 62, No. 6, P. 1683–1695, 1997.
48. Richardson S.E. and D.C. Lawton, Time-lapse seismic imaging of enhanced coalbed methane production: a numerical modelling study: *CREWES Research Report*, Vol. 14, 2002.
49. Akintunde, Olusoga M., Jerry M. Harris, and Youli Quean, 2004, Cross-well seismic monitoring of Coal Bed Methane (CBM) production: A case study from the Powder River Basin of Wyoming, *SEG Expanded Abstracts*, pp. 2307-2310.
50. Krail, P.M., Vertical cable as a subsalt imaging tool: *The Leading Edge*, Vol 13, 1994
51. Ikelle, L. and R.J. Wilson, Potential impacts of vertical cable (VC): *The Leading Edge*, Vol 18, 1999
52. J. S. Gulati, R. R. Stewart‡, and B. H. Hoffe, Vertical hydrophone cable acquisition and imaging on land: *Geophysics*, Vol 66, No. 4, P. 1190-1194, 2001
53. Ajo-Franklin, J. B., J. A. Urban, and J. M. Harris, 2006, Using resolution-constrained adaptive meshes for traveltimes tomography: *Journal of Seismic Exploration*, **14**, 371-392.
54. Ajo-Franklin, J. B., J. A. Urban, and J. M. Harris, 2005, Temporal integration of seismic traveltimes tomography: 75th Annual International Meeting, SEG, Expanded Abstracts, 2468-2471.
55. Bottema, O., 1982, On the area of a triangle in barycentric coordinates: *Crux Mathematicorum*, **8**, 228-231.
56. Davis, T., M. R. B. Terrel, R. Cardona, R. Kendall, and R. Winarsky, 2003, Multicomponent seismic characterization and monitoring of the CO<sub>2</sub> flood at Weyburn Field, Saskatchewan: *The Leading Edge*, **22**, 696-697.
57. Devaney, A. J., 1984, Geophysical diffraction tomography: *IEEE Transactions on Geoscience and Remote Sensing*, **22**, 3-13.
58. Harris, J. M., 1987, Diffraction tomography with discrete arrays of sources and receivers, *IEEE Transactions on Geoscience and Remote Sensing*, V. GE-25, n. 4, p. 448-455.
59. Lazaratos, S., and B. Marion, 1997, Crosswell seismic imaging of reservoir changes caused by CO<sub>2</sub> injection: *The Leading Edge*, **16**, 1300-1306.
60. Lumley, D., 2001, Time-lapse seismic reservoir monitoring: *Geophysics*, **66**, 50-53.
61. Penrose, R., 1955, A generalized inverse for matrices: *Proceedings of the Cambridge Philosophical Society*, **51**, 406-413.

62. Persson, P.-O. and G. Strang, 2004, A Simple Mesh Generator in MATLAB: *SIAM Review*, **46**, p. 329-345.
63. Rickett, J., and D. Lumley, 2001, Cross-equalization data processing for time-lapse seismic reservoir monitoring: A case study from the Gulf of Mexico: *Geophysics*, **66**, 1015-1025.
64. Rocha Filho, A. A., 1997, *Formulação Matricial Multifrequência e Inversão Integrada* (in Portuguese): M.Sc. Dissertation, Federal University of Bahia.
65. Santos, E. T. F., 2006, *Inversão tomográfica sísmica anisotrópica com regularização ótima* (in Portuguese): D.Sc. Thesis, Federal University of Bahia.
66. Tikhonov, A. N., and V. Y. Arsenin, 1977, *Solution of Ill-Posed Problems*: Wiley.
67. Wu, R-S, and M. N. Toksöz, 1987, Diffraction tomography and multisource holography applied to seismic imaging. *Geophysics*, **52**, 11-25.
68. Beinkafner K (1986) Use of dipmeter logs to refine structural mapping of Teapot Dome, Wyoming. *AAPG Bulletin* 70 (8): 1031
69. Brown KM, Bekins B, Clennell B, Dewhurst D and Westbrook GK (1994) Heterogeneous hydrofracture development and accretionary fault dynamics. *Geology* (22): 259-262.
70. Chang C, Zoback MD and Khaksar A (2006) Empirical relations between rock strength and physical properties in sedimentary rocks. *Journal of Petroleum Science and Engineering* 51: 223-237
71. Cooper SP and Goodwin LB (1998) Fracture characterization and variability within a basement-cored Laramide age anticline, Teapot Dome, Wyoming. *AAPG Annual Convention Abstract*
72. Finkbeiner T, Zoback MD, Flemings P and Stump B (2001) Stress, pore pressure, and dynamically constrained hydrocarbon columns in the South Eugene Island 330 Field, northern Gulf of Mexico. *American Association of Petroleum Geologists* 85 (6): 1007-1031
73. Friedmann SJ, Nummedal D, Stamp VW (2004) Science and technology goals of the Teapot Dome field experimental facility. *NETL 3rd Annual Carbon Sequestration Conference Proceedings*, Alexandria, VA, Exchange Monitor Publications
74. Grasso JR (1992) Mechanics of seismic instabilities induced by the recovery of hydrocarbon. *Pure and Applied Geophysics* 139 (3/4):507-533
75. Hubbert MK and Willis DG (1957) Mechanics of hydraulic fracturing. *Pet Trans AIME* 210:153-63
76. Jahn F, Cook M and Graham M (1998) *Hydrocarbon exploration and production*. Elsevier Amsterdam, 384 pp.
77. McCutcheon T (2003) *Time Structure Maps – 3D Seismic Data Interpretation*, Teapot Dome Oil Field, Naval Petroleum Reserve No. 3, Natrona County, Wyoming. *Rocky Mountain Oilfield Testing Center Report*
78. Milliken MD (2005) *Surface Mapping Validates 3D Seismic Faulting Interpretations at Teapot Dome Field*, Natrona Co., Wyoming.
79. <http://www.searchanddiscovery.com/documents/abstracts/2005rocky/RMmilli.htm>
80. Milliken MD and Koepsell R (2003) Imaging Technology offers enhanced interpretation of Teapot Dome reservoirs. *Wyoming Geological Association Field Guidebook 2002*: 41-62
81. Moos D and Zoback MD (1990) Utilization of observations of well bore failure to constrain the orientation and magnitude of crustal stresses: application to continental, deep sea drilling project and ocean drilling program boreholes. *Journal of Geophysical Research* 95 (B6):9305-9325.
82. Raleigh CB, Healy JH and Bredehofft JD (1976) An experiment in earthquake control at Rangeley, Colorado. *Science* 191:1230-1237
83. Segall P and Fitzgerald SD (1996) A note on induced stress changes in hydrocarbon and geothermal reservoirs. *Tectonophysics* 289: 117-128
84. Twiss RJ and Moores EM (1992) *Structural Geology*, W. H. Freeman, New York. 532 pp.
85. Wiprut DJ and Zoback MD (2002) Fault reactivation, leakage potential, and hydrocarbon column heights in the northern North Sea. In: Koestler AG and Hunsdale R (eds) *Hydrocarbon Seal Quantification (NPF Special Publication)* 11: 203-219
86. Zhang Q, Nummedal D and Yin P (2005) Stratigraphy, sedimentology and petrophysics of the Tensleep Sandstone at Teapot Dome and in outcrop. <http://www.searchanddiscovery.com/documents/abstracts/2005rocky/RMzha.htm>

87. Zoback MD, Barton CA, Brudy M, Castillo DA, Finkbeiner T, Grollmund BR, Moos DB, Peska P, Ward CD and Wiprut DJ (2003) Determination of stress orientation and magnitude in deep wells. *International Journal of Rock Mechanics and Mining Sciences* 40: 1049-1076
88. A. P. Aldushin, New Results in the Theory of Filtration Combustion. *Combustion and Flame* 94 (1993) 308–320.
89. DeKok, D., 1986, Unseen danger: University of Pennsylvania Press, p. 299.
90. Fields, Scott, 2002, Underground Fires Surface: Environmental Health Perspectives: v. 110, no. 5, A 234.
91. Geissinger, J., 1990, Managing underground mine fires: the case of Centralia, Pennsylvania: The Pennsylvania Geographer, v. 28, no. 2, p. 22-26.
92. Memmi, J., 2000, Cooking Centralia: a recipe for disaster: Geotimes (September): v. 45, no. 9, p. 26 – 27.
93. Mehl, James B. and Moldover, Michael R., 1981. Precision acoustic measurements with a spherical resonator: Ar and C<sub>2</sub>H<sub>4</sub>. *J. Chem. Phys.*, Vol. 74, No. 7, 1 April 1981.
94. Xu, Chuntang, 2007. Dynamic diffusion, Ph.D. Thesis, Department of Geophysics, Stanford University.
95. Morse, P. M. and Ingard, K. U., 1968, Theoretical acoustics: McGraw-Hill Book Company. New York.
96. Harpalani, S. and Zhao, X., The Unusual Response of Coal Permeability to Varying Gas Pressure and Effective Stress. *Rock Mechanics as a Guide for Effective Utilization of Natural Resources*, Khair (ed.), 65–72, 1989.
97. Gray, I., Reservoir Engineering in Coal Seams: Part 1—The Physical Process of Gas Storage and Movement in Coal Seams. SPE 12514 presented at SPE Reservoir Engineering February, 1987.
98. Palmer, I. and Mansoori, J., How Permeability Depends on Stress and Pore Pressure in Coalbeds: A New Model. SPE 52609 presented at SPE annual Technical Conference and Exhibition in Colorado, the USA, revised for publication from SPE 36737 October 6-9, 1996.
99. Seidle, J. and Huitt, L., Experimental Measurement of Coal Matrix Shrinkage Due to Gas Desorption and Implications for Permeability Increases. SPE 30010 presented at the International Meeting on Petroleum Engineering in Beijing, China November 14-17, 1995.
100. Palmer, I. and Mansoori, J., How Permeability Depends on Stress and Pore Pressure in Coalbeds: A New Model. SPE 52609 presented at SPE annual Technical Conference and Exhibition in Colorado, the USA, revised for publication from SPE 36737 October 6-9, 1996.
101. Tang, G., Jessen, K., and Kovscek, A., Laboratory and Simulation Investigation of Enhanced Coalbed Methane Recovery by Gas Injection. SPE 97947 presented at the 2005 SPE Annual Technical Conference and Exhibition, Dallas, TX U.S.A. October 8-12, 2005.
102. Yang, R., Gas Separation by Adsorption Processes. Butterworths Publishers, Johannesburg, South Africa, pp 26–51, 1987.
103. Myers, A. and Prausnitz, J., Thermodynamics of Mixed-Gas Adsorption. *A.I.Ch.E. Journal*, 121–127, 1965.
104. Reiss, L.H., The Reservoir Engineering Aspects of Fractured Formations, Gulf Publishing Company, 1980.
105. Deutsch, C. V., 2002, Geostatistical reservoir modeling: Oxford University Press.
106. Maybeck, Peter S. 1979. Stochastic Models, Estimation, and Control, Volume 1, Academic Press, Inc.
107. Akin, S. and A. R. Kovscek, 2003. “Computed Tomography in Petroleum Engineering Research,” in *Applications of X-ray Computed Tomography in the Geosciences*, Mees, F., Swennen, R, Van Geet, M. and Jacobs, P. (eds), Geological Society, London, Special Publications, **215**, 23-38.
108. Handy L.L. 1960. “Determination of effective capillary pressure for porous media from imbibition data.” *Pet. Trans AIME* 219 75-80, 1960.
109. Schembre, J. M. and A. R. Kovscek 2006. "Estimation of Dynamic Relative Permeability and Capillary Pressure from Countercurrent Imbibition Experiments, *Transport in Porous Media*, 65(1) 31-51. DOI: 10.1007/s11242-005-6092-5.
110. Fujioka, Masaji, 2006, Japan CO<sub>2</sub> Geosequestration in Coal Seams Project 2006, International Forum on Geologic Sequestration of CO<sub>2</sub> in Deep, Unmineable Coal seams (Coal-Seq V), Houston, Texas, Nov 8-9, 2006.

111. Pagnier, H.J.M., Van Bergen, F., and Van der Meer, L.G.H., 2003, Field experiment of ECBM in the Silesian Coal Basin of Poland (RECOPOL). International Coalbed Methane Symposium 2003, Tuscaloosa, Alabama (USA), May 5-9, 2003.
112. Palmer, I. and Mansoori, J., 1998, How Permeability Depends on Stress and Pore Pressure in Coalbeds: A New Model, SPE 52607, SPEREE, pp. 539-544.
113. Ross, H. E. and Zoback, M. D., 2006, Reservoir characterization of coals in the Powder River Basin, Wyoming, USA, for CO<sub>2</sub> sequestration feasibility studies: Greenhouse Gas Control Technologies Conference 8, Trondheim, Norway, June 19-22.

## Contacts

Jerry M. Harris: [harris@pangea.stanford.edu](mailto:harris@pangea.stanford.edu)  
Anthony R. Kovscek: [kovscek@pangea.stanford.edu](mailto:kovscek@pangea.stanford.edu)  
Franklin M. Orr, Jr.: [fmorr@pangea.stanford.edu](mailto:fmorr@pangea.stanford.edu)  
Mark D. Zoback: [zoback@pangea.stanford.edu](mailto:zoback@pangea.stanford.edu)  
Paul Hagin: [hagin@pangea.Stanford.edu](mailto:hagin@pangea.Stanford.edu)  
Youli Quan: [quany@stanford.edu](mailto:quany@stanford.edu)  
Eduardo Santos: [eduardot@stanford.edu](mailto:eduardot@stanford.edu)  
Tom Tang: [gtang@pangea.stanford.edu](mailto:gtang@pangea.stanford.edu)  
Adeyemi Arogunmati: [aadeyemi@stanford.edu](mailto:aadeyemi@stanford.edu)  
Laura Chiaramonte: [chiarlau@stanford.edu](mailto:chiarlau@stanford.edu)  
Jolene Robin-McCaskill: [jmrobin@stanford.edu](mailto:jmrobin@stanford.edu)  
Hannah Ross: [hemiller@stanford.edu](mailto:hemiller@stanford.edu)  
Chun-tang Xu: [xct7015@stanford.edu](mailto:xct7015@stanford.edu)  
Taku Ide: [idetaku@stanford.edu](mailto:idetaku@stanford.edu)  
Wenjuan Lin: [wenjuanl@stanford.edu](mailto:wenjuanl@stanford.edu)  
Carolyn Seto: [cjseto@pangea.stanford.edu](mailto:cjseto@pangea.stanford.edu)  
Reginald Mitchell: [remitche@stanford.edu](mailto:remitche@stanford.edu)